VORTICAL STRUCTURES GENERATED BY A LOCALIZED FORCING

VASILY N. KORABEL

VORTICAL STRUCTURES

GENERATED BY A LOCALIZED FORCING

by

Vasily N. Korabel

Dissertation submitted to the School of Graduate Studies
in partial fulfillment of the
requirements for the degree of
Doctor of Philosophy

Department of Physics and Physical Oceanography
Memorial University of Newfoundland
2005

Advisory Committee:

Professor Yakov D. Afanasyev, Chair/Advisor
Professor Brad de Young
Professor Len Zedel

Your file Votre référence
ISBN: 978-0-494-15659-9
Our file Notre référence
ISBN: 978-0-494-15659-9

ABSTRACT

Vortex structures (monopoles, dipoles, quadrupoles) as well as more complex structures (vortex streets) are fundamental elements of geophysical turbulence. Because they can effectively transport momentum, heat, salt and biochemical products, they play an essential role in ocean dynamics. Organized vortex structures are a well known feature of quasi-two-dimensional flows where motion in one direction is suppressed due to one of the following physical mechanisms: background rotation of the system, density stratification or geometrical restrictions such as for the flows in thin layers or soap films.

Vortex dipoles are formed in a viscous fluid when a force is applied locally to some volume of fluid. If the force acts impulsively, a translating vortex dipole is generated. If the force starts at $t = 0$ and then acts continuously a starting jet with a dipole at its front is generated. Solutions for unsteady viscous flows generated by the action of continuous or impulsive localized forces are obtained in Oseen approximation. The solutions are compared with direct numerical simulations of vortex dipoles as well as with laboratory experiments. The comparison shows good quantitative agreement in both cases.

A physical problem where the localized force acting continuously on fluid is placed in a uniform stream is equivalent to a problem of a fixed body in a uniform stream, while the couple of forces acting in opposite direction are equivalent to the problem of self-propelled body moving at constant velocity through a fluid. The solutions for the two-dimensional far-field wake are obtained in both cases. At a certain Reynolds number, wakes become unstable and form vortex streets. New series of high-resolution 2D numerical simulations is performed to study the characteristics of the wakes including the shedding frequency for a wide range of control parameters such as translational velocity, magnitude and spatial extent of a localized force. The results of numerical experiments of unsteady wake flow show existence of a great variety of flow regimes and are in good qualitative agreement with laboratory experiments.

Acknowledgements

I would like to thank Prof. Iakov Afanasyev for the supervision of this work. I am particularly indebted to him for his continuing generous help and enthusiasm spirit during all phases of the thesis.

I extend my gratitude to Prof. Len Zedel and Prof. Brad de Young to have kindly accepted to take part in the jury of my thesis and for their helpful comments on the manuscript.

Thanks to all the Ph.D. students at the Department of Physics for creating a delightful atmosphere. Thanks to my family and parents who have faithfully supported and encouraged me over my many years of education.

TABLE OF CONTENTS

LIST OF FIGURES

LIST OF TABLES

Chapter 1

Introduction

The goal of this dissertation is the investigation of a new class of flows generated by a moving localized forcing in a quasi two-dimensional geometry. The force is called localized if it is applied to some region in space locally. In many cases, this region is small compared to the typical length scale of the flow generated by the force. The situation when flows are investigated in a quasi two-dimensional geometry often arise if the motion in one direction is suppressed. Physical mechanisms leading to two-dimensialization of the flow could be a background rotation of the system, density stratification or geometrical restrictions such as for the flows in thin layers or soap films.

The approach taken in this dissertation consists of numerical simulations of strictly two dimensional flows, laboratory experiments with quasi two-dimensional flows and theoretical investigation. In laboratory experiments the electromagnetic method was

used to produce the forcing. It represents the adaptation of the existing method of forcing usually used for the investigation of quasi two-dimensional turbulence (Afanasyev and Wells 2005). The main idea of the method can be described as follows. The flow is generated in a two-layer solution of salt. The two-layer system is proved to work well for studying two-dimensional flows, because the relaxation time for three-dimensional perturbations in this system is small compared to other characteristic times of the system (Tabeling et. al. 1997). In a two-layer fluid in the presence of a uniform electric field, an external localized force can be exerted on fluid by a small permanent magnet which produces the Lorenz force. Consequently, the force generates motion of fluid and creates the vorticity. In numerical experiments the localized forcing is introduced as an external body force on the right-hand side of the Navier-Stokes equations. The force is applied to the fluid within a circular area. In theoretical analysis, however, the concept of the point force was used, where the localized force is of the form of Dirac delta function $F \sim \delta(x)$.

The importance of the investigation of flows generated by the localized forcing is supported by a large number of examples of such flows in nature and technology. In oceanography, various natural phenomena can be associated with localized forces, such as baroclinic instability, instability of fronts or wind forcing. Action of localized (impulsive) forces on a viscous fluid results in the formation of vortex dipoles. They are often called mushroom-like currents since they resemble a sliced mushroom (Ginzburg and Fedorov 1984; Fedorov and Ginzburg 1989). Numerous satellite observations of the upper ocean revealed regular formation of dipoles in the regions where a current separates from the shelf (de Ruijter 2004). In the coastal zone dipolar structures may also be formed by upwelling, water exchange through a strait, abrupt melting of ice or by the flow from the river mouth (Fedorov and Ginzburg, 1992; Grishin, 1993; Ginzburg, 1994; Sur et al., 1994, 1996; Sur and Ilyin, 1997; Ginzburg

et al., 1998, 2000a, 2000b, Goncharov and Pavlov 2001). The typical view of the mushroom-like currents generated by a separated flow near the Madagascar shelf and dipolar vortex ejected by the river mouth is shown in Figure 1.1. Mushroom-like currents play an important role in exchange between shelf and deep-sea water. Since they are caused by the action of localized forces, they possess linear momentum. This means that such vortical structures can transport heat, salt, nutrients and plankton through large distances from their origin and thus present an effective mechanism for horizontal mixing in the ocean.

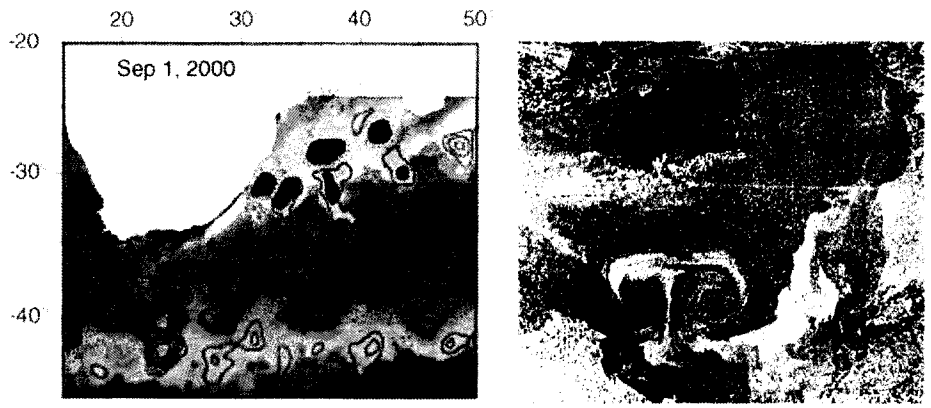

Figure 1.1: (a) Sea surface temperature (SSH) image of the train of vortex dipoles forming around South Madagascar and propagating into the Agulhas Current region, taken from P.M. de Ruijter (2004); (b) Vortex pairs observed in SSH near the coastal line forming as the result of the flow from the river mouth, (from Goncharov, Pavlov 2001).

More complicated vortical structures, such as vortical wakes are also widely observed in nature. They are produced by a stationary localized forcing placed in a moving stream or by moving localized vortices. One example is the wakes behind islands. Strong tidal currents such as observed in the Bay of Fundy interact with large number of small islands and produce organized system of transient eddies on the lee side of the island (Wolanski et al. 1984; Geyer and Signell 1990; Rankin et al. 1994; Lee et al. 1999). Recently, Neill and Elliot 2004 reported on the observations of the distinctive von Kármán vortex street produced by Beamer Rock, a 50-m-wide island in the Firth of Forth (Scotland). The characteristics of the vortex street depend on the speed and direction of the tidal flow (Neill and Elliot 2004). A typical picture of vortical wakes formed in the atmosphere behind the Alaska's Aleutian Islands is shown in Figure 1.2. Since the eddies formed by island wakes can trap water and particulates behind islands (Wolanski et al., 1984, St. John and Pond 1992), the investigation of such flows has important implications for the fishing industry, waste treatment, and for navigation of small vessels.

The investigation of the flows generated by a moving localized forcing is also important due to numerous engineering applications. This type of flows is closely related to wakes behind nonstreamlined (bluff) bodies. Flow around a circular cylinder which is a classical problem of fluid dynamics, belongs to this class of flows. Such vortical flows have found application in many industrial apparatus, such as chemical mixers and sewage treatment plants (Villermaux and Pope, 1986). Turbulent wakes generated by an array of a large number of cylinders greatly improve the efficiency of mixing systems (Hinch, Gollub, 1999). On the other hand, vortical wakes shed from submerged oil pipes induce vibrations in the presence of strong currents. The resultant large amplitude oscillations can lead to structural failure. The flow generated by more complex forcing such as a system of two localized forces acting in opposite direction

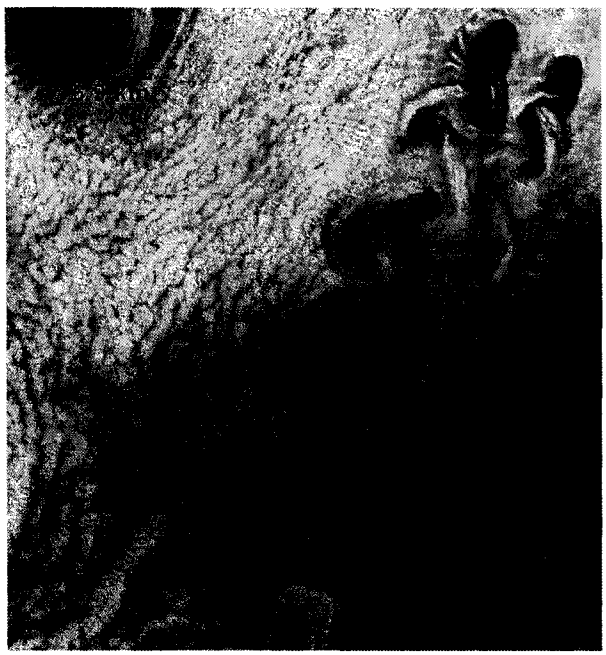

Figure 1.2: The photograph of the Alaska's Aleutian Islands. Vortices in the atmosphere clearly demonstate an island wake. Adapted from the Landsat 7 satellite image taken from the US Geological Survey web page http://landsat.gsfc.nasa.gov.

(force doublet) can serve as a model for wakes behind self-propelled objects including submarines as well as fishes, birds and insects, Triantafyllou et. al 1995, Sane 2003. These flows attract a lot of attention due to military applications connected with surveillance and detection technology and also with problems in bio-hydrodynamics of locomotion (Lighthill 1969, 1970; Wu 1977, Spedding 1985, Triantafyllou 1995, 2000).

1.1 Historical review

1.1.1 Theory

Two-dimensional flows generated in a viscous fluid by localized forces have been extensively studied both theoretically and experimentally by Cantwell 1986, Voropayev and Afanasyev 1994, Afanasyev 2003. This part of the review will cover theoretical results on flows generated by point forces. The systematic treatment of the time-dependent 2D flows arising in initially quiescent viscous fluid under the action of different singularities was started by Cantwell (1986). If a single localized force acts impulsively for a short period of time in an initially static viscous fluid, a translating vortex dipole is generated. If the force acts continuously a jet forms with a dipole at its front. Impulsive and continuous forcing can be formally introduced with the help of the Dirac delta function $\delta(x)$ and the Heaviside function $h(x)$ respectively:

$$\frac{F_i(x,y,t)}{\rho} = I\,\delta(t)\,(\delta(x),\,\delta(y),\,0)\,,$$
$$\frac{F_c(x,y,t)}{\rho} = J\,h(t)\,(\delta(x),\,\delta(y),\,0)\,,$$

where I or J are parameters describing an amplitude of the forcing for impulsive and continuous cases correspondingly. Here $r = \sqrt{x^2+y^2}$ is the position-vector, ρ is the fluid density, and ν is the kinematic viscosity. Cantwell obtained solutions for both impulsive and continuous forcing using Stokes approximation ($Re \to 0$) using similarity variable $\xi = r/(4\nu t)^{1/2}$. The corresponding expressions for the stream-function and vorticity are given as follows:

(i) Impulsive single forcing, $k = 1/2$, $n = 1$

$$\psi(r,\theta,t) = \frac{I(4\nu)^{-\frac{1}{2}}t^{3k-\frac{3}{2}}}{(n-1)} \cdot \frac{\xi}{\pi} e^{-\xi^2}\sin\theta,$$

$$\omega(r,\theta,t) = \frac{I(4\nu)^{-\frac{3}{2}}t^{3k-\frac{5}{2}}}{(n-1)} \cdot \frac{1}{4\pi\xi}(1-e^{-\xi^2})\sin\theta.$$

(ii) Continuous single forcing, $k = 1/2$, $n = 2$

$$\psi(r,\theta,t) = \frac{J(4\nu)^{-\frac{1}{2}}t^{3k-\frac{3}{2}}}{(n-1)} \cdot \frac{1}{\pi\xi}e^{-\xi^2}\sin\theta,$$

$$\omega(r,\theta,t) = \frac{J(4\nu)^{-\frac{3}{2}}t^{3k-\frac{5}{2}}}{(n-1)} \cdot \frac{1}{4\pi\xi}\left(1 - e^{-\xi^2} + \xi^2 E(\xi^2)\right)\sin\theta,$$

here $E(\xi^2)$ is an exponential integral defined as

$$E(\xi^2) = \int_{\xi^2}^{\infty} \frac{e^{-x}}{x}dx.$$

Two equal forces with the intensities I placed at a distance δ one from another constitute a force doublet. The point force doublet is obtained in the limit when the magnitude of the forces tends to infinity while the distance shrinks to zero, such that their product remains constant, $M = lim_{I\to\infty,\,\delta\to 0} I\delta$. Linear Stokes solutions for the case of impulsive and continuous quadrupoles are given in Voropayev and Afanasyev 1994. Here we give the solution only for the impulsive case

$$\psi_{I,M}(x,y,t) = -\frac{Mxy}{\pi(x^2+y^2)^2}\left(1 - (1+\xi^2)e^{-\xi^2}\right).$$

$$\omega_{I,M}(x,y,t) = -\frac{Mxy}{32\pi(\nu t)^3}e^{-\xi^2},$$

Linear solutions describe the general behavior of the flow and are helpful in understanding the flows generated by point forcing. Mathematical modeling of the motion of tracer particles allows us to visualize the flow. Linear combinations of the Stokes solutions are also capable to reproduce general features of the interaction between vortical structures. However, linear solutions fail to describe some important features of the flow, such as the translation of dipoles which is clearly due to non-linear effects. The linear solution is in fact a first order term of the expansion of the full solution in terms of a small parameter, namely the dimensionless forcing amplitude (the Reynolds number). The linear solution can be improved if the next term in the expansion is added thus rendering a weakly nonlinear solution. This second order

term is quadratic in the Reynolds number and is proportional to $\sin 2\theta$ (Voropayev and Afanasyev 1994). The weakly nonlinear solution allows the vortex dipole to drift forward. This solution, however, does not correctly describe the velocity of propagation of the dipoles for moderate and large values of the Reynolds numbers.

The Oseen approximation was used in Afanasyev and Korabel (2004) to describe the translation of the dipole with the help of linearized advection term. Time-dependent solutions for the case of the impulsive and continuous forcing were obtained and compared to the results of numerical simulations. It was found that the Oseen approximation provides a good quantitative agreement with both numerical and laboratory experiments.

If a single force or a force doublet moves with constant speed U in a fluid it generates a wake with a vorticity distribution similar to that generated by stationary forcing but rather stretched along the x-axis by the oncoming stream. A theoretical solution which describes the vorticity and stream function for two-dimensional flows generated by a point force or a force doublet was obtained in the Oseen approximation by Afanasyev (2004). Formally it can be expressed in the integral form as follows:

$$\begin{bmatrix} \psi_{J,Q} \\ \omega_{J,Q} \end{bmatrix} (x, y, t) = \int_0^t \begin{bmatrix} \psi_{I,M} \\ \omega_{I,M} \end{bmatrix} (x - (t - \tau) U, y, t - \tau) d\tau,$$

where $\psi_{I,M}$ and $\omega_{I,M}$ are solutions for the stream-function and vorticity for the impulsive arbitrary forcing acting in steady fluid. This solution describes the time-dependent distribution of vorticity generated by a corresponding forcing. Due to the linearity of the equations used in the Oseen approximation, the effects of vorticity generated by the source in the stream at different times can be superposed directly. The vorticity distribution at any time can then be found by integration of previous distributions where time delay $t - \tau$ and instantaneous position of the source with respect to the moving water are taken into account. An asymptotic theory describing

2D flows generated by a moving point forcing was also developed by Voropayev and Smirnov (2002) using a boundary layer approximation.

1.1.2 Laboratory experiments

A laboratory investigations of the dipolar flows in a stratified fluid were pioneered by Voropayev in 1983. Later the dynamics of individual dipoles as well as their interactions with each other and solid boundaries were studied extensively in laboratory experiments (Afanasyev, Voropayev, Filippov, 1988; Voropayev et al., 1991; Voropayev and Afanasyev, 1992). A typical view of the dipole generated by a localized force is shown in Figure 1.3. In this case a small permanent magnet was used to generate a localized force.

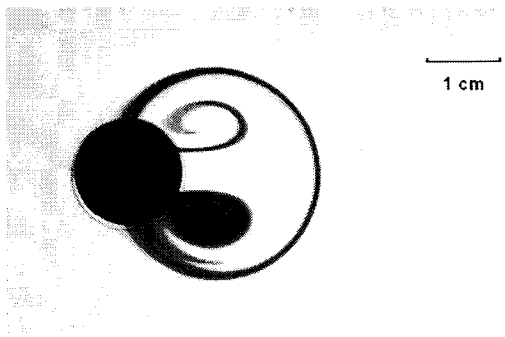

Figure 1.3: Photograph of a vortex dipole generated by localized force. t = 2 sec.

Asymmetric collision of vortex dipoles was described in van Heijst and Flór (1989). Evolution of two-dimensional flows with zero net momentum, such as vortex quadrupoles was investigated by Voropayev and Afanasyev (1993), Voropayev, Afanasyev and van Heijst (1995).

The laboratory investigations of the localized momentum source moving in a stratified fluid were carried out by Voropayev, Smirnov (2003). The momentum source

was modeled with the help of a moving jet. The jet was supplied by a small nozzle translated in the water. The size of the source was small, such that the volume flux was small while the force (momentum flux) was significant. The electro-magnetic method of forcing, when a localized force is modeled with the help of a small permanent magnet was used by Afanasyev, Korabel (2004) to investigate flows generated by moving localized force and force doublet.

1.1.3 Flow behind bluff bodies

A moving bluff body, or, equivalently, a stationary body placed in a uniform stream leaves a vortex trail (wake) behind it. A quantitative description of an unstable wake presents a difficult problem even if the shape of the body is relatively simple such as a cylinder. The flow around a cylinder is a classical problem in fluid mechanics and has a long history of serious investigations. As emphasized by Morkovin (1964), the bluff body wake and vortex street problem has provided fluid dynamics with "a kaleidoscope of challenging fluid phenomena." The foundation behind this quotation is that the flow behind the bluff body is sensitive to the variations of the Reynolds number, Re, where $Re = UD/\nu$. Here U is the velocity, D is diameter of the cylinder and ν is the kinematic viscosity. In range of the Reynolds number from 1 to 10^6 there exists a number of different regimes of the flow.

For the low Reynolds numbers, $0 < Re < 5$ the flow is called "creeping". The flow is dominated by viscosity and the streamlines remain unperturbed and close to the surface of the body, or in other words, there is no separation in the wake. The problem was solved theoretically by Stokes (1851) and then improved by Oseen (1910) for the case of a moving sphere. The solution for the 2D creeping flow behind circular cylinder is given in Lamb (1911). At $Re = 4 - 5$ separation occurs and a steady closed region of recirculation is formed behind the cylinder. It is followed by

two layers of opposite vorticity, as shown in Figure 1.4a. Properties of the closed recirculation region, namely, its length (the distance between the cylinder and the point where two shear layers reconnect) and width (distance between the centers of the recirculating cores) as well as velocity components were explored by Nisi and Porter (1923), Taneda (1956), Grove et.al. (1964), Coutanceau and Bouard (1977).

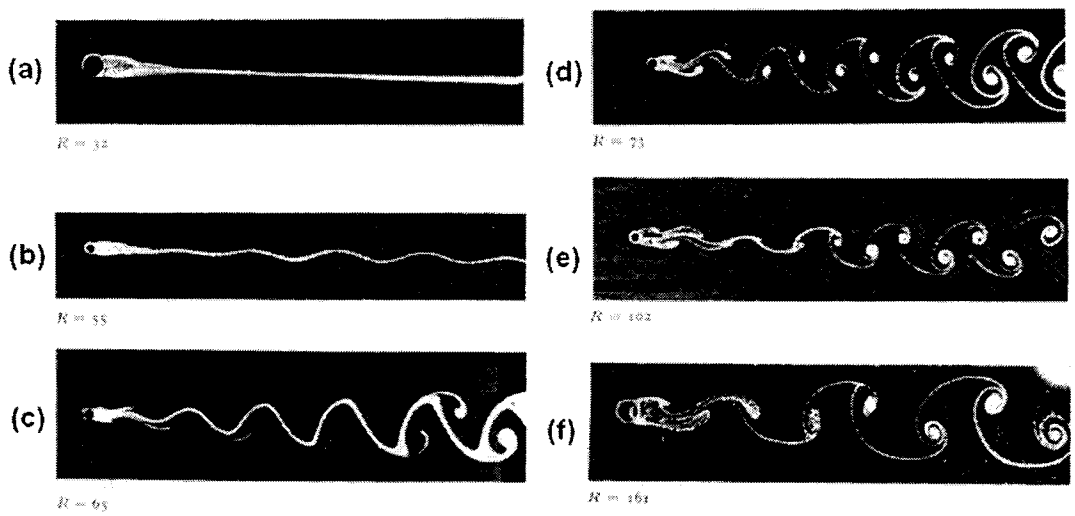

Figure 1.4: The sequence of photographs of the developing wake behind circular cylinder for Reynolds numbers (a) $Re = 34$ (b) $Re = 55$ (c) $Re = 65$ (d) $Re = 73$ (e) $Re = 102$ (f) $Re = 161$. (From Zdravkovich, 1997).

Above a critical Reynolds number $Re_c = 49$ the wake becomes unstable (Figure 1.4b). At moderate Reynolds numbers the unstable wake has a form of oscillating shear layers, but at higher Re, a regular street of alternate vortices forms behind the cylinder (Figure 1.4c). The regular array of vortices is called a Kármán-Bénard vortex street, after Bénard (1908,1913), who carried out pioneering experiments with

a cylinder and Kármán (1954), who developed a mathematical model of the idealized vortex street constructed of point vortices.

Extensive measurements of the velocity fluctuations in the near-wake by Kovasznay (1949) indicated that the latter are very small in the vicinity of the body and that they reach a maximum at some distance downstream from the cylinder. It can be concluded that the vortices are not shed from the body for low Re, but rather develop gradually with downstream distance, as shown in Figure 1.4c. This allows us to make an assumption that the shedding phenomenon may be considered as the instability of the shear layers that form the laminar wake, Kovasznay (1949). Abernathy and Kronauer (1962) suggested that the two shear layers, and not the body itself, are responsible for vortex shedding in the vortex street, and that the body " merely modifies the process by allowing feedback between the wake and the shedding of circulation at the separation points." A vortex is fed by its associated shear layer until it is strong enough to draw over the opposite shear layer. The fluid of oppositely signed vorticity then causes the vortex to be shed and move downstream, whereupon the process repeats itself as more vortices are shed.

Sarpkaya (1979) suggests a more complex process for the shedding of vortices. With the symmetric growth of vortices, the body's shear layer begins to develop instabilities and is drawn across the wake due to the reduced base pressure brought about by the vortex growth. This breaks up the sheet, reducing the supply of vorticity to the growing vortex, bringing it to a minimum, causing the vortex to be shed. The opposite vortex entrains the remaining oppositely signed vorticity. When the circulation for that vortex reaches a minimum, the corresponding shear layer is again drawn across the wake and the vortex is shed, and the process repeats itself.

Strouhal (1878) was the first to measure the frequency of the vortex streets formed behind wires. He proposed the dimensionless combination to describe the shedding

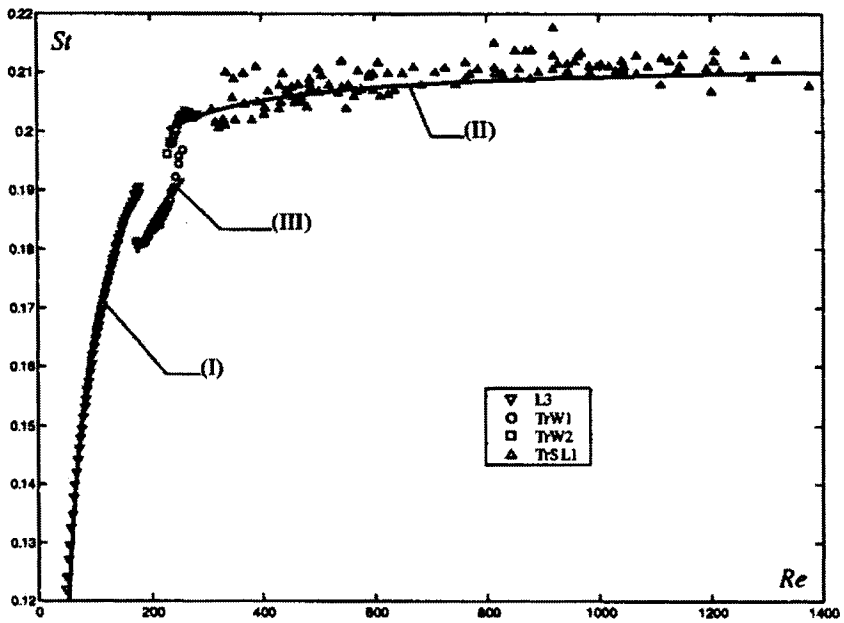

Figure 1.5: Dependence of the dimensionless shedding frequency, Strouhal number, on the Reynolds number of the flow. (From Zdravkovich, 1997).

frequency, which is now known as the Strouhal number:

$$St = fD/U,$$

where f is the dimensional shedding frequency and D is the diameter of the cylinder and U is fluid velocity. Extensive quantitative investigations of vortex street made by Roshko (1954) lead him to the experimental discovery of the vortex street similarity, which is nearly independent of the bluff body. He found that data for the cylinders with different diameters collapse well on a single curve. Based on this curve he found that there exists a number of flow regimes. The transitions between different regimes

are marked by a discontinuities in the St-Re dependence, Tritton (1959, 1971). Roshko (1952) indicated three basic regimes: stable regime for $40 < Re < 150$, transitional regime for $150 < Re < 300$ and irregular regime for $Re > 300$, (Figure 1.5).

To describe the St-Re dependence Roshko proposed empirical relations:

$$St = 0.212 - 4.5/Re, \quad Re < 180$$

and

$$St = 0.212 - 2.7/Re, \quad Re > 300.$$

Numerous laboratory investigations of vortex streets behind circular cylinder performed by Gerrard (1966), Bearman (1984), Zdravkovich (1969, 1972), Williamson (1988, 89), Cimbala (1988) and many others were aimed to refining this relationship. Roshko also noted that another dimensional combination depends linearly on the Reynolds number. This parameter is now called the Roshko number:

$$Ro = fD^2/\nu$$

The corresponding asymptotic relations in terms of this parameter can be found in Roshko (1952):

$$Ro = 0.212Re - 4.5 \quad 50 < Re < 150,$$

$$Ro = 0.212Re - 2.7 \quad 300 < Re < 2000.$$

Williamson (1988) explained the nature of the discontinuities in the shedding frequency curve as the transition between different modes of vortex shedding. He noted that the angle of the slanted vortex measured near the cylinder is closely connected to the discontinuity in shedding curve. For the $Re < 180$ vortices are shed parallel to the cylinder surface, while at $Re > 300$ the oblique shedding mode takes place.

The remarkable feature of the vortex street at moderate Reynolds numbers is its regularity which can be observed at very large distances from the body. The strength

of the vortices decays with distance and at some point the far wake transforms into the stable wake consisting of two layers of vorticity. These two layers of vorticity also become unstable further downstream and a secondary vortex street is formed, Inoue and Yamazaki (1995), Takeda and LeGal (1997), Williamson and Prasad (1993). It is characterized by a larger spatial scale and a lower frequency, compared to the primary vortex street. The typical view of the secondary vortex street is shown on the Figure 1.6.

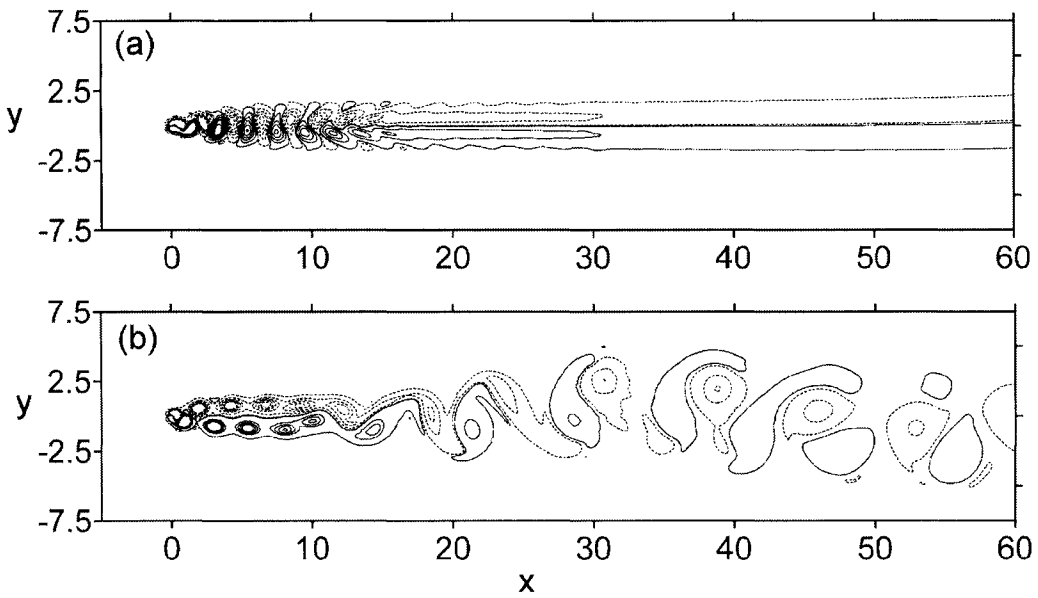

Figure 1.6: Typical view of the development of the secondary vortex street generated by a single localized force $J = 3.77\ cm^3 s^2$ placed in a uniform stream. Contours of vorticity are calculated with a non-linear Navier-Stokes solver (series 6 in Table 3.1) (a) $Re = 100$ and (b) $Re = 120$ Contours $\pm$ 0:1; 1; 2; 3; 4; 5 s^{-1}, scale in cm.

Cimbala, Nagib and Roshko (1988) who studied experimentally the behavior of the far wake for $70 < Re < 2000$ concluded that the parameters of the secondary vortex street do not depend on the scale or frequency of the primary vortex street. This conclusion agrees well with the results of Taneda (1959) who suggested that the formation of the secondary vortex street is explained by the hydrodynamic instability of the developing vorticity layers. On the other hand, Okude and Maysui (1981, 1990) concluded that the results with experiments with the flow behind the forced cylinder indicate that the secondary vortex street is formed by pairing of vortices in the primary vortex street. Recent studies of Vorobieff and Ecke (1999) and Vorobieff et.al (2002) who investigated the far wake flow behind cylinder in the thin soap films showed that the downstream position of the onset of secondary vortex street is proportional to $1/\sqrt{Re}$.

Starting at $Re \approx 150$ the vortex street becomes turbulent further downstream, and at $Re \approx 400$, the vortices themselves become turbulent from the point of generation. For higher values of Reynolds number, vortices lose their regular shape and coherency, making visualization difficult (Mair and Maull 1971, Berger and Wille 1972, Oertel 1990).

1.2 Outline

Chapter 2 covers the theoretical framework for the analysis of numerical simulations and laboratory experiments. Solutions in Stokes approximation for two dimensional dipolar flow are improved by using the Oseen approximation. These solutions are derived for the flows generated by a localized forcing acting in an initially quiescent fluid. Then the Oseen approximation is applied to the flows generated by a moving forcing.

In Chapter 3, laboratory experiments with dipolar flows are described. The design and setup of the laboratory experiments are described in detail. The results of both laboratory experiments and numerical simulations indicate that the Oseen approximation provides a reasonable prediction for the translational velocity of the dipole.

Chapter 4 contains the results and analysis of the numerical experiments with a single localized force. The numerical setup for the high resolution computations is presented. The results of a large number of simulations provide a full description of different regimes of flows generated by a moving localized forcing.

Chapter 5 summarizes results of numerical simulations of flows generated by a force doublet. Relevant analysis and discussions of the flow regimes as well as the dependence of the flow on the main control parameters are presented.

Chapter 6 contains the summary of results and conclusion. The description of the user defined functions used in numerical simulations to introduce a localized forcing is included in the Appendix.

Chapter 2

Background and Theory

2.1 2D vortical structures in steady fluid

The earth's oceans and atmosphere are stratified and rotating fluid systems and as such provide an environment for the evolution of two dimensional dipolar vortical structures. Vortical dipoles are also common in engineering applications. Many industrial applications, such as chemical processing and sewage treatment (Villermaux et. al. 1999, Pope 1994), rely on the ability to effectively mix components. Vortical structures generated by the array of a large number of cylinders greatly improve the efficiency of mixing systems (Hinch 1999, Gollub 1991). On the other hand, vortical wakes shed off the oil pipes submerged into the water induce vibrations in the presence of the strong current. The resultant large amplitude oscillations caused by oscillatory forces can lead to failure of structures. Vortex dipoles are formed in a viscous fluid

when a force is applied locally to some volume of fluid. In what follows, the theoretical framework for flows generated by localized forces is presented.

2.1.1 Stokes solution

Consider a two-dimensional planar flow in a viscous incompressible fluid induced by a localized forcing. The fluid extends to infinity and is initially at rest. A momentum source is located at the origin of the coordinate system. The momentum source starts acting at time t=0 and thereafter exerts on the fluid the kinematic momentum flux (force per unit mass and unit depth) equal to $J = const.$ The dimensions of J are $[J] = L^3T^{-2}$, where L and T are the units of length and time. An impulsive source which acts for a short period of time delivering finite kinematic momentum $I([I] = L^3T^{-1})$ will be considered as well. The balance of momentum and the equation of continuity for a fluid with singularity at the origin can be presented in the form:

$$\frac{\partial \vec{u}}{\partial t} + \left(\vec{u} \cdot \vec{\nabla}\right) \vec{u} = -\frac{1}{\rho}\vec{\nabla}p + \nu\nabla^2\vec{u} + \vec{A}\delta(\vec{x}), \tag{2.1}$$

$$\nabla \cdot \vec{u} = 0, \tag{2.2}$$

where $\vec{u}$ is the velocity vector, p is pressure, ν is the kinematic viscosity, $\vec{x}$ the position vector and $\delta(\vec{x})$ is the Dirac delta-function. The vector $\vec{A}$ represents the force of magnitude $J \cdot H(t)$ or $I \cdot \delta(t)$ applied in the positive direction along the x-axis. Here H(t) is the Heaviside step-function.

The dimensionless amplitudes of forcing in the following form:

$$Re_J = \frac{Jt^{1/2}}{\nu^{3/2}}, \qquad Re_I = \frac{I}{\nu^{3/2}t^{1/2}}, \tag{2.3}$$

have the physical meaning of the Reynolds number of the flow (Cantwell 1986, Voropayev and Afanasyev 1994). Note, that there is no natural length scale in the problem since the momentum source is a point source. A force acting at the origin generates

dipolar vorticity in the vicinity of the origin. This vorticity is advected by the induced flow and diffuses. The far field of the flow is approximately irrotational (potential). The velocity in this region establishes instantaneously (in an incompressible fluid) according to the momentum equation at large $|\vec{x}|$

$$\frac{\partial \vec{u}}{\partial t} + \frac{1}{\rho}\vec{\nabla} p = 0, \tag{2.4}$$

The pressure field can be found by taking the divergence of 2.1 and employing the fact that in two-dimensions $2\pi\delta(\vec{x}) = -\nabla^2 log|\vec{x}|$. Taking into account the continuity equation 2.2 and neglecting the nonlinear terms which are small at large $|\vec{x}|$ (e.g. Cantwell, 1986), one arrives at the Poisson equation

$$\nabla^2 \left(\frac{p}{\rho} + \frac{\vec{A}}{2\pi} \nabla log|\vec{x}| \right) = 0. \tag{2.5}$$

The particular solution is easy to find

$$\frac{p}{\rho} = \frac{\vec{A} \cdot \vec{n}}{2\pi|\vec{x}|} = |\vec{A}| \frac{\cos\theta}{2\pi r} = |\vec{A}| \frac{x}{2\pi(x^2+y^2)}, \tag{2.6}$$

where $\vec{n} = \frac{\vec{x}}{|\vec{x}|}$ is the unit vector, and polar coordinates are used. As can be seen from (2.6), the pressure instantaneously arises in the fluid and does not change with time for the continuous source, while for impulsive source there is a pressure impulse at $t = 0$ and the pressure is zero at $t > 0$. The potential velocity distribution can then be obtained by integrating (2.4) with respect to time as follows:

$$\vec{u} = -Jt \frac{1}{2\pi} \vec{\nabla} \left(\frac{x}{x^2+y^2} \right), \qquad (continuous \quad source) \tag{2.7}$$

$$\vec{u} = -I \frac{1}{2\pi} \vec{\nabla} \left(\frac{x}{x^2+y^2} \right), \qquad (impulsive \quad source), \tag{2.8}$$

For small Reynolds numbers the momentum equation 2.1 can be linearized to obtain the equation in the Stokes' approximation. The equation for vorticity in this approximation is of the form of the heat diffusion equation and can be solved for different

configurations of point forces (e.g. Cantwell, 1986, Voropayev and Afanasyev, 1994). The relation for pressure 2.4 can be used to relate the flow characteristics to the forcing amplitude (Voropayev et al., 2003). The particular solutions for the two cases of interest give vorticity and stream-function as follows:

$$\omega(x,y,t) = \frac{J\sin\theta}{2\pi\nu r} e^{-\frac{r^2}{4\nu t}} \quad ,$$

$$\Psi(x,y,t) = \frac{Jr\sin\theta}{8\pi\nu}\left[\frac{4\nu t}{r^2}\left(1-e^{-\frac{r^2}{4\nu t}}\right) + \int_{\frac{r^2}{4\nu t}}^{\infty} e^{-\zeta}\zeta^{-1}d\zeta\right] \tag{2.9}$$

(for the continuous source) and

$$\omega(x,y,t) = \frac{Ir\sin\theta}{8\pi(\nu t)^2} e^{-\frac{r^2}{4\nu t}},$$

$$\Psi(x,y,t) = \frac{I\sin\theta}{2\pi r}\left(1-e^{-\frac{r^2}{4\nu t}}\right) \tag{2.10}$$

for the impulsive source.

It was demonstrated that these solutions describe reasonably well the growth of the vortex dipole for small values of the Reynolds numbers. They fail however to describe the translational motion of the vortex dipole which is clearly due to nonlinear effect of advection. The linear solution is in fact a first order term of the expansion of the full solution of the original equation 2.1 in terms of a small parameter, namely the dimensionless forcing amplitude (Reynolds number). The linear solution can be improved if the next term in the expansion is added thus rendering a weakly nonlinear solution. This second order term is quadratic in Reynolds number and is proportional to $\sin 2\theta$ (Voropayev and Afanasyev, 1994). The weakly nonlinear solution allows the vortex dipole to drift forward. This solution, however, does not correctly describe the velocity of propagation of the dipoles for moderate and large values of the Reynolds numbers.

2.1.2 The Oseen approximation

Here, we attempt to obtain a solution which is a good approximation at moderate Reynolds numbers. The Oseen approximation will be used for this purpose. This approximation was introduced as a correction to the Stokes solution for steady flow around a circular cylinder where the linearized advection term in the form $(\vec{U} \cdot \vec{\nabla})\vec{u}$ is added to the Stokes equation (see e.g. Batchelor, 1967). Here $\vec{U}$ is the spatially uniform velocity of the stream. In this approximation, the vorticity is advected by the flow and diffuses. In our problem, however, the velocity of the stream around the source where the vorticity is generated is not spatially uniform and is, in general, time-dependent. An approximation similar to that of Oseen was used when solving for a weakly nonlinear flow (Voropayev and Afanasyev, 1994). Second order equations in this approximation contain a linearized advection term where $\vec{u}$ is the second order velocity and $\vec{U}$ is the first order velocity obtained by solving the first order (Stokes) equations. In this approximation the first order stream advects the second order vorticity. Here we hypothesize that instead of using the first order (viscous) velocity field we can employ the potential velocity to build the solution using the Oseen approximation. We further simplify the problem by considering the advecting stream to be spatially uniform (but still time dependent). The velocity of the stream is given by the value of the x-component of potential velocity (in the direction of forcing) at the x-axis. We will demonstrate by comparing the solutions obtained in this approximation with the results of direct numerical simulations of vortex dipoles (Sec. III), that this hypothesis provides us with a reasonable approximation for moderate Reynolds numbers.

The equation for the vorticity in the Oseen approximation is the advection-diffusion equation

$$\frac{\partial \omega}{\partial t} + U\frac{\partial \omega}{\partial x} = \nu\left(\frac{\partial^2 \omega}{\partial x^2} + \frac{\partial^2 \omega}{\partial y^2}\right). \tag{2.11}$$

This equation describes the diffusion and advective transport of vorticity generated by a momentum source in the stream of uniform velocity U. This problem is, of course, equivalent to a diffusion problem for a source moving with velocity $-U$ in the negative direction along x-axis. To demonstrate this, consider the coordinate system (x', y', t') fixed in a fluid at rest. The diffusion of vorticity from a moving source is then described by simple diffusion equation

$$\frac{\partial \omega}{\partial t} = \nu \left(\frac{\partial^2 \omega}{\partial x'^2} + \frac{\partial^2 \omega}{\partial y'^2} \right). \tag{2.12}$$

The transformation of the coordinates

$$x = x' + Ut',$$

$$y = y',$$

$$t = t'.$$

allows us to rewrite 2.12 in the coordinate system (x, y, t) where the source is always at the origin. It is assumed here that U is constant in time. The transformed form of 2.13 is identical to 2.11. Fortunately, it is not necessary to solve equation 2.11 from scratch when the solution 2.9, 2.10 for the impulsive (stationary) source is known. In fact, due to the linearity of the equations 2.11 or 2.12, the effects of vorticity generation by the moving source at different times can be superposed directly. For a source in the stream, the vorticity distribution at any time can be found by integration of previous distributions. Similar problems are routinely solved in heat conduction theory for such applications as laser cutting (e.g. Easterling, 1983). The source in the heat conduction problems is different though than those considered here. The heat source is usually a symmetric source without angular dependence and it would correspond therefore to a vorticity monopole. In our problem, the forcing creates a dipolar distribution of vorticity. Apart from this minor difference, the solution of the

problem is the same in both cases. The distribution of vorticity for the continuous source of magnitude J starting at $t = 0$ is obtained by integration over the solution for the impulsive source (see e.g. Farlow, 1993). Formally, this integration for both vorticity and stream function can be expressed as follows:

$$\begin{bmatrix} \omega_J \\ \psi_J \end{bmatrix}(x,y,t) = \int_0^t \begin{bmatrix} \omega_I \\ \psi_I \end{bmatrix}(x - U(t-\tau), y, t-\tau)d\tau. \tag{2.13}$$

Substituting the expression 2.10 for vorticity of the impulsive force, one arrives at

$$\omega(x,y,t) = \frac{Jy}{8\pi\nu^2}\int_0^t \frac{1}{(t-\tau)^2}\exp\left[-\frac{[x-(t-\tau)U]^2+y^2}{4\nu(t-\tau)}\right]d\tau. \tag{2.14}$$

Similar integration can be performed to obtain the stream function of the flow using 2.10

$$\Psi(x,y,t) = -\frac{Jy}{2\pi}\int_0^t \frac{1-\exp\left[-\frac{[x-(t-\tau)U]^2+y^2}{4\nu(t-\tau)}\right]}{[x-(t-\tau)U]^2+y^2}d\tau, \tag{2.15}$$

since the equation for the stream function is linear as well. Here the minus sign is taken to describe the forcing in the negative x direction.

Consider now the starting vortex dipoles generated either by a continuous or an impulsive forcing. The x-component of the potential velocity 2.7 or 2.8 at $y = 0$ can be integrated with respect to time to give the displacement of the vortex dipole with time for continuous and impulsive sources respectively:

$$L(t) = \left(\frac{3J}{4\pi}\right)^{1/3} t^{2/3}, \tag{2.16}$$

$$L(t) = \left(\frac{3I}{2\pi}\right)^{1/3} t^{1/3}. \tag{2.17}$$

The transformation of coordinates from the (primed) coordinate system where the source is moving to the coordinate system where it is fixed at the origin can be modified as following:

$$x = x' - L(t).$$

The solution for the continuous source similar to 2.14, 2.15 can then be easily obtained in the integral form:

$$\omega(x,y,t) = \frac{Jy}{8\pi\nu^2}\int_0^t \frac{1}{(t-\tau)^2}\exp\left[-\frac{[x-L(t-\tau)]^2+y^2}{4\nu(t-\tau)}\right]d\tau. \tag{2.18}$$

$$\Psi(x,y,t) = -\frac{Jy}{2\pi}\int_0^t \frac{1-\exp\left[-\frac{[x-L(t-\tau)]^2+y^2}{4\nu(t-\tau)}\right]}{[x-L(t-\tau)]^2+y^2}d\tau, \tag{2.19}$$

where $L(t)$ is defined by 2.16.

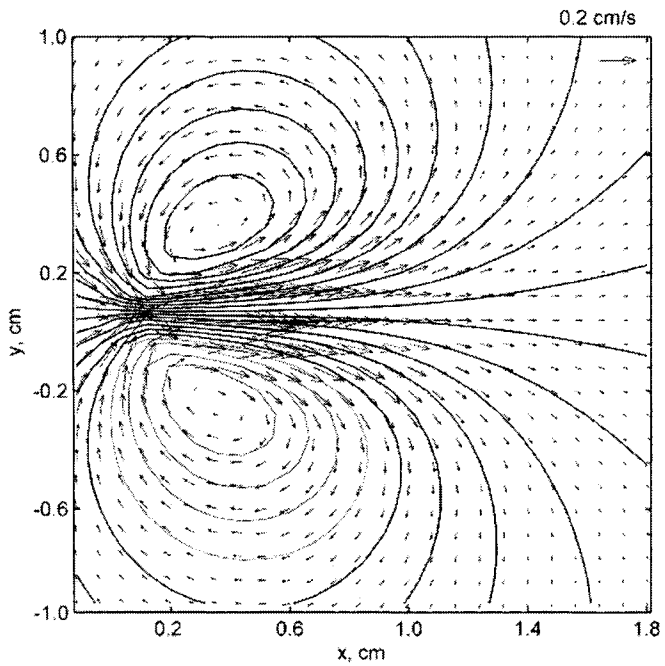

Figure 2.1: Velocity field (arrows) and instantaneous stream function (contours) calculated from 2.15 for $J = 0.05\,cm^3/s^2$ at $t = 5\,s$.

The solution for the impulsive dipole can be obtained by performing a simple transformation of the x-coordinate in the expressions 2.9, 2.10 where $L(t)$ is given by

2.17. We don't need to integrate in this case because vorticity is only generated at $t = 0$. Instantaneous streamlines calculated from 2.19 and the velocity field obtained by differentiation of 2.19 with respect to x and y demonstrate a typical pattern of the dipolar flow Fig. 2.1.

In experiments, some passive tracer (usually a dye) is used to visualize the flow pattern. It is useful therefore to visualize the theoretical results in the same way. If the velocity components are known, it is possible to calculate the distributions of the marked particles at different times integrating the equations of motion for marked particles:

$$\frac{dx_p}{dt} = u(x, y, t), \quad \frac{dy_p}{dt} = v(x, y, t). \tag{2.20}$$

Such a system of ordinary differential equations where the right hand side is known can be easily solved numerically using standard solvers available in various applied mathematical software packages. It is important however to specify initial conditions for the marked particles such that the calculations closely reproduce the experiments.

We performed numerical integration of 2.20 for the case of continuous dipole where the velocity components were obtained by differentiation of 2.15. In our calculations we launched 30 particles from the circle of radius $r = 0.1\,cm$ with the center at the origin. The endpoints of the trajectories of all the injected particles at any time t gave the outline of the front of the dyed fluid ("hat of the mushroom"). The second series of particles was launched continuously at intervals $0.1\,s$ from one point of the circle. These particles gave the outline of the side surface of the dyed fluid ("leg of the mushroom"). A sequence of images in Fig. 2.2 shows that our theoretical solution generates a typical pattern of dyed fluid observed both in laboratory experiments and numerical simulations of vortex dipoles.

In Chapter 3 we perform the quantitative comparison of the theoretical results obtained here for continuous and impulsive vortex dipoles with direct numerical simu-

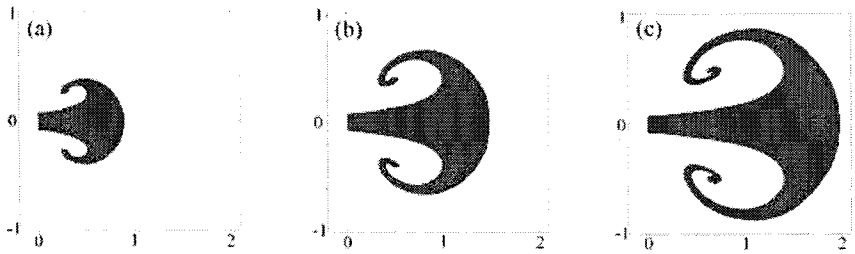

Figure 2.2: A succession of calculated images showing the continuous vortex dipole. The values of control parameters in the model are: $\rho = 1\, gcm^{-3}$, $\nu = 0.01\, cm^2 s^{-1}$ and $J = 0.05\, cm^3 s^{-2}$. Time $t = 5$ (a), 10 (b), 15 (c) seconds. The motion of marked particles is simulated using the solution 2.15. Scale in cm.

lations to show the validity of the hypothesis on the translational speed of the dipoles which is used here to introduce the Oseen approximation.

2.2 Vortical structures in a uniform stream

2.2.1 Drag wake behind localized force

Consider now a two-dimensional planar flow in a viscous incompressible fluid induced by a single localized forcing. A momentum source is located at the origin of the coordinate system in the stream of uniform velocity U in positive x-direction. The system is described by the Navier-Stokes equation which does not have singularities except at the origin. However, if one is interested in flow, far from the source, the equation for the vorticity in the Oseen approximation is the diffusion-advection equation 2.11.

In this case U will represent the spatially uniform velocity of the free stream. The solution of this equation in general form was obtained earlier 2.13. Neglecting the 'end effects' (the start-up of the flow), we can obtain steady-state solution by letting $t \to \infty$ in the equation 2.14. The solution of equation (2.11) for the momentum source acting in the negative x-direction is then given by:

$$\omega(x,y) = -\frac{JU}{4\pi\nu^2}\frac{y}{\sqrt{x^2+y^2}}\exp\left(\frac{Ux}{2\nu}\right)K_1\left(\frac{U}{2\nu}\sqrt{x^2+y^2}\right), \tag{2.21}$$

where $K_1(z)$ is the modified Bessel function of the second kind. The corresponding vorticity distribution is shown on the Fig 2.3.

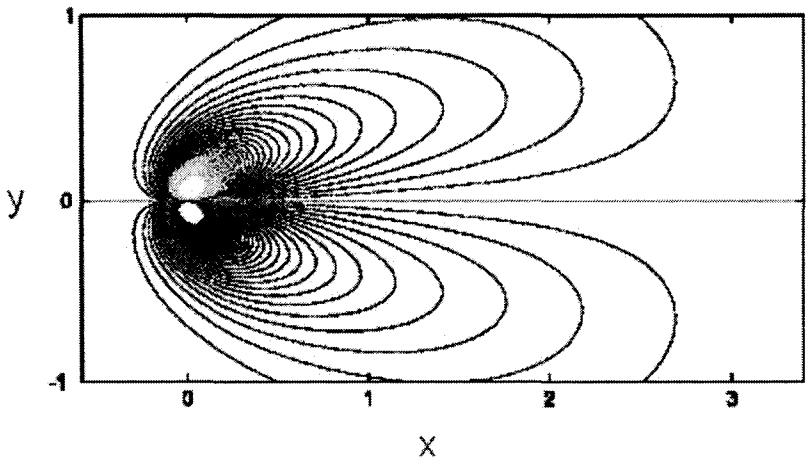

Figure 2.3: Vorticity field of the 2D flow generated by a single force in a uniform stream for $J = 0.01\,cm^3s^{-2}$, $U = 0.1\,cm/s$, $\nu = 0.01\,cm^2s^{-1}$, $t = 25\,s$. Contours are from -1 to 1 s^{-1} with the interval $0.02\,s^{-1}$. Scale in cm.

A similar integration can also be performed to obtain the stream function of the

flow:

$$\psi(x,y) = -\frac{Jy}{2\pi}\int_0^\infty \frac{1-\exp\left[-\frac{x'^2+y^2}{4\nu\zeta}\right]}{x'^2+y^2}d\zeta. \tag{2.22}$$

Here we use the notation $x' = x - U\zeta$. Expressions (2.21) and (2.22) describe the far wake behind a body (e.g. a cylinder) submerged into a uniformly moving fluid. The force represents a net reaction force applied by the body on the fluid whose magnitude is equal to the drag force.

It is also useful to consider the x velocity component, which can be obtained by differentiation of (2.22) as follows:

$$u(x,y) = -\frac{J}{\pi}\int_0^\infty \left[\frac{\left(1-e^{-\frac{x'^2+y^2}{4\nu\zeta}}\right)y^2}{\left(x'^2+y^2\right)^2} + \frac{\left(1-e^{-\frac{x'^2+y^2}{4\nu\zeta}}\right)}{2\left(x'^2+y^2\right)} + \frac{y^2 e^{-\frac{x'^2+y^2}{4\nu\zeta}}}{4\nu\zeta\left(x'^2+y^2\right)}\right]d\zeta. \tag{2.23}$$

The explicit expression for the distribution of u along the x-axis can be obtained after integration in the form:

$$u(x,y=0) = \frac{J}{4\pi\nu\tilde{x}}\left[1-\tilde{x}\exp\tilde{x}\left(K_0(|\tilde{x}|)+K_{-1}(|\tilde{x}|)\right)\right], \tag{2.24}$$

where $\tilde{x} = \frac{Ux}{2\nu}$. For large negative $\tilde{x}$ we obtain the asymptotic relation:

$$u(x) = \frac{J}{2\pi U x}. \tag{2.25}$$

Equating (2.25) to $-U$, one can obtain the position of the stagnation point in front of the momentum source:

$$x_s = \frac{J}{2\pi U^2}. \tag{2.26}$$

This expression will be used in the next Section to derive the relation between the forcing amplitude J and the stream velocity U which gives the boundary separating the two different regimes of instability of the flow.

2.2.2 Zero-momentum wake behind force doublet

Since 2.21 is a linear solution, the flow induced by two forces acting in opposite directions, is given by a superposition:

$$\omega_2(x,y) = \omega(x,y) - \omega(x-\delta,y), \tag{2.27}$$

where δ is the distance between the forces. The vorticity field (2.27) is in the form of two vortex dipoles of opposite signs which are "stretched" by the incoming stream (Fig. 2.4 a).

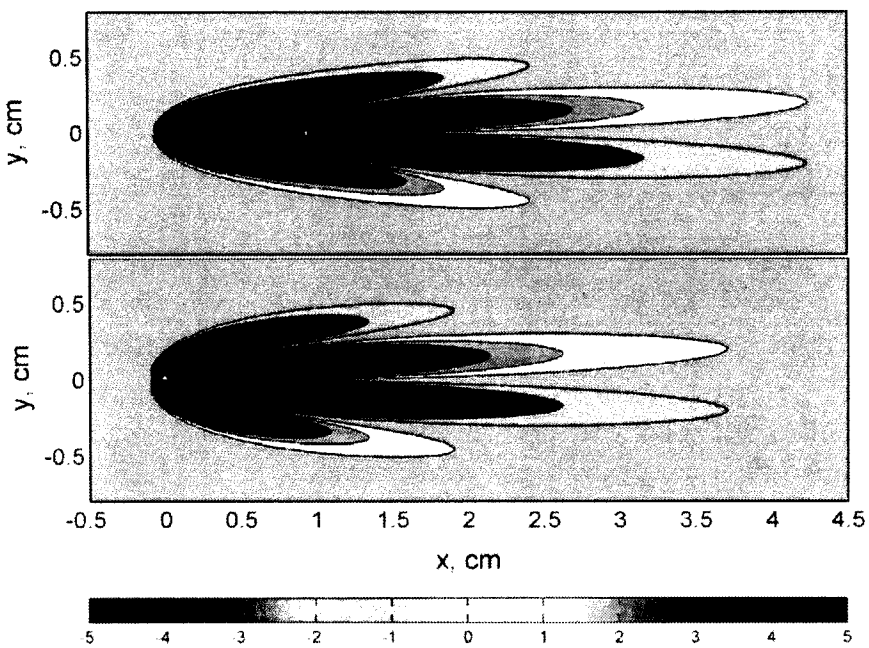

Figure 2.4: Vorticity contours for a continuous vortex dipole calculated from the theoretical relations (2.27) and (2.28). Contours are from -5 to 5 s^{-1}. $J = 1\,cm^3 s^{-2}$, $\delta = 1\,cm$, $Q = 1\,cm^4/s^2$, and $\nu = 0.01\,cm^2 s^{-1}$.

In the limit when two point forces are very close to one another, or alternatively the flow at a larger distance from the origin is considered, a force doublet Q can be introduced such that $Q = \lim_{\delta \to 0, J \to \infty} J\delta$. The unsteady solution for the flow induced by a force doublet which starts at $t = 0$ is given in the form of an integral (Afanasyev 2004):

$$\omega_Q(x, y, t) = \frac{Qy}{16\pi\nu^3} \int_0^t \frac{x - (t-\tau)U}{(t-\tau)^3} exp\left[-\frac{[x-(t-\tau)U]^2 + y^2}{4\nu(t-\tau)}\right] d\tau. \tag{2.28}$$

For the steady-state case this expression can be integrated to give:

$$\omega_Q(x, y) = \frac{QU^2 y}{8\pi\nu^3 r} exp\left(\frac{Ux}{2\nu}\right)\left[-K_1\left(\frac{rU}{2\nu}\right) + \frac{x}{r}K_2\left(\frac{rU}{2\nu}\right)\right], \tag{2.29}$$

where $r = \sqrt{x^2 + y^2}$. The vorticity field 2.29 is shown in Fig. 2.4 b. The profiles of vorticity in the wake (Fig. 2.5) show that vorticity changes sign at the axis of the flow as well as at some distance from the axis symmetrically. It is interesting to compare the vorticity profiles given by 2.29 and by 2.27 at some downstream location which is not too far from the origin so that the finite distance between the forces can be a significant factor. Fig. 2.5 depicts the profiles of vorticity across the wake for both cases at two downstream locations x = 3 and 6 cm. While at the closer location the profiles differ significantly in amplitude, at the further location the difference is much smaller and at still further downstream it becomes negligible.

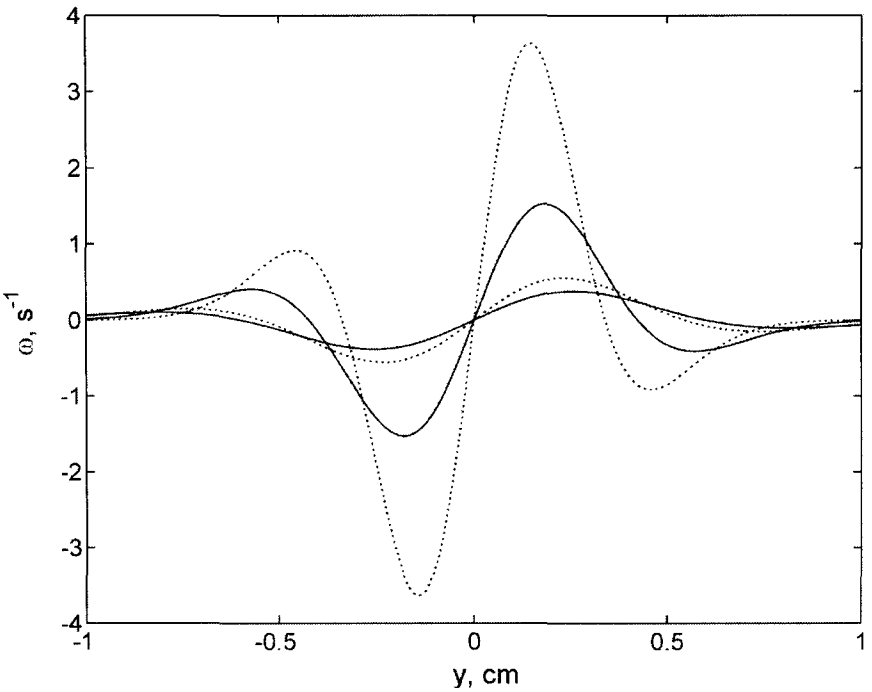

Figure 2.5: Vorticity profiles across the wake at two locations x = 3 (larger amplitude) and 6 cm (smaller amplitude). Control parameters are the same as those in Figure 2.4. The solid line is for the force doublet (2.28) while the dashed line is for the flow induced by two separate forces (2.27). In the latter case the distance in x-direction is measured from the point in the middle between the two forces.

Chapter 3

Starting Dipole Flow: numerical simulations and laboratory experiments

3.1 Introduction

In the following sections results of the numerical simulations of the starting vortex dipoles are reported and compared to the theoretical analysis presented in Chapter 2.

3.2 Numerical work and results

A series of two-dimensional numerical simulations that document the dipolar flow generated by a localized forcing has been performed using commercial computational

fluid dynamics code Fluent 5.5.14 on the SGI Onyx 3400 computer. Finite element method simulations were carried out using a Navier-Stokes solver. The computational domain of dimensions 60 cm x 30 cm was used in our simulations and free-slip boundary conditions were applied at the walls to model the experiments in a laboratory tank. The domain was large enough though to neglect the effect of the walls on the flow during the entire period of the flow evolution (10 - 50 s). The test of the effect of the walls on the flow is presented in the Appendix A. The domain was filled with an unstructured grid consisting of 85,000 triangular elements with a minimum mesh size of 0.027 cm. The size of the elements was smaller near the origin where the momentum source was located. The working fluid was water of density $\rho = 0.998\, g/cm^3$ and kinematic viscosity $\nu = 0.01\, cm^2/s$. A localized force J was applied to a fluid in a circle of radius $a = 0.1 - 0.5\, cm$ such that the force density F (force per unit area) is described by the Gaussian distribution $F = F_0\, exp(-r^2/a^2)$. The amplitude of the force F_0 and the radius of the circle a were varied in our simulations. In Fluent the action of the force was implemented using the UDF (User Defined Function) to specify the momentum source in the x direction. The time step was fixed during all simulations and was $dt = 0.05$s.

To analyze the results of numerical simulations, it is useful to perform simple dimensional analysis of the control parameters involved in the problem. Consider the distance L traveled by a dipole measured from the origin to the centers of the vortices of the dipole measured along the x-axis. L depends on the set of four dimensional quantities including kinematic viscosity ν , time t, the amplitude of forcing J (or I for the impulsive dipoles) and the size of the region where the force is applied, a. Dimensional analysis then gives

$$L = \left(\frac{3J}{4\pi}\right)^{1/3} t^{2/3} \Phi\left(\frac{Jt^{1/2}}{\nu^{3/2}}, \frac{Ja}{\nu^2}\right), \tag{3.1}$$

$$L = \left(\frac{3I}{2\pi}\right)^{1/3} t^{1/3} \Phi\left(\frac{I}{\nu^{3/2} t^{1/2}}, \frac{I}{a\nu}\right), \tag{3.2}$$

Simulations	J, cm^3/s^2	I, cm^3/s	a, cm	n	aJ/ν^2	$I/a\nu$	c
Continuous							
1	0.05		0.2	0.66	100		0.23
2	0.126		0.2	0.66	100		0.23
3	0.5		0.1	0.66	126		0.37
4	0.05		0.2	0.65	1000		0.64
5	1.0		0.2	0.67	2000		1.1
Impulsive							
6		0.63	0.1	—		630	—
7		15.75	0.5	0.35		3140	2.6
8		12.6	0.2	0.34		6300	2.2
9		18.8	0.2	0.34		9400	3.1

Table 3.1: Numerical simulations for impulsive and continuous starting dipoles.

where the numerical coefficients has been introduced to match these expressions with those for potential flow 2.16, 2.17. Φ is an unknown function of two dimensionless arguments. The first argument $\Pi_1 = \frac{Jt^{1/2}}{\nu^{3/2}}$ ($\Pi_1 = \frac{I}{\nu^{3/2}}t^{1/2}$) of the function Φ includes viscosity and is effectively the Reynolds number of the flow. It is time dependent and grows with time for continuous dipoles and decreases for impulsive dipoles. The second argument $\Pi_2 = \frac{Ja}{\nu^2}$ ($\Pi_2 = \frac{I}{a\nu}$) includes a, and represents the effect of the finite size of the source. Several simulations with different values of the amplitude of forcing and the size of the source were performed for continuous and impulsive sources. The main control parameters of the simulations are summarized in Table 3.1.

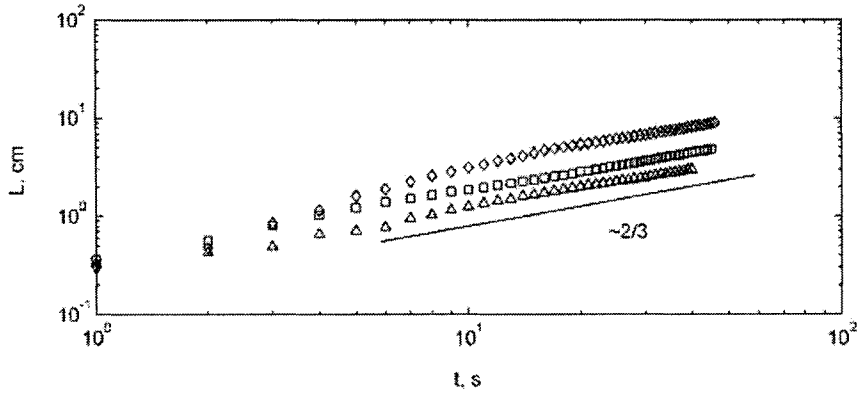

Figure 3.1: Distance L for continuous dipoles for simulations 1 (triangles), 2 (squares) and 3 (diamonds) in Table 3.1.

Measurements of the distance traveled by the dipoles (Fig. 3.1, 3.2) demonstrate that the asymptotic regime of the flows is characterized by the time dependence $L \sim t^n$, where $n = 2/3$ for continuous dipoles and $n = 1/3$ for impulsive dipoles in accord with those values predicted by 2.16, 2.17.

Measured exponents for the numerically simulated flows are $n = 0.66 \pm 0.01$ (continuous) and $n = 0.34 \pm 0.01$ (impulsive). These results allow us to make a conclusion about the asymptotic behavior of function in 3.1, 3.2 for large values of its first argument. To satisfy the results of the measurements this function must not depend on time therefore we can assume complete similarity of this function with respect to Π_1.

$$\Phi\left(\frac{Jt^{1/2}}{\nu^{3/2}} \to \infty, \frac{Ja}{\nu^2}\right) = G\left(\frac{Ja}{\nu^2}\right), \tag{3.3}$$

$$\Phi\left(\frac{I}{\nu^{3/2}t^{1/2}} \to \infty, \frac{I}{a\nu}\right) = G\left(\frac{I}{a\nu}\right), \tag{3.4}$$

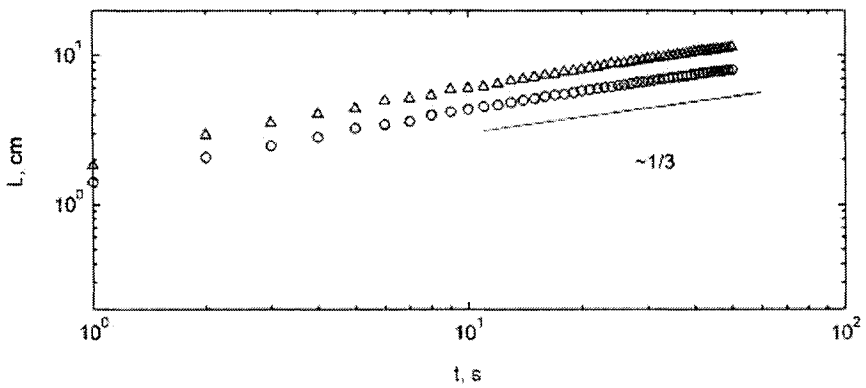

Figure 3.2: Distance L for impulsive dipoles for simulations 7 (triangles) and 8 (circles) in Table 3.1.

For impulsive dipoles, Π_1 decreases with time and the asymptotic regime can be expected to exist only for intermediate times when Π_1 is still large. At large times, a viscous regime should be established in this case. The values of the coefficient c in the dependence $L = ct^{2/3}$ ($L = ct^{1/3}$) were then measured and compared with the theoretically predicted values of the coefficient $c_t = (3J/4\pi)^{1/3}$ ($c_t = (3I/2\pi)^{1/3}$). The graph in Fig. 3.3 for continuous dipoles demonstrate that the measured coefficient approaches the theoretical value for the simulations where the parameter $\Pi_2 = \frac{I}{a\nu}$ is relatively small. This corresponds to more concentrated (smaller a) and weaker source (smaller J). The asymptotic behavior of the function G therefore can be characterized as a complete similarity of this function with respect to its argument for small values of the argument

$$G\left(\frac{Ja}{\nu^2} \to 0\right) \to 1.$$

The values of the coefficient c for impulsive dipoles are given in Table 3.1. They

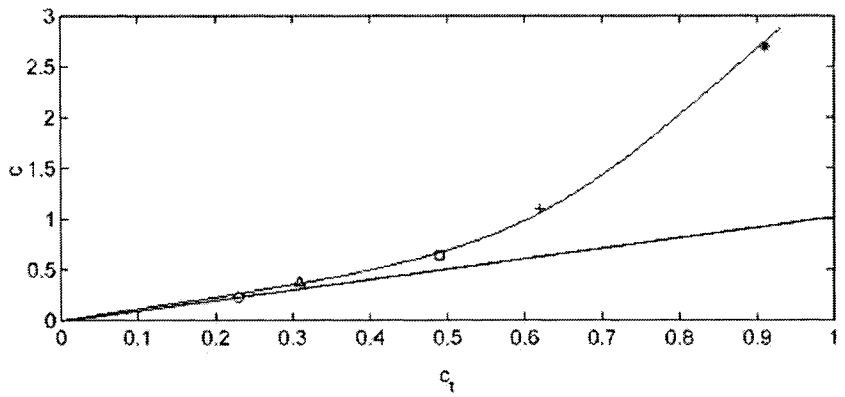

Figure 3.3: Coefficient c measured in the simulations 1 (circle), 2 (triangle), 3 (square), 4 (plus) and 5 (star) versus the theoretical values of the coefficient. Solid line is $c = c_t$.

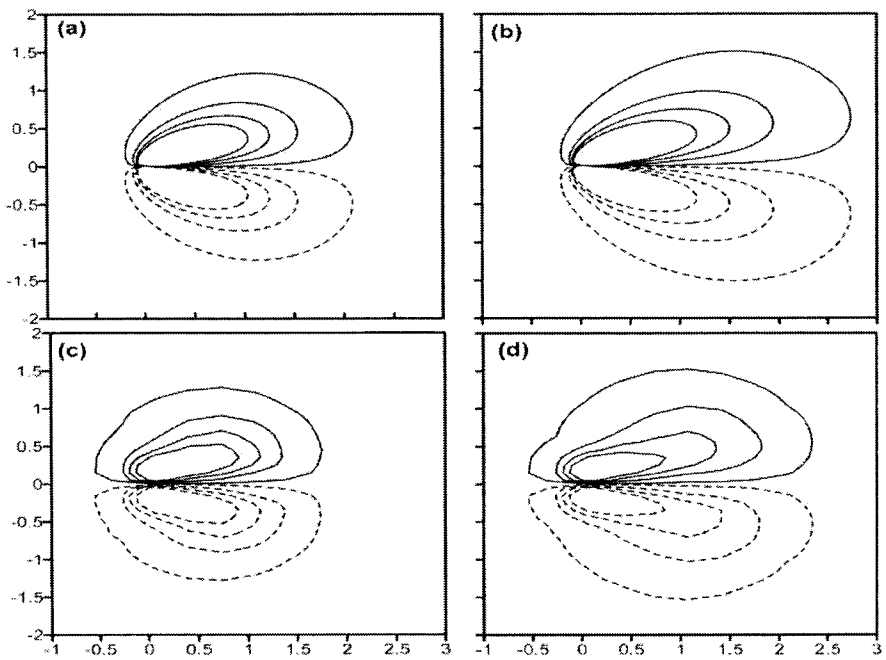

Figure 3.4: Vorticity contours for a continuous vortex dipole: (a), (b) calculated from the theoretical relation 2.18 and (c), (d) are obtained in numerical simulation 1 (Table 3.1). Contours are from -0.65 to 0.65 with the interval $0.2\,s^{-1}$. $J = 0.05\,cm^3/s^2$, $t = 15\,s$ (a), (c) and $t = 25\,s$ (b), (d). Scale in cm.

indicate a similar property of the function G with respect to $\Pi_2 = \frac{I}{a\nu}$. Surprisingly this also indicates that this asymptotic behavior is achieved for larger values of a in contrast to the case of continuous dipoles where a must be small in order for Π_2 to be small. In the simulation 6 (Table 3.1) where the forcing was very weak, the intermediate asymptotic behavior was not observed. Since the initial Reynolds number of the flow was small the flow was in a viscous regime where no significant translation of the dipole was observed after the time interval of a few seconds. Our numerical simulations demonstrate that global characteristics of the dipole such as the distance L is predicted well by theory. It's also interesting to compare the entire vorticity fields for the numerically simulated dipoles and those given by theory 2.18. Fig. 3.4 shows good quantitative agreement between the simulated dipole and theory.

However, in Fig. 3.5 where similar data is presented for the simulation with higher Π_2 there are visible differences in the pattern of the vorticity distribution. There is a developed dipole in the frontal part of the starting flow in the numerical simulations. This dipole detaches somewhat from the jet flow which establishes behind it and moves faster than it should according to theory. This can be also seen from the fact that the difference between the coefficient c in simulations and in theory increases for larger values of the parameter Π_2 . Note that the predicted exponent in the time dependence $L \sim t^{2/3}$ is still valid for large Π_2 .

3.3 Laboratory experiments

The laboratory experiments reported herein were performed in a system of two thin layers of different density using the electromagnetic method of forcing. This method was chosen to provide the two-dimensionality the flow (see e.g. Paret et. al., 1997). The particular parameters of the system were the same as those in previous exper-

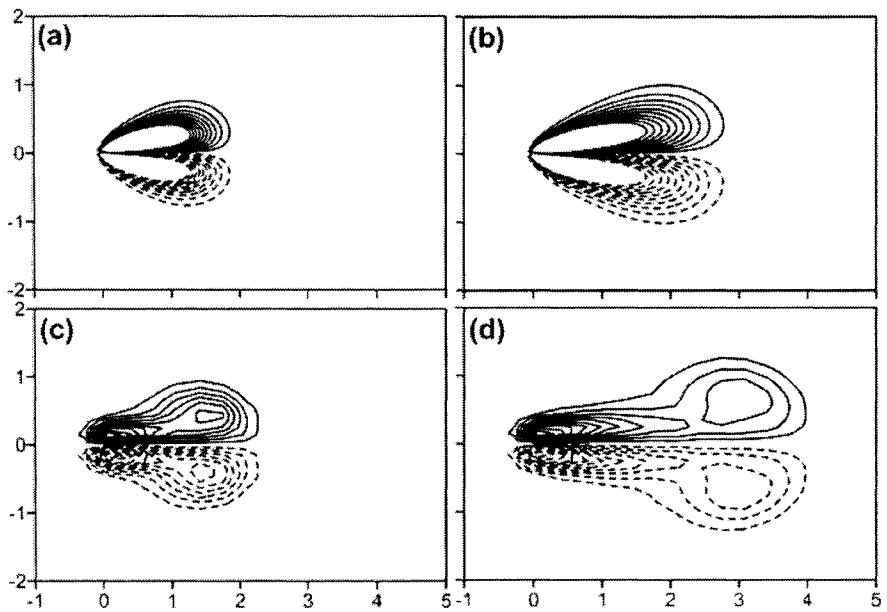

Figure 3.5: Vorticity contours for continuous vortex dipole: (a), (b) calculated from the theoretical relation 2.18 and (c), (d) are obtained in numerical simulation 3 (Table 3.1). Contours are from -5 to 5 with the interval $0.5\,s^{-1}$. $J = 0.5\,cm^3/s^2$, $t = 5\,s$ (a), (c) and $t = 10\,s$ (b), (d). Scale in cm.

iments with two-dimensional turbulence (Afanasyev and Wells, 2005). This system was demonstrated to work well. In particular an important result of that study was the growth of the Reynolds number of the flow which was in agreement with the predictions for the two-dimensional turbulence (e.g. Chasnov, 1997). This growth was previously achieved only for the flows in soap films (Martin et al., 1998). This provides additional evidence of the 2D dynamics of the flow. Two layers were used to minimize the vertical component of velocity. In a thin layer system, bottom friction is an important factor which prevents the flow from being purely two-dimensional. Bottom friction as well as friction due to ordinary viscosity causes the total energy of the flow to decay (e.g. Danilov et al., 2002). It is important therefore to keep the rate of energy decrease due to bottom friction to be somewhat less than that due to ordinary viscosity. It was demonstrated to be the case in Afanasyev and Wells (2005). We assume that this is also true for the present experiments where the magnitude of forcing is similar to that used previously.

The experiments were carried out in a rectangular container of inner dimensions L = 29 cm and W = 21 cm. The container was filled with two layers of salt water of depth 0.5 cm each and of concentration 40 and $250\,g/l$. The flow was forced electromagnetically by imposing an electric current of magnitude 0 - 3 A in the horizontal direction. A rare earth permanent magnet of diameter 0.5 cm was placed flush with the bottom of the container. The magnet produces a magnetic field with a vertical component of approximately 0.09 T. The interaction of the magnetic field with the electric current results in a horizontal force exerted locally on the fluid in the direction perpendicular to the electric current. This localized force generates a vortex dipole (Fig. 3.6). The magnitude of the force can be controlled by varying the current. Parameters of the experiments are summarized in Table 3.2. The flow was visualized by pH-indicator thymol blue and recorded using a digital video camera placed above

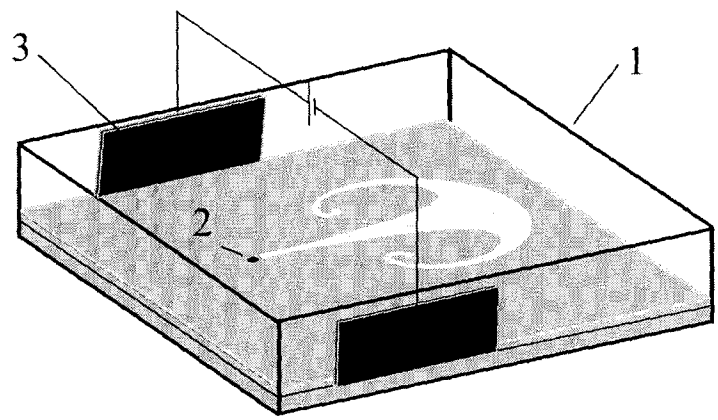

Figure 3.6: Laboratory setup for the investigation of starting dipole flow. Here (1) is rectangular container (2) is the permanent magnet and (3) are electrodes.

Experiment	Current, A	n	c
1	0.3	0.62	0.64
2	0.8	0.60	0.98
3	1	0.65	1.1
4	1.2	0.61	1.2
5	1.4	0.63	1.2
6	1.6	0.67	1.4
7	1.8	0.69	1.6

Table 3.2: Parameter values used in laboratory experiments of continuous starting dipoles.

the container. Geometrical characteristics of the flow were then measured using the individual frames of a video sequence. Measurements of the distance L traveled by the dipoles (Fig. 3.7) gave the results similar to that obtained in numerical simulations. (Fig. 3.1). The measured exponent for the laboratory flows is $n = 0.63 \pm 0.03$ (Table 3.2) for the asymptotic regime of the flow evolution. The values of the coefficient c in the relationship $L = c \cdot t^n$ are given in Table 3.2 and plotted in Fig. 3.8 as a function of current. The magnitude of forcing is proportional to current as is shown in the graph in Fig. 3.8 where the dependence of c on the forcing is in fact demonstrated although we did not measure the absolute value of the forcing parameter J. The graph shows that the growth of c with current is somewhat faster than predicted by theory. This is the result of the finite extent of the forcing region and, most likely, the effect of the bottom friction as well. Bottom friction is comparable with that of the ordinary viscosity in our experiments.

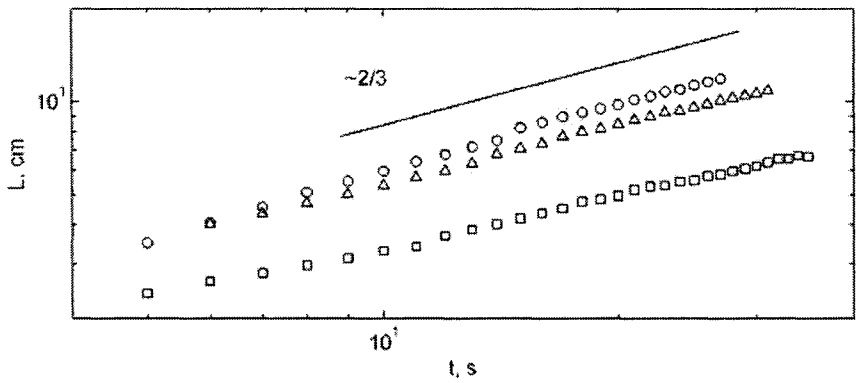

Figure 3.7: Distance traveled L for different times measured for continuous dipoles in the laboratory experiments 1 (squares), 3 (triangles) and 5 (circles) in Table 3.2.

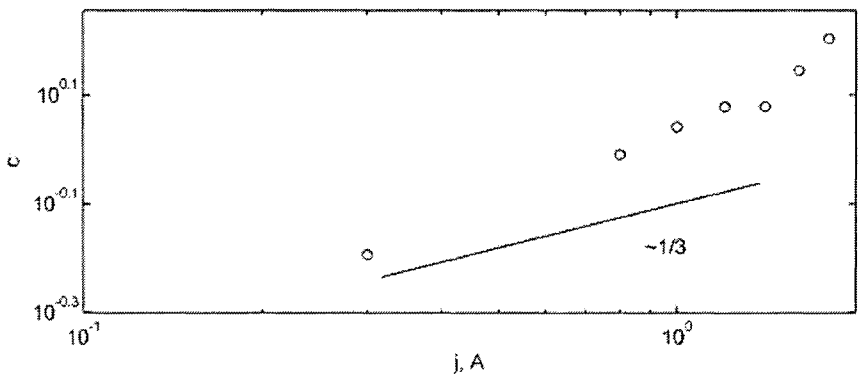

Figure 3.8: Coefficient c ($L = ct^n$) measured in the experiments 1 - 7 (Table 3.2) for different values of the current.

3.4 Discussion and concluding remarks

In summary, it can be concluded that the theoretical analysis based on the formulation of the problem in the Oseen approximation reported in Chapter 2 provides an accurate approximation of the flow for continuous and impulsive starting dipoles. This approach includes the application of the Oseen approximation to the flows generated by localized forcing. Our hypothesis on the velocity of the stream which is required for this approximation turned out to be quite accurate as demonstrated by the quantitative comparison of the theoretical results with the results of our numerical simulations of dipoles as well as with the results of laboratory experiments. The theoretical result which predicts the power law asymptotic behavior of the flow turned out to be especially robust even when additional factors such as the bottom friction in the laboratory experiments affect the flow.

Chapter 4

Wakes and vortex streets behind localized force

4.1 Introduction

The problem of the quantitative description of the characteristics of wakes behind bodies (towed or self-propelled) moving in a viscous fluid arises in many diverse applications including flows of different length scales from millimeters (swimming microorganisms) to kilometers (wakes behind submarines). The characteristics of the drag wakes occurring behind bluff bodies are relatively well studied. In particular the flow around a cylinder which is a benchmark problem in fluid mechanics, has a long history of serious investigation (see comprehensive reviews by Zdravkovitch (1997) and Williamson and Govardhan (2004)).

An idealized problem was formulated in Chapter 2 where the effect of the moving objects is effectively reduced to a combination of spatially localized forces acting

on the fluid. This approach to the wakes behind bluff bodies is justified if one is interested in the flow sufficiently far from the object (far-field flow). A towed object experiences a drag force. The effect of the object on the fluid is therefore described by the force equal to the drag force in magnitude and acting in the opposite direction. Therefore, we can specify the magnitude of the force rather than the size and the details of shape of a particular object and then study the vortical wake generated by such forcing. Besides its important practical application to the far-field bluff body wakes, the problem of the (far- or near-field) wake induced by a force is of interest from the more general fluid dynamical perspective of flows induced by a localized forcing. The flow around a circular cylinder is controlled by three dimensional parameters, namely the diameter of the cylinder d, the velocity of the stream U and the kinematic viscosity of fluid ν. Our problem, where the solid body (cylinder) is simulated by a localized force, contains one additional parameter, the magnitude of the force J (we consider the size,a, of the forcing area to be analogous to the size of the cylinder). Thus, in terms of control parameters, our problem contains an extra degree of freedom and therefore describes a wider class of flows. It is therefore interesting to investigate different regimes of this flow and find a correspondence to the dynamics of the flow around the cylinder.

In this Chapter we focus on the wakes induced by a single force. A similar investigation for the force doublet generating a wake of zero net momentum (self-propelled bodies) will be described in the next Chapter. In two-dimensional flows or quasi-two-dimensional flows that occur in a stratified fluid, wakes become unstable at moderate and high values of the Reynolds number and form typical Karman - Benard vortex streets. In the following sections, the results of a large number of numerical simulations investigating the dependence of the frequency of the vortex shedding on the main control parameters of the flow as well as their comparison with laboratory

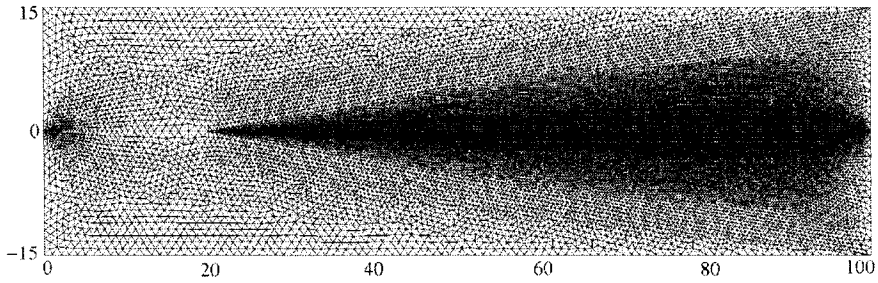

Figure 4.1: Numerical simulation domain.

experiments and the theoretical analysis are described.

4.2 Numerical simulations of a virtual bluff body

A large number of two-dimensional numerical simulations that document the flows generated by a localized momentum source in a uniform stream, have been performed for a wide range of governing parameters. The main control parameters of the simulations are summarized in Table 4.1. The simulations were performed using the commercial computational fluid dynamics code Fluent 5.5.14 on a SGI Onyx 3400 computer. Finite element method simulations were carried out using the Navier-Stokes solver.

A computational domain of dimensions 100 cm x 30 cm was used in our simulations and free-slip boundary conditions were applied at the walls, Fig.4.1. The domain was large enough to neglect the effect of the walls on the flow during the entire period of the flow evolution. The domain was filled with an unstructured grid consisting of 85,000 triangular elements with a minimum mesh size of 0.027 cm. The size of the elements was smaller near the place where the momentum source was located. The working fluid was water of density $\rho = 0.998\, g/cm^3$ and kinematic viscosity

Series	♯ exps,	J, cm^3/s^2	U, cm/s	a, cm	symbol
1	11	1.63-12.5	2.0	0.2	diamond
2	11	1.88-12.5	2.5	0.2	circle
3	36	3.14 -25.17	3.0	0.2	square
4	15	5.35-12.5	3.5	0.2	x-mark
5	22	7.86-12.5	4.5	0.2	star
6	6	3.77	1.5-4	0.2	triangle (right)
7	8	5.035	1.5-5	0.2	triangle (left)
8	10	7.55	1.5-6	0.2	triangle (down)
9	10	12.5	2-6.5	0.2	triangle (up)
10	12	2-46	3.0	0.15-0.7	pentagram
11	12	2.8-62	3.0	0.15-0.7	hexagram
12	12	4-93	3.0	0.15-0.7	filled circle
13	12	7-154	3.0	0.15-0.7	plus

Table 4.1: Numerical simulations for single localized force.

$\nu = 0.01\,cm^2/s$. A localized force J was applied to a fluid in a circle of radius $a = 0.1 - 0.7\,cm$ such that the force density F (force per unit area) is described by a Gaussian distribution. The amplitude of the force F_0 and the radius of the circle a were varied in our simulations. The uniform inflow of velocity $U = 1.5 - 7\,cm/s$ was sustained at the right wall of the domain while the outflow boundary conditions were specified at the left wall. To trigger the instability of the wake a stream was initialized such that for a very short period of time (0.05 s) there was a 5% difference in the velocity in the upper and lower halves of the domain. For the flows where the regular shedding of vortices was observed, we measured the frequency of shedding using the following method. The mean vorticity was calculated for positive values of y along a line located perpendicular to the axis of the flow at x = 23 cm (3 cm downstream of the force). The time series of the vorticity was then analyzed using a Fourier transform to find the shedding frequency.

4.2.1 Results and interpretation

Several series of simulations where one of the control parameters was varied while others were fixed, were performed to study the regime of the flow in the space of three control parameters. In series 1 - 4 (Table 4.1), the momentum flux was varied from $J = 3 - 25\,cm^3/s^2$, in series 6 - 9 the velocity of the stream was varied in the range $U = 1.5 - 6.5cm/s$ and in series 10 - 13 the size of the forcing area was varied, $a = 0.15 - 0.7\,cm$. In the latter case the forcing amplitude J was fixed in each series, while the momentum flux, being proportional to the forcing area, varies as a^2. Figure 4.2 depicts the shedding frequency f measured downstream of the force for simulations with different J in series 1 - 4 while Fig. 4.3 demonstrates the behavior of f as a function of U for simulations with different J in series 6 - 9.

Different regimes of the flow can be identified from these plots. For low values

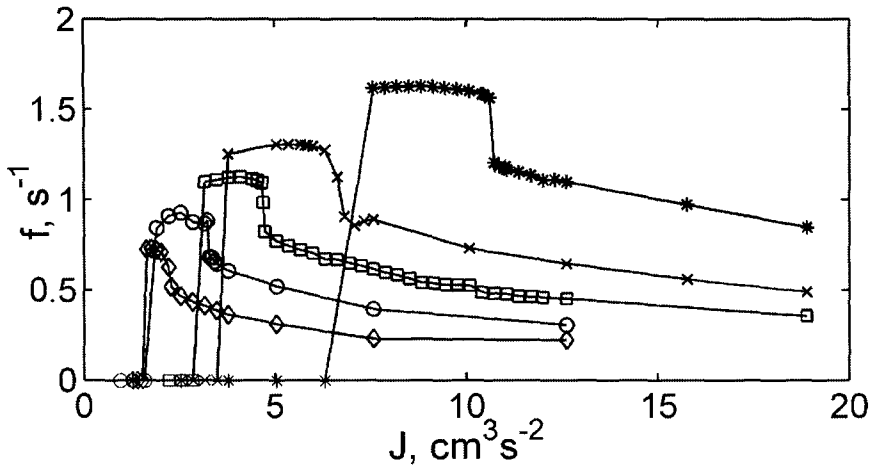

Figure 4.2: Frequency f for different values of J for series 1-4. The legend for symbols is in Table 4.1.

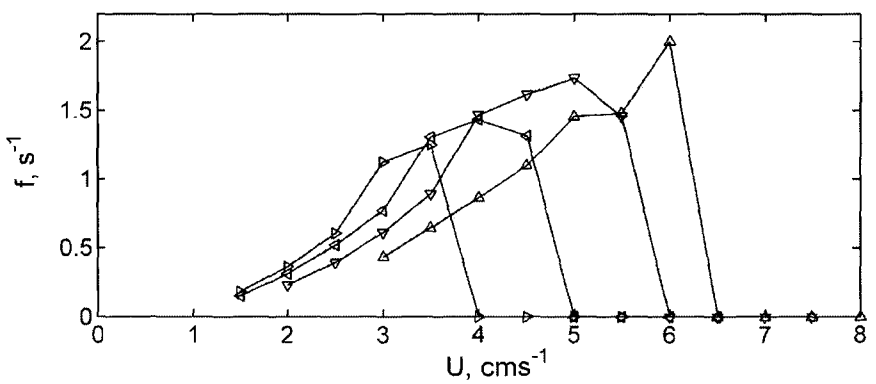

Figure 4.3: Frequency f for different values of U for series 6-9. The legend for symbols is in Table 1.

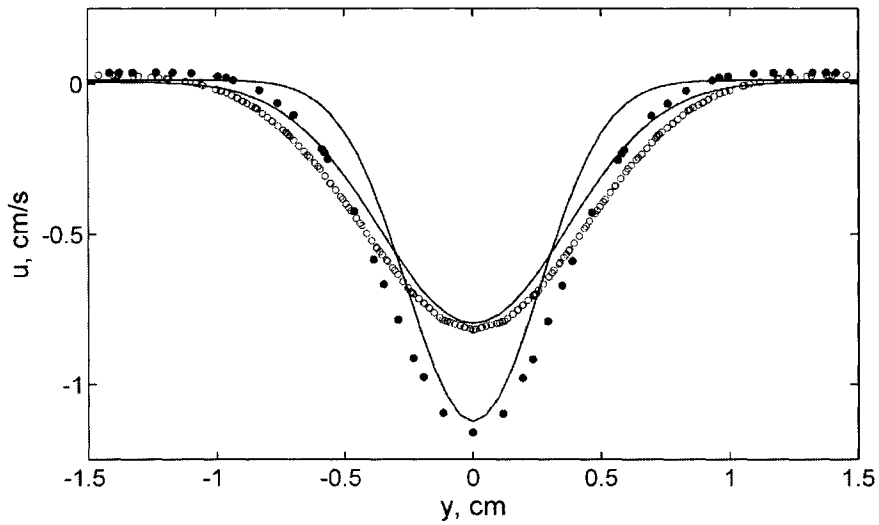

Figure 4.4: Profiles of the x-component of velocity at $x = 15$ and $25\,cm$ from the origin (35 and 45 cm in the computational domain). Theoretical relation 2.24 is shown by solid lines while symbols show the data obtained in numerical simulations: circles (x = 15 cm) and filled circles (x = 25 cm). Control parameters are $J = 2.02\,cm^3/s^2$, $U = 3.0\,cm/s$, $a = 0.2\,cm$.

of J or high values of U the wake is stable (zero shedding frequency). In the stable regime the wake is in the form of an almost parallel flow far downstream of the force. It is interesting to compare the deficit of the x-component of velocity in the wake with the theoretical solution (Afanasyev, 2004) obtained for the point force in the Oseen approximation in Chapter 2, 2.21. Figure 4.4 shows the velocity profiles in a stable wake for one of our simulation together with those calculated from the theoretical relation 2.21. The profiles are given at two locations of 15 and 25 cm downstream of the force. The Reynolds number based on the size of the forcing

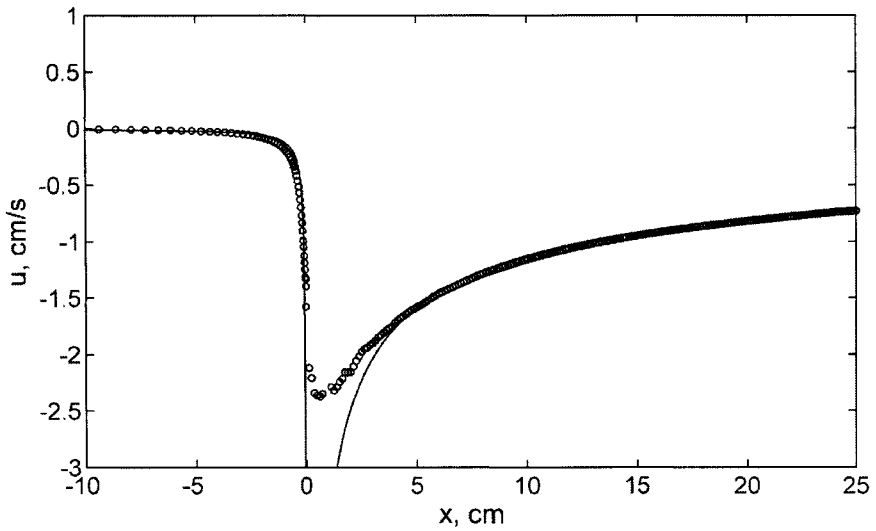

Figure 4.5: Distribution of the x-component of velocity along the axis of the flow ($y = 0$). Theoretical relation 2.24 is shown by solid lines while symbols show the data obtained in numerical simulations. Control parameters are the same as in Figure 4.4.

region for this particular flow is fairly high $Re = 2aU/\nu = 120$. The comparison reveals better agreement for the profiles farther downstream as one might expect. One of the advantages of the solution 2.21 compared to the well known solution obtained from the boundary layer approximation (e.g. Batchelor, 1967) is that 2.24 allows one to determine the velocity upstream of the force. Figure 4.5 demonstrates the distribution of velocity u along the axis of the flow ($y = 0$) in a numerical simulation and that obtained from the steady-state distribution 2.24. The differences between the numerical and theoretical solutions are practically negligible both upstream and downstream of the force except in the area within approximately 3 cm downstream

of the force. It is not clear if the differences in this area because the force in the numerical simulations is applied within a finite area in contrast to point singularity in the theoretical solution or rather to the approximate character of the theoretical solution. The agreement between the solutions might be better if the force in the numerical simulations were applied in a smaller area.

For larger values of J for each series of simulations in Fig. 4.2 we observe nonzero frequencies. The frequency stays almost constant (a plateau in the graph in Fig. 4.2) with varying J in this regime. Regular vortex streets are formed in the wake in this regime. Typical vorticity distributions in the vortex streets are depicted in Fig. 4.6. The patterns of vorticity observed in our simulations are similar to those observed previously by other authors in numerical simulations of the flow behind a circular cylinder (e.g. Inoue and Yamazaki, 1999) as well as in the laboratory experiments performed in water (e.g. Karasudani and Funakoshi, 1994) or in soap films (Vorobieff et al., 2002). Returning to Fig. 4.2 we can observe that the flows for even higher values of J undergo further transition which can be identified by a rapid drop in frequency. After the drop the frequency follows a pattern of slow decay when J increases. Regular vortex street also forms in this regime (Fig. 4.6b), but the character of the vortex shedding becomes different. It is interesting to discuss here the onset of the secondary vortex street in the far wake. Taneda (1959) observed in his visualization experiments that vortex streets behind a cylinder break down at some distance from the cylinder, and that a new (secondary) vortex street consisting of vortices of larger scale forms far downstream. The formation of the secondary vortex street is believed to be due to the instability of the primary vortex street (e.g. Williamson and Prasad, 1993). The downstream position of the onset of the secondary wake was shown to be proportional to $Re^{-1/2}$ (Vorobieff et al., 2002). The formation of the secondary vortex street was also observed in our simulations. Typical

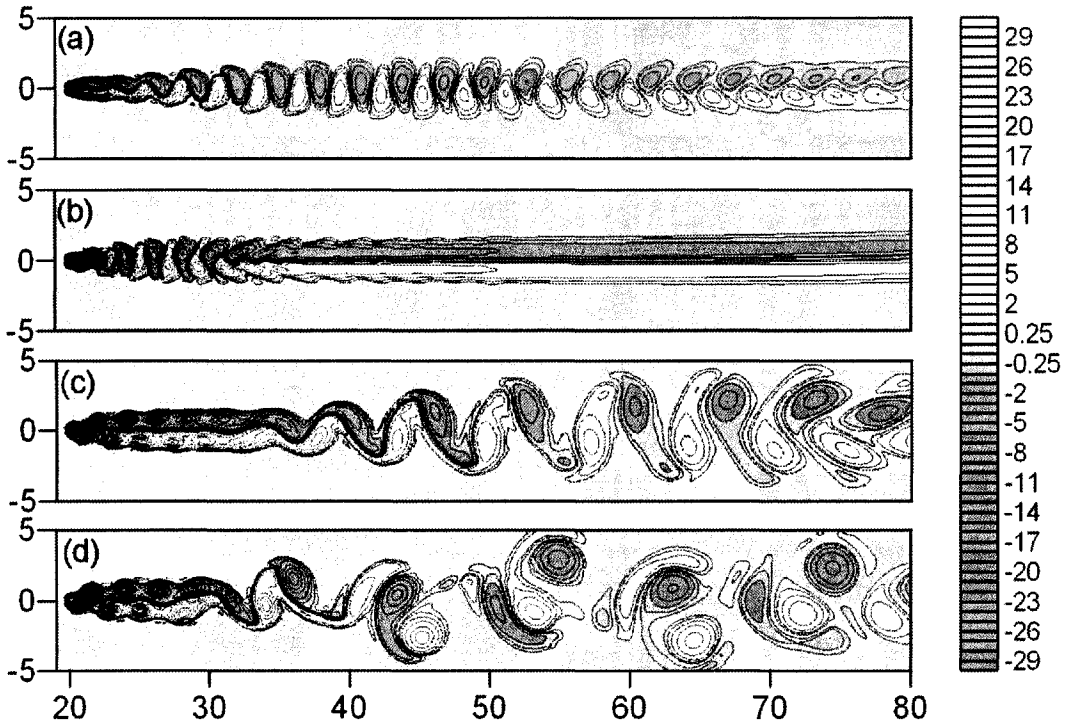

Figure 4.6: Vorticity contours for four different simulations. Panels (a) - (d) are for the same value of velocity U = 3.0 cm/s and different values of momentum flux J = 2.52 (a), 3.78 (b), 4.69 (c) and 5.67 cm^3s^{-2} (d). Color bar shows the values of vorticity in s^{-1}. Scale in cm.

example is shown in Fig. 4.6 c. Note that the wake in Fig. 4.6 b does not exhibit the secondary vortex street although the transition to almost parallel flow (which is a precursor to the development of the secondary vortex street in cylinder wakes) can be clearly seen in this picture. Since the Reynolds number for this flow was relatively low, the onset of the secondary vortex street was outside of the computational domain in this case.

Consider now the transition between stable wake and regular vortex shedding as well as the transition between two different vortex shedding regimes. The critical values of control parameters J and U at which the first and the second transitions occur can be measured from Figures 4.2 and 4.3. For the first transition the midpoints between the data points for zero frequency and the first non-zero value were taken to find either J or U while for the second transition the points in the middle of the interval where rapid drop of frequency occurs in Fig. 4.2 were chosen for this purpose. The values of J for the first and second transitions are plotted in Fig. 4.7 as a function of U^2. In these coordinates the behavior of the transition values of J is described accurately by linear relations of the form $J = 0.29\,U^2$ for the first transition and $J = 0.53\,U^2$ for the second transition. Note that the numerical coefficient for the first transition is approximately the same as that obtained in our simulations of the wakes behind a force doublet (virtual self-propelled body) which indicates that the dynamics of the transition is similar for these cases.

While the first transition is a regular transition from stable to unstable regime, the nature of the second transition is less clear. Let us consider a few simulations before and after the transition in more detail. The filled symbols in Fig. 4.8a labeled 1-4 indicate the particular runs chosen for this purpose. The plot of frequency as a function of J in Fig. 4.8a is the same as that in Fig. 4.2 for series 3. Figure 4.9 demonstrates the profiles of the x-component of velocity along the axis of the flow for

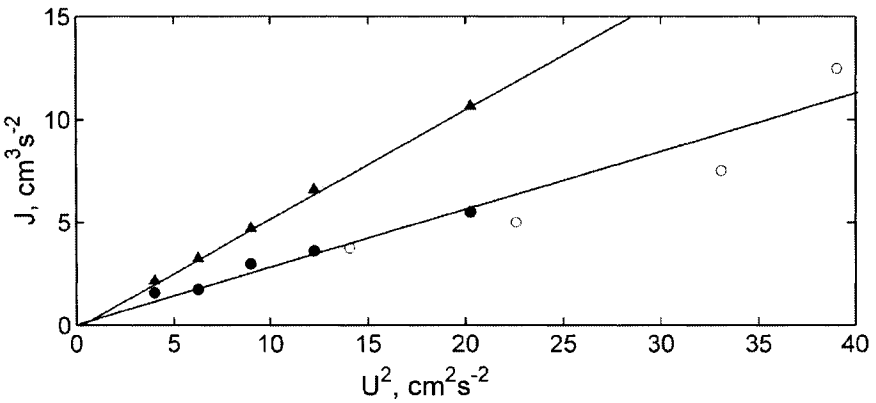

Figure 4.7: Values of J where transitions between the regimes occur for different U^2, measured from plots in Figs. 4.2 and 4.3. Filled triangles show the transition between the stable wakes and wakes with regular vortex shedding. Triangles and clear circles are obtained from Fig. 4.2 while filled circles are obtained from Fig. 4.3. Circles show the second transition between different regimes of shedding.

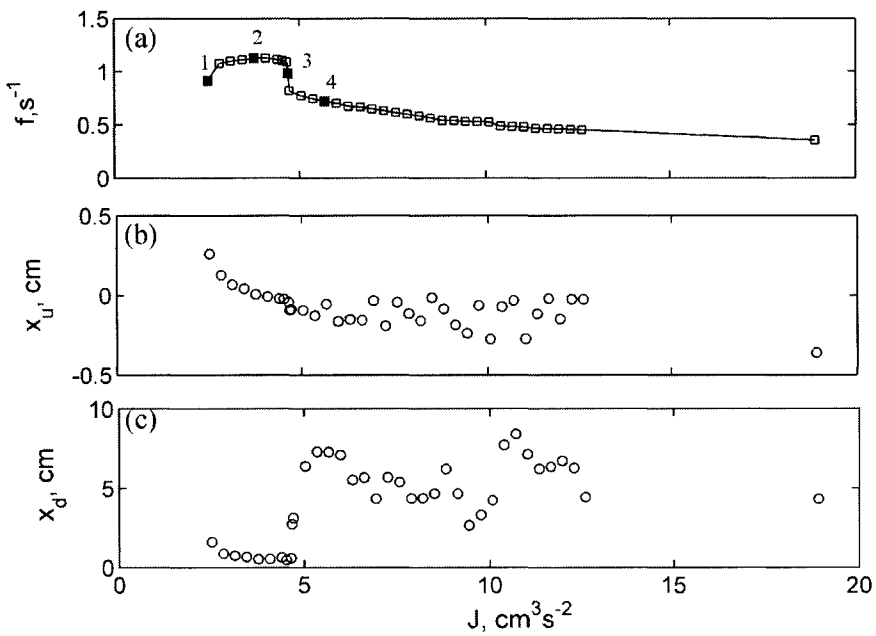

Figure 4.8: Frequency of vortex shedding (a), position of the upstream stagnation point (b) and position of the downstream stagnation point (c) plotted for different values of J measured in series 3 from the Table 1. Filled symbols in panel (a) indicate the simulations depicted in Fig. 4.6.

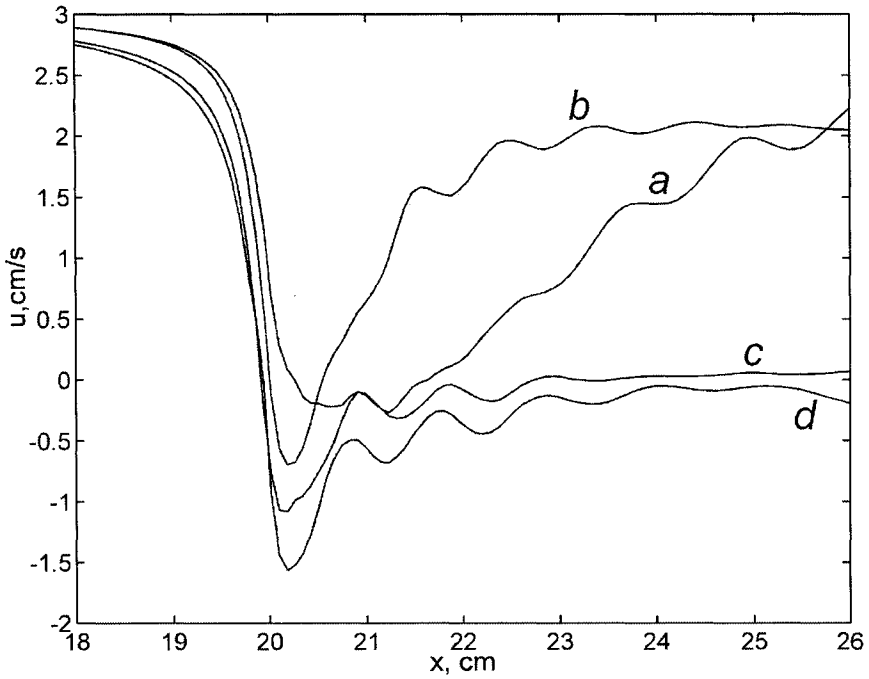

Figure 4.9: Distributions of the x-component of velocity along the axis of the flow (y = 0) for the same runs as in Fig. 4.6.

these four runs. An essential difference between the runs before the transition (a and b) and after the transition (c and d) is that for the runs before the transition (low J) the velocity downstream returns much faster (asymptotically) to its unperturbed value equal to the velocity of the stream U.

For high values of J, a long region with reduced velocity is formed downstream of the force. This feature of the flow can be further identified on the plots of the position of stagnation points located upstream and downstream of the force (Fig. 4.8). While the position of the upstream point (Fig. 4.8 b) varies smoothly with J, the position of the downstream point makes a jump to higher values after the transition (Fig. 4.8 c).

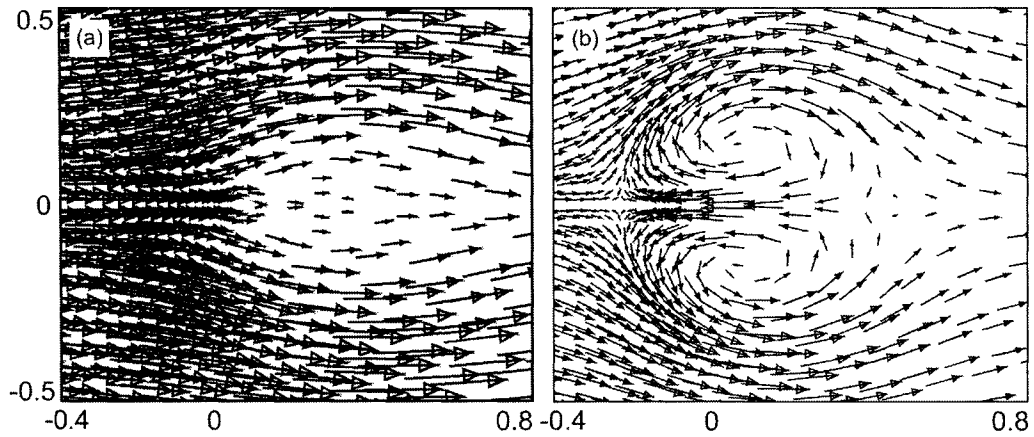

Figure 4.10: Velocity vectors in the vicinity of the origin at the after the start of the flow (t = 0.5 s) for two simulations with the same $J = 3.77cm^3/s^2$ but different stream velocities: U = 1.5 cm/s (a) and U = 3.0 cm/s (b).

Close inspection of velocity fields near the origin (Figs. 4.10 a, b) reveals that after the transition when the velocity of the stream is relatively low and the magnitude of the force is high, the forcing creates a region of recirculation (vortex dipole) near the origin such that the velocity at the x-axis within this region is in the opposite direction to that of the stream.

Before the transition, when the velocity of the stream is high and the magnitude of the force is low, the stream prevails and the forcing only creates a region with a depression in the magnitude of the velocity of the stream. Figures 4.11 - 4.13 depict different phases of vortex shedding for the runs 1, 2 and 4. The flow in Fig. 4.11 is almost parallel initially and only becomes unstable relatively far downstream. In the flow in Fig. 4.12 (again before the transition) the instability develops closer to the force. The vortex street can be characterized by a relatively small spacing between

the vortices in the y direction such that the vortices are located almost at the axis of the flow one after another. Finally, in the flow in Fig. 4.13 (after the transition), the vortex shedding occurs at the origin and the resulting vortex street is characterized by a significant spacing in y direction.

To better understand the results of the numerical simulations, it is useful to perform a simple dimensional analysis of the control parameters involved in the problem. Consider the frequency, f, of vortex shedding which depends on a set of four dimensional quantities namely, the kinematic viscosity ν, the velocity U, the amplitude of forcing J and the size of the region where the force is applied, a. Dimensional analysis then gives

$$f = \frac{U^3}{J}\Phi\left(\frac{J}{\nu U}, \frac{J}{aU^2}\right), \tag{4.1}$$

where Φ is an unknown function of two dimensionless arguments. The first argument $\Pi_\nu = \frac{J}{\nu U}$ of the function Φ includes viscosity and can be considered as an analogue of the Reynolds number of the flow. The second argument $\Pi_\alpha = \frac{J}{aU^2}$ includes a, and represents the effect of the finite size of the source. Π_α can also be interpreted as the ratio of the momentum flux delivered by the forcing to the momentum per unit time transported by the stream through the cross section of the forcing area. Relation 4.1 can then be rewritten in the dimensionless form as follows:

$$St = \Phi\left(\Pi_\nu, \Pi_\alpha\right), \tag{4.2}$$

where

$$St = \frac{fJ}{U^3}$$

is the Strouhal number (dimensionless frequency). Typical values of Reynolds number in our simulations are quite large, $\Pi_\nu \sim 10^2 - 10^3$, allowing us to consider the asymptotic behavior of function Φ for large values of its first argument. In the first approximation, one can assume complete similarity of this function with respect to

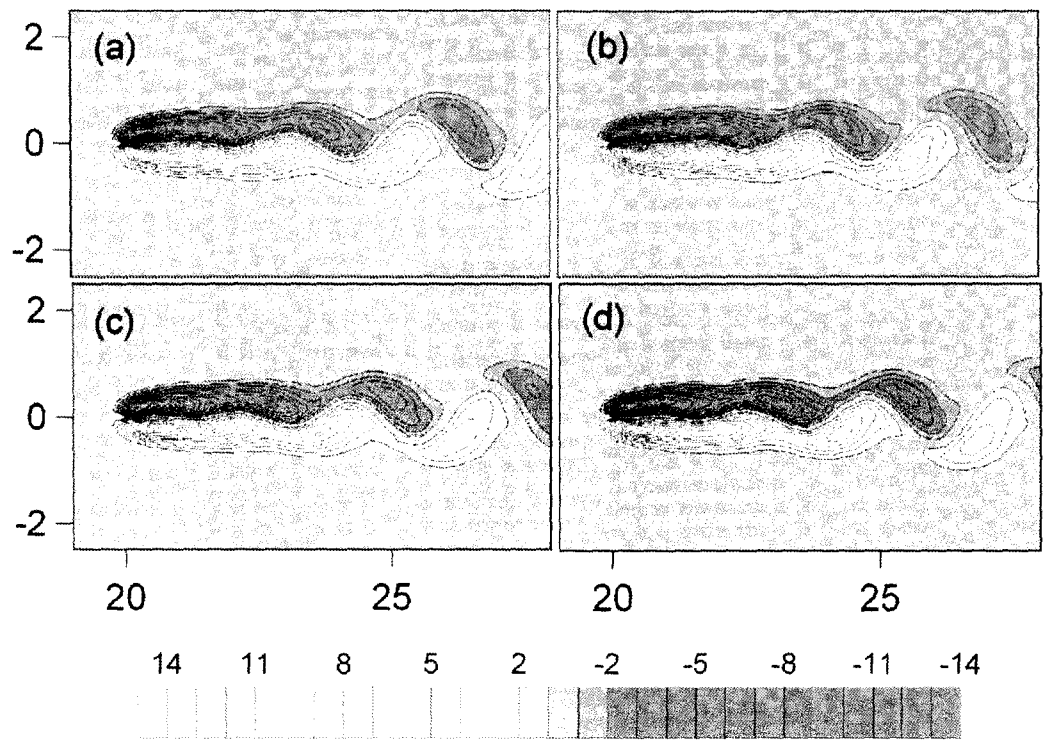

Figure 4.11: A succession of images showing the vorticity distribution in the vicinity of the force for different phases of the shedding cycle t = 474.35 (a), 474.65 (b), 474.95 (c) and 475.20 (d). Control parameters are J = 2.52 cm^3/s^2, U = 3 cm/s, a = 0.2 cm. Scale in cm. Color bar shows the values of vorticity in s^{-1}.

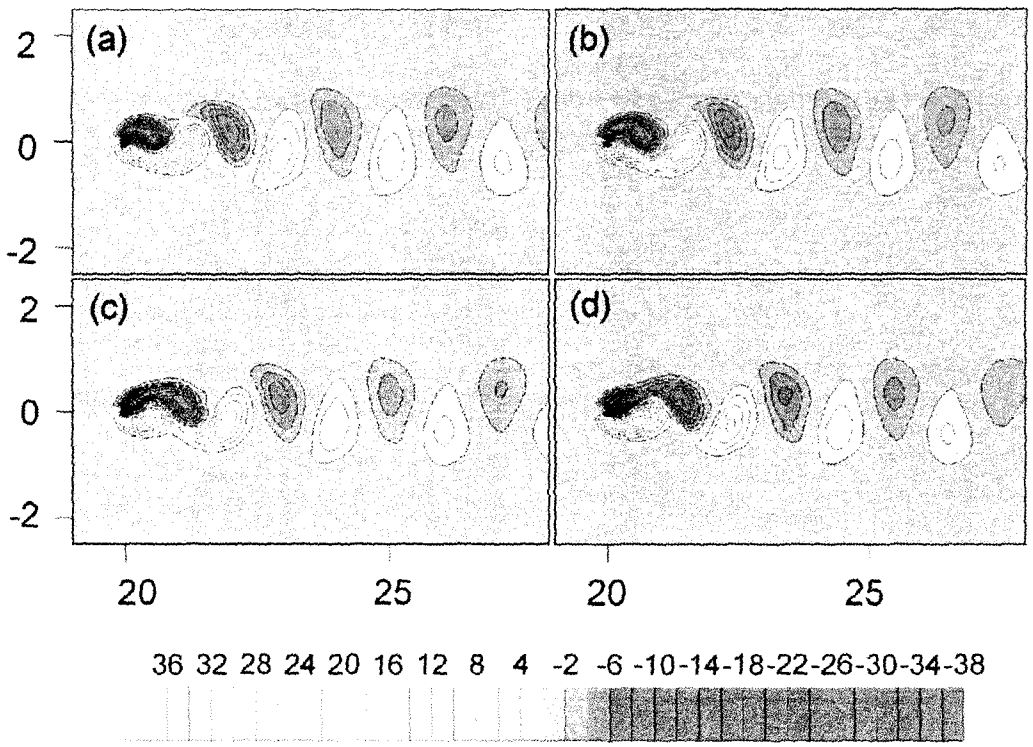

Figure 4.12: A succession of images showing the vorticity distribution in the vicinity of the force for different phases of the shedding cycle t = 179.35 (a), 179.55 (b), 179.85 (c) and 180.1 (d). Control parameters are J = 3.78 cm^3/s^2, U = 3 cm/s, a = 0.2 cm. Scale in cm. Color bar shows the values of vorticity in s^{-1}.

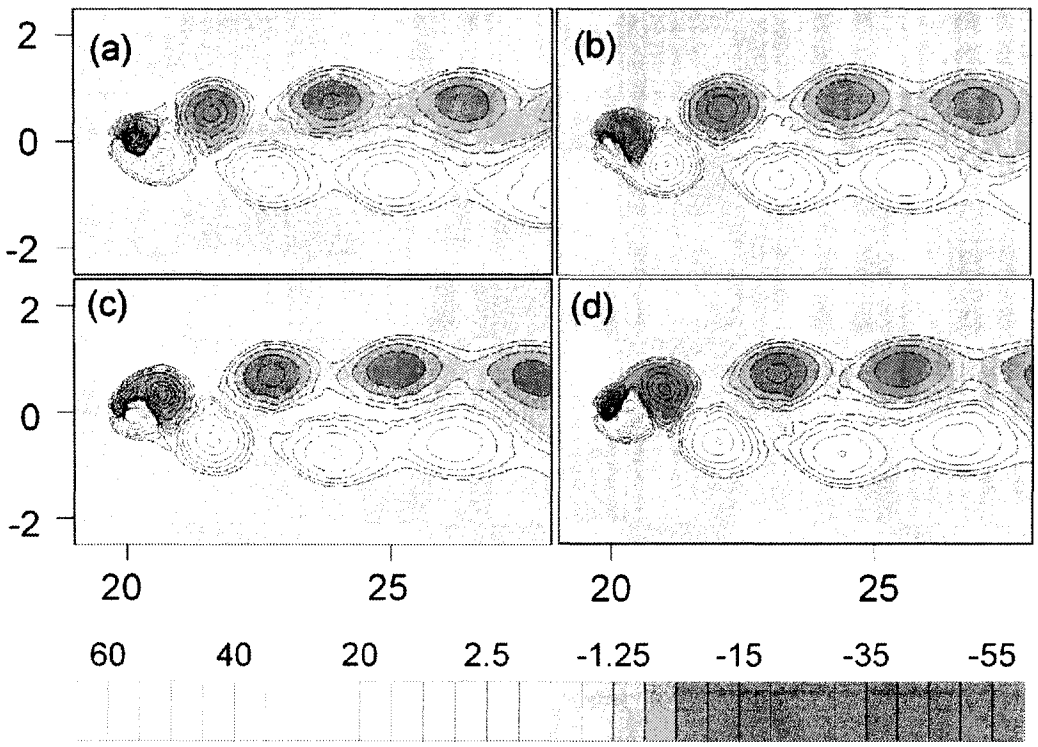

Figure 4.13: A succession of images showing the vorticity distribution in the vicinity of the force for different phases of the shedding cycle t = 70.1 (a), 70.45 (b), 70.8 (c) and 71.1 (d). Control parameters are J = 5.67 cm^3/s^2, U = 3 cm/s, a = 0.2 cm. Scale in cm. Color bar shows the values of vorticity in s^{-1}.

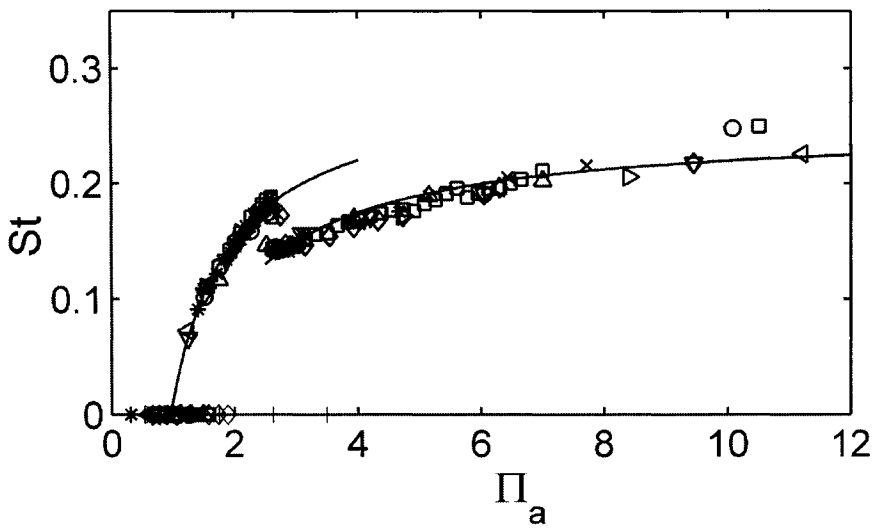

Figure 4.14: Strouhal number versus Π_α the dimensionless parameter for all series of simulations. A legend for symbols is given in Table 4.1.

Re, such that:

$$\Phi\left(\Pi_\nu \rightarrow \infty, \Pi_\alpha\right) = G(\Pi_\alpha), \tag{4.3}$$

where G is an unknown dimensionless function of one argument. To test the assumption of complete similarity, we plot the data from all of the experiments in a single graph St vs. Π_α (Fig. 4.14). The data collapse well on a single curve and the transition point is at approximately $\Pi_\alpha = 2.55$ which supports our original assumption. We can describe the function G using an analogue of the Roshko (1952) relation as follows:

$$\begin{aligned} G &= 0.29\left(1 - \frac{0.96}{\Pi_\alpha}\right) \qquad for \quad \Pi_\alpha < 2.65, \\ G &= 0.25\left(1 - \frac{1.25}{\Pi_\alpha}\right) \qquad for \quad \Pi_\alpha > 2.65, \end{aligned} \tag{4.4}$$

In terms of the dimensionless argument Π_α the first and second transitions between

the regimes occur at approximately $\Pi_\alpha = 1.5$ and 2.7. Note that the plot in Fig. 4.14 demonstrates a hysteretic behavior near both transition points. This is consistent with the description of the bifurcation points using the Stuart-Landau model (e.g. Dusek et al., 1994; Thompson, Le Gal, 2004; Williamson, 1996) It is interesting to relate the dimensionless parameters introduced here to those for the flows around a circular cylinder. The flow around a circular cylinder is controlled by three dimensional parameters: the diameter of the cylinder d, the velocity of the stream U and the kinematic viscosity of fluid ν. The force applied by the cylinder on the fluid is not an independent parameter but rather depends on the control parameters of the flow:

$$J = \frac{1}{2} C_D d U^2. \tag{4.5}$$

Here C_D is the drag coefficient, which depends on the Reynolds number of the flow. To establish the relation between these two problems we can use equation 4.5 to relate our dimensionless parameters to those in the problem with the cylinder as follows:

$$St = \frac{1}{2} C_D \frac{fd}{U} = \frac{1}{2} C_D St_c, \tag{4.6}$$

$$\Pi_\alpha = \frac{1}{2} C_D \frac{d}{a}, \tag{4.7}$$

$$\Pi_\nu = \frac{1}{2} C_D \frac{dU}{\nu}, \tag{4.8}$$

Here we introduced the Strouhal number, St_c, and the Reynolds number, Re, for the flow around the cylinder. Relation 4.8 gives typical values of the Reynolds number Re = 100 - 1000 for our simulations. Since the drag coefficient involves a dependence on Re which is generally unknown (although an empirical relation can be used, e.g. Chaplin, 1999), the relation between these two groups of dimensionless parameters is not straightforward. The relation between the flows around a cylinder and those induced by a localized force deserves further investigation and will be reported elsewhere.

4.2.2 Discussion and concluding remarks

In summary, it can be concluded that the results of the numerical simulations reported in this article provide a detailed description of the behavior of the Strouhal number for different values of control parameters which include the magnitude of the forcing and the velocity of the stream. Two distinct regimes of vortex shedding were observed in our simulations. The transition between regimes is in the form of a rapid drop in frequency. The flow in the first (high frequency) regime when the velocity of the stream is high and the magnitude of the force is low, is characterized by a depression in the magnitude of the velocity of the stream in the vicinity of the source. This effect is due to the finite size of the forcing region in the numerical simulations. In contrast the flow in the second (reduced frequency) regime when the forcing is relatively strong, is characterized by the formation of a recirculation region in the form of a vortex dipole such that the downstream stagnation point is located relatively far from the origin. Certain similarities in the behavior of the Strouhal number as a function of the dimensionless argument with the St versus Re dependence for a circular cylinder can be observed although the direct comparison is not straightforward due to the fact that the drag coefficient for the cylinder is a function of the Reynolds number. According to Fig. 4.14 the asymptotic value of the Strouhal number for large Π_α is approximately $St \approx 0.24$. This value is close to the asymptotic value of $St_c = 0.212$ (Roshko, 1952) for the flow around a cylinder for large values of the Reynolds number. It is interesting to mention here that similar behavior of the Strouhal number was observed in the laboratory experiments (Afanasyev, Filippov, 1995) where the flow around a cylinder oscillating in the transverse direction was studied. In those experiments the cylinder was thin enough that the Reynolds number (based on the size of the cylinder) was less then a critical. Therefore, there was no vortex shedding if the cylinder was stationary in the stream. However, if the cylinder oscillated rapidly, the typical

Karman - Benard vortex street was formed. The frequency of the vortex shedding was incomparable with the frequency of oscillations in that particular problem. The main control parameters were the velocity of the stream, U, the kinematic viscosity, ν, and the magnitude of the force doublet, Q, defined as $Q = F\varepsilon$, where F is the amplitude of the (oscillating) force in the transverse direction and ε is the amplitude of oscillations. The Strouhal number and the Reynolds number were then defined as follows:

$$St = \frac{fQ^{1/2}}{U^2}, \quad Re = \frac{Q}{\nu^2}.$$

Although these parameters were defined differently from those in the present problem, the result was similar. The Strouhal number was approximately constant for different values of the Reynolds number with the a value of $St \approx 0.23$.

4.3 Laboratory experiments

4.3.1 Experimental technique

The laboratory experiments reported here were conducted in a long rectangular tank: 120 cm long, 10 cm deep and 30 cm wide (Figure 4.15).

The tank was filled with two layers of salt water of height 0.5 cm each and of concentration 40 and 250 g/l. The flow was forced electromagnetically by imposing an electric current of magnitude j = 0 - 6 A in the horizontal direction. One or two rare earth permanent magnets of diameter 0.5 cm were located approximately 0.1 cm above the surface of water. The magnets were translated along the tank by a carriage driven by a computer controlled stepping motor on a translating stage. The translation velocity was varied in the range $U = 0.5 - 2\,cm/s$. Each magnet produces a magnetic field with a vertical component of approximately 0.09 T. The

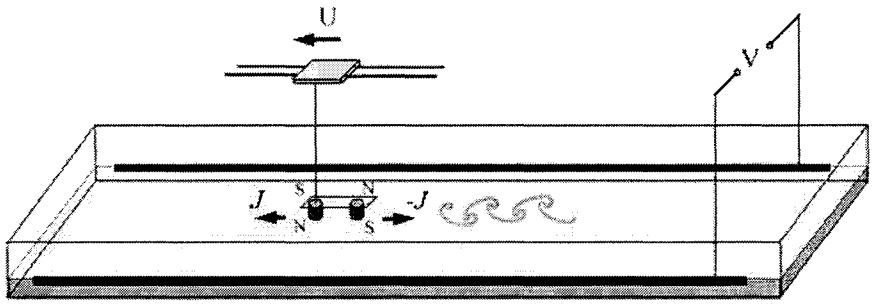

Figure 4.15: View of the experimental setup.

interaction of the magnetic field with the electric current results in a horizontal force exerted locally on the fluid in the direction perpendicular to the electric current. The magnitude of the force can be controlled in the experiments by varying the current. If a magnet is stationary, the localized force generates a starting vortex dipole. Our previous results (Afanasyev & Korabel 2004) which predict that the distance traveled by a dipole varies with time as

$$L(t) = \left(\frac{3J}{4\pi}\right)^3 t^{2/3}, \tag{4.9}$$

allow us to relate the momentum per unit time per unit depth of the layer, J , to the magnitude of the electric current j. We measured L using video sequences documenting the development of dipoles for different values of current j. The momentum flux J was then estimated from 4.9. The linear relation between the control parameter J and the current j was found to have the form $J = 0.54j$ where J is in cm^3/s^2 and j is in A. Here we assumed that the flow is approximately uniform in the vertical direction along the depth of the layer (except may be in the thin boundary layer at the bottom). In the experiments with a single magnet, the polarity of the magnet and the direction of the current were chosen such that the resulting force was applied on the fluid in the same direction as that of the translation of the magnet. This imitates

Series	♯ exps .	J, cm^3/s^2	U, cm/s	symbol
1	9	0.22-1.6	0.58	plus
2	10	0.27-1.6	0.87	diamond
3	5	0.54-1.6	1.16	star
4	8	0.54-1.6	1.45	square
5	5	0.8-1.6	1.74	circle

Table 4.2: Experimental parameters for the experiments with a single magnet.

the force applied by a towed body on the fluid (a reaction to the drag force).

The flow was visualized by pH-indicator thymol blue and recorded using a video camera or a photo camera placed above the container. Geometrical characteristics of the flow were then measured using the individual frames of a video sequence. The horizontal velocity field in the flow was measured using a PIV technique. A description of the method and general technique is given by Fincham & Spedding (1997). Videos of the experiments were recorded in plan view using a digital video camera with an array resolution of 1032 x 1032 pixels. The typical spatial resolution of the images was 35.5 pixels/cm. The seeding particles were polyamid spheres of mean diameter 50 nm which were made visible by illuminating the fluid with a sheet of light from a laser at the interface between the layers. Parameters of the experiments with the single and double forces are summarized in Tables 4.2.

Experimental results and interpretation

In order to identify different regimes of the flow a number of experiments were performed where the main control parameters, namely the translation speed of the mag-

net U and the momentum flux J , have been varied. Figure 4.16 demonstrates typical images of the flow in the experiments with a single force. When the speed of the magnet was relatively large while the force was relatively weak, the wake behind the magnet was stable and was in the form of a jet (not shown in Fig. 4.16) flowing in the direction of motion of the forcing. For higher values of J (or lower U) undulations of the jet were observed (Figure 4.16 a). In some experiments these undulations develop into a vortex street consisting of antisymmetric array of vortices (interconnected vortex dipoles) well after the forcing is passed (Figure 4.16 b). It will be shown later, however, that the initial form of the instability of the jet flow is in fact symmetric in the form of a chain of dipoles moving after one another along the jet axis. When we further increased J a clear transition to a different regime of the instability was observed. The forcing is now strong enough to generate a compact vortex dipole under the magnet. This dipole does not remain stable however and start shedding vortices. While the dipole loses vorticity of one sign it becomes asymmetric and eventually turns in the direction of rotation of the remaining vortex. Thus the periodic shedding of vortices is accompanied by the wobbling of the dipole (Figure 4.17). This results in a formation of a typical Karman-Benard vortex street in the wake (Figure 4.16 c). When the forcing is increased even further the nonlinearity of the flow increases to such an extent that the forcing produces strong compact vortex dipoles which then eject in different directions quasiperiodically without forming an organized vortex street (Figure 4.16 d). Further insight into the dynamics of the unstable wakes can be provided by PIV measurements. Figure 4.18 demonstrates the velocity and vorticity fields for three different regimes of the flow. A stable jet is shown in plate a of figure 4.18 while plate b shows a typical form of instability of the jet. This particular regime of instability corresponds to that shown in figure 4.18a. The unstable flow is symmetric with respect to the axis of the jet and is in the form of dipoles where

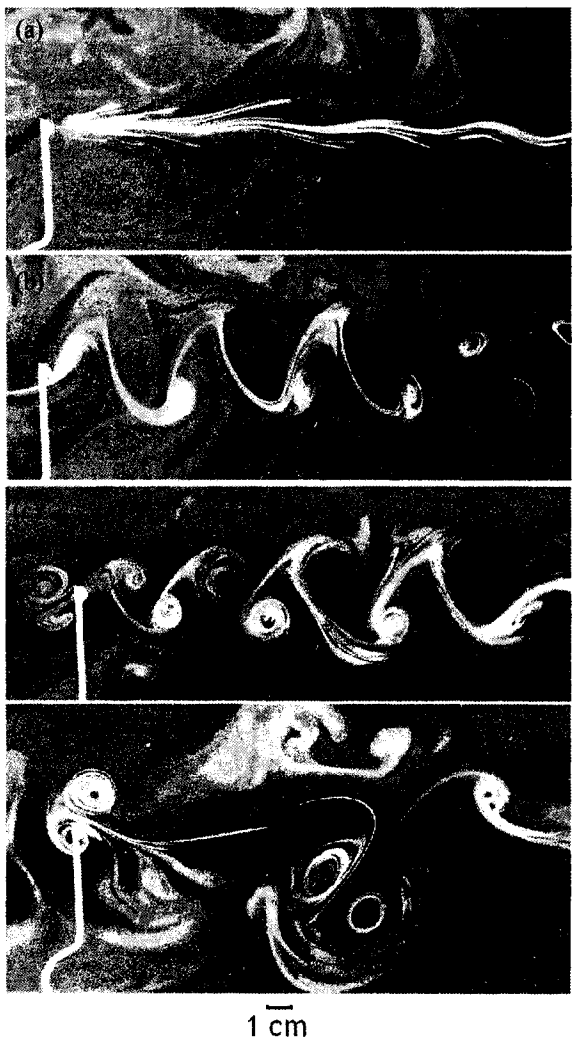

Figure 4.16: Images of the flow generated by a single magnet for different regimes. Top view. The magnet is located at the end of the support rod. Experimental parameters: U = 0.87 cm/s, J = 0.48 cm^3/s^2 (a); U = 1.74 cm/s, J = 1.6 cm^3/s^2 (b); U = 1.16 cm/s, J = 1.1 cm^3/s^2 (c) and U = 0.87 cm/s, J = 1.35 cm^3/s^2 (d).

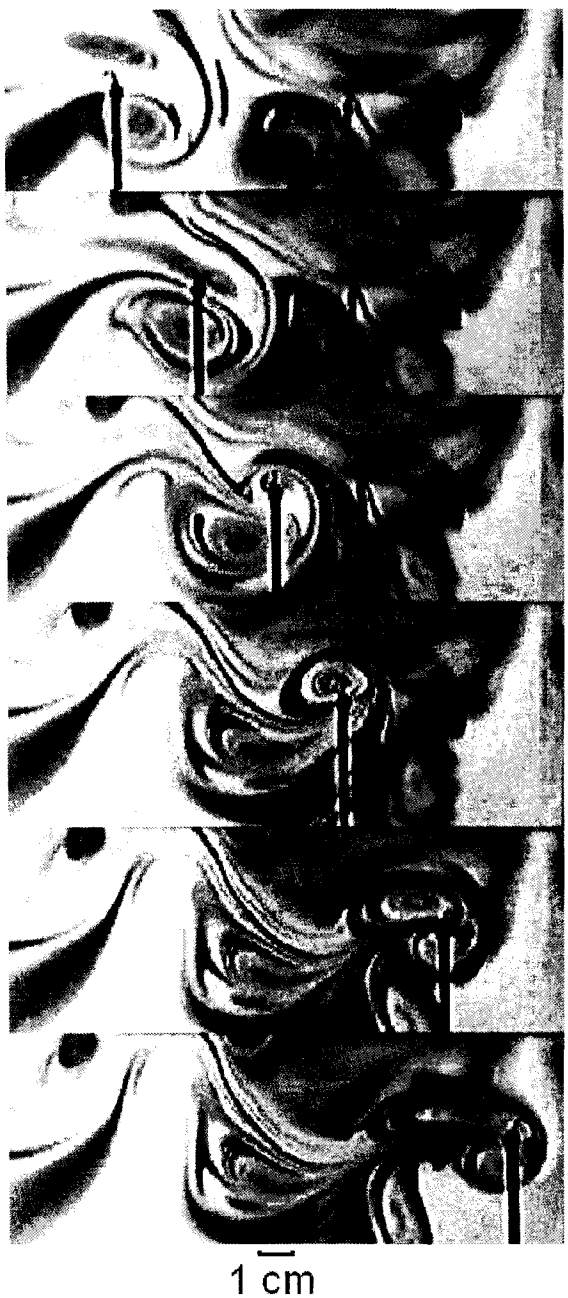

Figure 4.17: Sequence of video frames showing the vortex shedding by the unstable dipole.

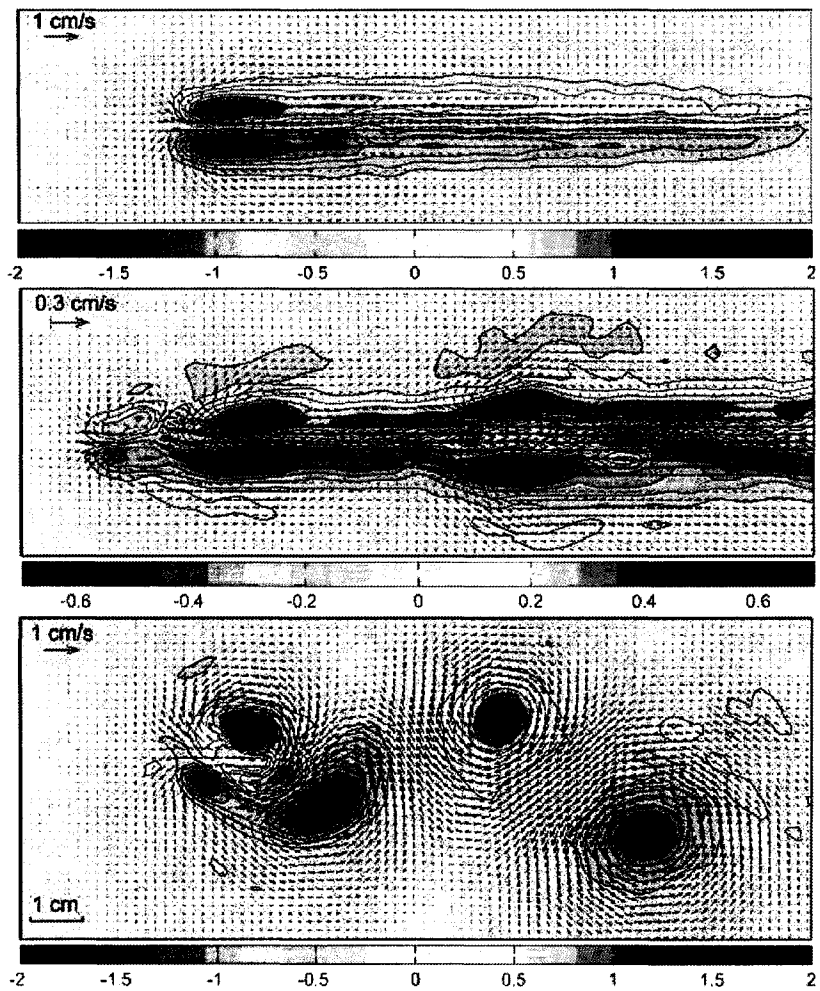

Figure 4.18: Vorticity (color) and velocity (arrows) fields measured in the experiments with a single magnet for different regimes of the flow: U = 1.45 cm/s, J = 0.54 cm^3/s^2 (a); U = 1.6 cm/s, J = 1.1 cm^3/s^2 (b) and U = 0.58 cm/s, J = 0.54 cm^3/s^2 (c). The color bars show the vorticity scale in s^{-1}.

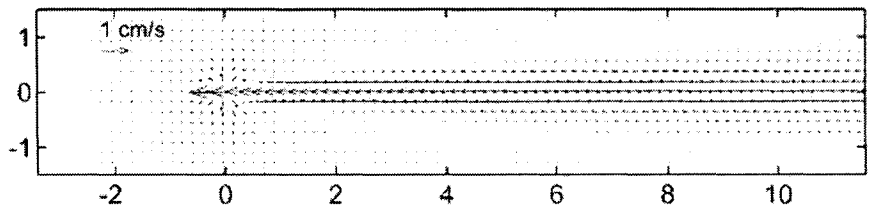

Figure 4.19: Velocity field for the flow induced by a moving point force calculated from the theoretical solution 2.22. Scale in cm.

the vorticity of the jet is concentrated. The dipoles propagate in the same direction as that of the jet. Finally, the regime of the Karman-Benard vortex street where an antisymmetric array of vortices is shed from the vortex dipole is shown in figure 4.18 c. The measurements of the velocity field in the stable jet (figure 4.18 a) allows us to perform a comparison with theoretical results. The x and y velocity components, can be obtained by differentiation of the stream function of the flow 2.22, 2.23 obtained in Chapter 2. The velocity vectors are shown in figure 4.19 which can be compared with the velocity field in figure 4.18 a. The values of control parameters J and U are the same for theory and the experiment. Comparison shows some similarities as well as the differences. In order to compare these data in a quantitative manner we plotted the profiles of x-component of velocity, u, for three different distances from the origin (where the forcing is located).

The experimental data (symbols) and theory (solid lines) in figure 4.20 demonstrate that the width of the jet remains approximately constant in the experiments while according to theory it must increase with the distance from the origin. The most important discrepancy between the theory and the experiment is the significant

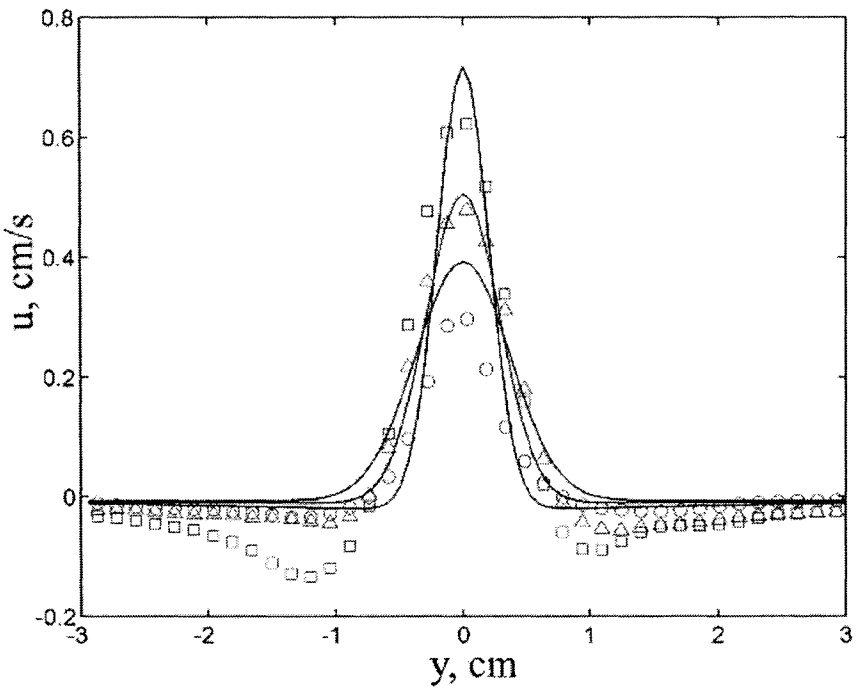

Figure 4.20: Profiles of the x-component of velocity in the jet at three different distances (x = 3, 6 and 10 cm) from the origin where the forcing is located. Solid lines represent the theoretical solution 2.22 while symbols show the results of the PIV measurements (same as in figure 4.19 a).

return flow at the sides of the jet which is observed in the experiment. The return flow predicted by theory is very weak. The origin of this discrepancy lies in the finite size of the forcing area. While theory is developed in the assumption of a point force, the effect of the size of the forcing area, a is in fact significant both for the dynamics of the stable jet and for the instability of the flow. Our previous numerical simulations (Afanasyev & Korabel 2004) of vortex dipoles generated by a localized forcing in initially quiescent fluid demonstrated that when a was small enough the comparison of results of numerical simulations with theory was quite good. The flow did not form concentrated vortices in that case. In contrast, for larger a, the compact vortex dipole was formed at the front of the developing jet. The dipole propagated faster than predicted by theory because the theory neglected the effect of self-induction of vortices. This dipole also remained a compact structure during its evolution. The effect of the finite size of the forcing area (or rather the effect of the corresponding dimensionless parameter which includes a) will also be discussed here in the context of the dynamics of the vortex shedding for unstable flows. The wavelength of the perturbations, was measured in our experiments for different regimes of the flow. The wavelength was defined as a distance between the peaks in the meandering jet such as the one in figure 4.16 a or the distance between the vortices of the same sign in the vortex street (figure 4.16 c). The frequency of the perturbations can then be introduced as $f = U/\lambda$. Dimensional analysis preformed in Section 4.2 suggests that frequency f depends on the set of four dimensional quantities including kinematic viscosity ν, velocity U, the amplitude of forcing J and the size of the region where the force is applied, a. It can be related to these parameters in a form of dimensionless as follows:

$$St = \Phi\left(\Pi_\nu, \Pi_\alpha\right),$$

where $St = fJ/U^3$ is the Strouhal number (dimensionless frequency). The Strouhal

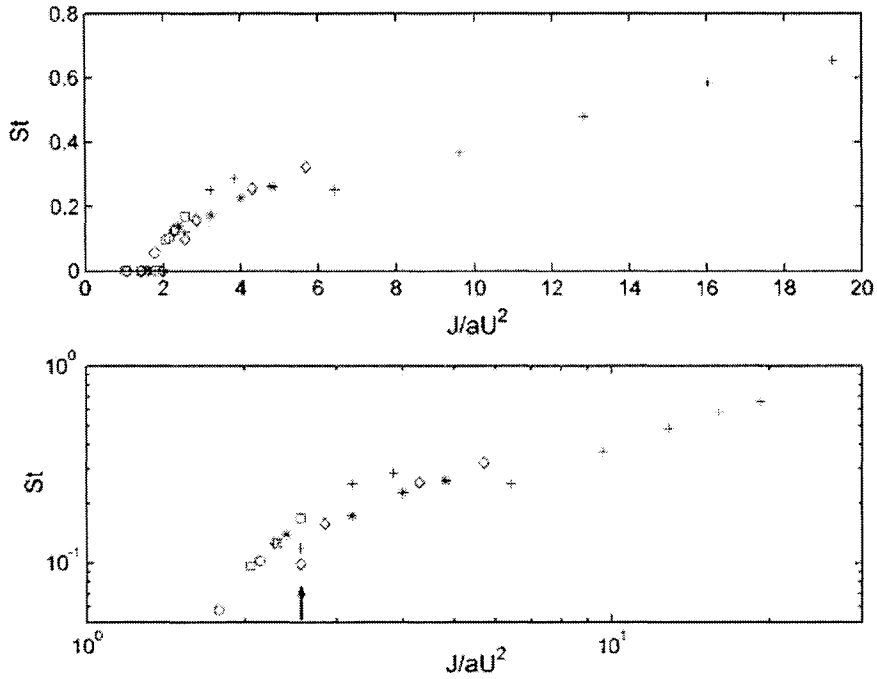

Figure 4.21: The Strouhal number versus Π_α for five series of experiments with a single magnet in linear and logarithmic scale. The legend for symbols is given in Table 4.2.

number is plotted in figure 4.21 as a function of Π_α for five series of experiments.

In each series the value of velocity U was fixed while the magnitude of the forcing J was varied (Table 4.2). The graph shows that transition between the regimes of the stable jet ($f = 0$) and unstable meandering jet occurs at $\Pi_\alpha \approx 2$. The second transition from the meandering jet to the Karman-Benard vortex streets is not immediately obvious from the data but it can be identified from the analysis of the images of the flow. The analysis gives that the transition occurs at $\Pi_\alpha \approx 2.5$.

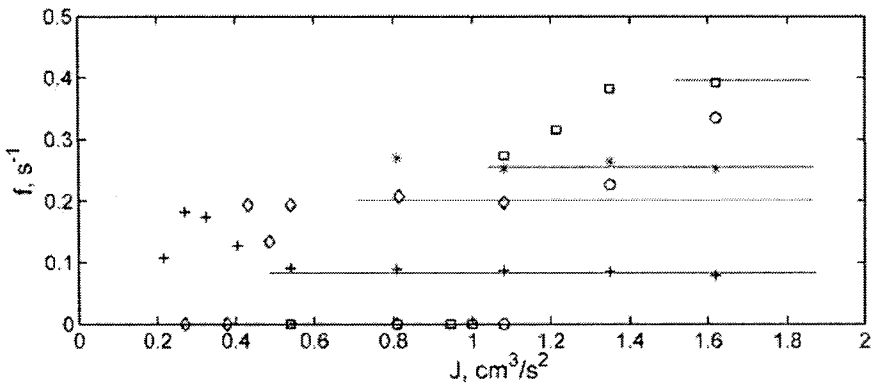

Figure 4.22: Frequency of vortex shedding for different values of the forcing magnitude. Solid lines indicate schematically asymptotic values of frequency for large J in the experiments with different U. Symbols are the same as those in figure 4.21.

A second look at the data allows one to see a small step in the graph (marked by arrow in figure 4.21) at this value of Π_α . The data points in the St versus Π_α graph corresponds to different values of Π_ν . However, the data collapse well on a single curve for $\Pi_\alpha < 2.5$ that indicates negligible dependence of the function $St = \Phi(\Pi_\nu, \Pi_\alpha)$ on its first argument. The data points in this range of are characterized by the relatively large values of velocity. The scatter in the data for the larger values of Π_α however is more significant implying that the dependence on Π_ν has to be taken into account. To clarify this dependence, let us return to the dimensional variables. A plot of frequency as a function of J for the series of experiments with different velocity U (figure 4.22) demonstrates that the frequency remains approximately constant with J when the flow is in the vortex street regime (J is sufficiently large).

The asymptotic values of f for four series of experiments (different U) is indicated by the straight line in figure 4.23. For the fifth series (circles) which correspond to the

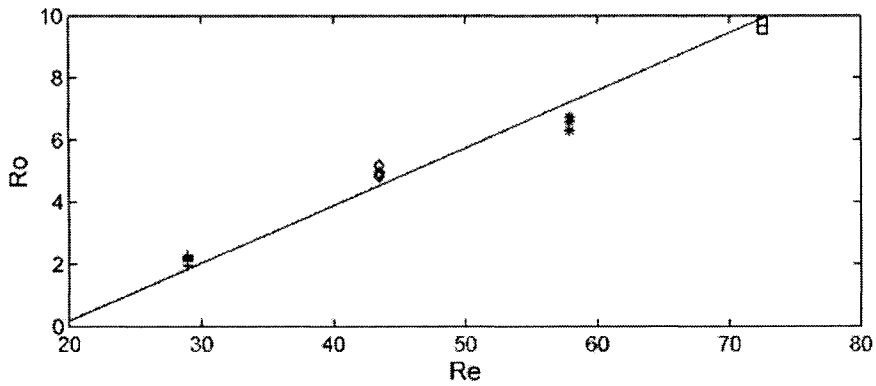

Figure 4.23: The Roshko number versus the Reynolds number for the flows where the Karman-Benard vortex street was formed.

largest U, the forcing was not strong enough for the flow to reach the vortex street regime. The constant values of f can be plotted then as a function of U. However, this can be done also in terms of new dimensionless parameters, namely the Roshko number and the Reynolds number defined as follows:

$$Ro = \frac{fd^2}{\nu},$$

$$Re = \frac{Ud}{\nu}.$$

Here $d = 2a$ is the diameter of the forcing region. These numbers are used to describe the flow around a circular cylinder which is one of the well studied flows in fluid mechanics (e. g. Zdravkovich 1997). We can therefore establish a similarity between the flow generated by localized forcing and the flow around the cylinder. The plot of Ro versus Re where only the data points for the flow in the established vortex street regime are considered, is shown in figure 4.24.

A linear fit gives the dependence of the form

$$Ro = 0.18(Re - 0.18), \tag{4.10}$$

This dependence is very close to that of the flow around a cylinder. A number of such dependences have been offered in literature during a period of more than 100 years. The well known examples include:

$$Ro = 0.195(Re - 20.1), \quad (Rayleigh\,1879), \tag{4.11}$$

$$Ro = 0.212(Re - 21.2), \quad (Roshko\,1952), \tag{4.12}$$

$$Ro = 0.21(Re - 20.5), \quad (Tritton\,1959). \tag{4.13}$$

Note, that in 4.10 the value of the size of the forcing region is not known exactly and the diameter of the magnet is taken as an estimate. This can account for the small discrepancy between the numerical values of coefficients in 4.10 and those in the relations for the cylinder. Thus, the dynamics of the flow in the regime when the Karman-Benard vortex street forms in the wake is similar to that of the flow around a cylinder for moderate values of the Reynolds number ($40 < Re < 150$).

Chapter 5

Momentumless wakes and vortex streets generated by a force doublet

5.1 Numerical simulations of a virtual self-propelled body

5.1.1 Introduction

Self-propelled bodies in a wide range of scales from microorganisms to submarines, generate wakes which are characterized by (approximately) zero momentum when they move with constant speed without maneuvering. The drag and thrust forces applied on the self-propelled body are of equal magnitude and of opposite directions.

The drag force is applied near the front of the body while the thrust force is usually generated near the rear end. Thus, these forces are separated by a distance which is approximately equal to the length of the body. The same is also valid for the corresponding reaction forces which are applied by the body on the fluid. Herein, we formulate an idealized problem where the effect of the moving body is effectively reduced to a combination of two spatially localized forces acting on the fluid. Since momentum is a conserved quantity, the major control parameter in the problem is the total magnitude of the force or equivalently the momentum flux transferred to the fluid. The flow peculiarities due to details of the shape of the body or equivalently the details of the distribution of forcing are then controlled by higher moments of the force distribution and decay faster with distance from the origin. This approach is therefore justified if one is interested in the flow sufficiently far from the object. In what follows we consider a force doublet consisting of two forces of equal magnitude and opposite directions. These forces however cannot be considered as being point forces since the area where they are applied although small, is finite. The distance between the forces is also finite. Thus we do not perform the limiting procedure which requires the distance between the forces to be made small while simultaneously increasing the magnitude of the forces inversely proportional to the distance. Our previous numerical simulations of the drag wakes (generated by a single localized force) as well laboratory experiments with both a single force and a force doublet, demonstrated that the finite size of the area where the force is applied is an important factor in developing the instability of the wake in the form of a vortex street. Thus the considered flows are in fact a result of the interaction of two drag wakes (of equal and opposite momenta) with different origins. The characteristics of the drag wakes occurring behind towed bluff bodies are relatively well studied. In particular the flow around a cylinder which is a classical problem in fluid mechanics, has a long

history of serious investigation, see comprehensive reviews by Zdravkovitch (1997) and Williamson and Govardhan, (2004). The behavior of the frequency of vortex shedding which is usually presented in dimensionless form by either the Strouhal number or the Roshko number, is known for a wide range of the Reynolds number of the flow. Similar comprehensive analysis of the wakes behind the self-propelled bodies is yet to be performed. In the following sections of this thesis we report on the results of numerical simulations of the (stable or unstable) flows generated by two localized forces of equal magnitude and of opposite direction which are applied in a uniform stream. In this Chapter the details of the numerical simulations including the computational grid and boundary conditions are described. The dimensional analysis of the governing parameters is presented as well as description of different regimes of the flow observed in our simulations for different values of governing parameters is given. Velocity data in stable wakes are compared with the available theoretical results. The frequency of vortex shedding in unstable wakes is then analyzed in the space of dimensionless control parameters.

5.1.2 Numerical simulations of a virtual self-propelled body

Several series of two-dimensional numerical simulations that document the evolution of the flow generated by a force doublet applied in a uniform stream have been performed using the same numerical scheme as describes in Section 4. A force doublet was simulated by two forces of opposite sign and of equal magnitude, J. Each force was applied to the fluid in a circle of radius a = 0.2 cm such that the force density F (force per unit area) is described by the Gaussian distribution $F = F_0\, exp(-r^2/a^2)$. The first (upstream) force was located at x = 20 cm within the computational domain while the second (downstream force) was at x = 23 cm. The distance between the forces was fixed at $\delta = 3$ cm in all runs. The amplitude of the force, F_0 was varied in

our simulations. For the flows where the regular shedding of vortices was observed, we measured the frequency of shedding using the following method. The mean value vorticity was calculated for positive values of y along a line located perpendicular to the axis of the flow at x = 25 cm (2 cm downstream of the second force). The time series of the vorticity values was then analyzed using a Fourier transform to find the shedding frequency. For the investigation of the secondary vortex street in this section, the position of the test line was variable.

Control parameters

To analyze the results of the numerical simulations, it is useful to perform simple dimensional analysis of the control parameters involved in the problem. The frequency f of vortex shedding (as well as other characteristics of the wake) depends a set of four dimensional quantities including kinematic viscosity ν, velocity of the stream U, the amplitude of forcing J, the size of the region where the force is applied, a and the distance between the forces δ. Dimensional analysis then gives

$$\frac{fJ}{U^3} = \Phi\left(\frac{J}{\nu U}, \frac{J}{aU^2}, \frac{J}{\delta U^2}\right), \tag{5.1}$$

where Φ is an unknown function of three dimensionless arguments. Here we used J and U to nondimensionalize the rest of dimensional parameters. The first argument $\Pi_\nu = \frac{J}{\nu U}$ of the function Φ represents the effect of viscosity while the second argument $\Pi_\alpha = \frac{J}{aU^2}$ and the third argument $\Pi_\delta = \frac{J}{\delta U^2}$ represent the effect of the finite size of the forcing area. The dimensionless frequency $St_J = \frac{fJ}{U^3}$ is the analogue of the Strouhal number (in the conventional definition of the Strouhal number the typical size of the body, d is used as a length scale $St = fd/U$). In what follows we investigate the dimensionless function Φ over the wide range of their arguments using the results of our numerical simulations.

Series	♯ exps,	J, cm^3/s^2	U, cm/s	symbol
1	51	2.8 - 31.5	3	triangle (down)
2	29	5 - 30.2	3.5	triangle (up)
3	33	5.6 - 39	4.5	triangle (left)
4	32	8.82 - 44.1	5.5	triangle (right)
5	5	3.78	1 - 4.5	circle
6	8	5.04	1 - 4.5	hexagram
7	4	7.56	3 - 5.5	diamond
8	6	12.6	2.5 - 6	pentagram
9	27	37.8	3 - 11	square

Table 5.1: Numerical simulations for the force doublet.

Results of numerical simulations

Our simulations were performed in series where one of the control parameters was varied while others were fixed (Table 1).

Several distinct regimes of the flow were observed for different values of the control parameters. Figure 5.1 depicts vorticity fields which illustrate typical regimes of the flow. For low values of J (or relatively high values of U) the wake is stable. The vorticity distribution is in the form of layers of positive and negative vorticity (Fig. 1.4). Vorticity profiles in the stable wake for one of our numerical simulations together with those calculated from the theoretical relations 2.27 and 2.28 are presented in the Fig. 5.2. The profiles are given at two locations downstream of the forces at a distance of 15 and 25 cm from the upstream force. The Reynolds number for this

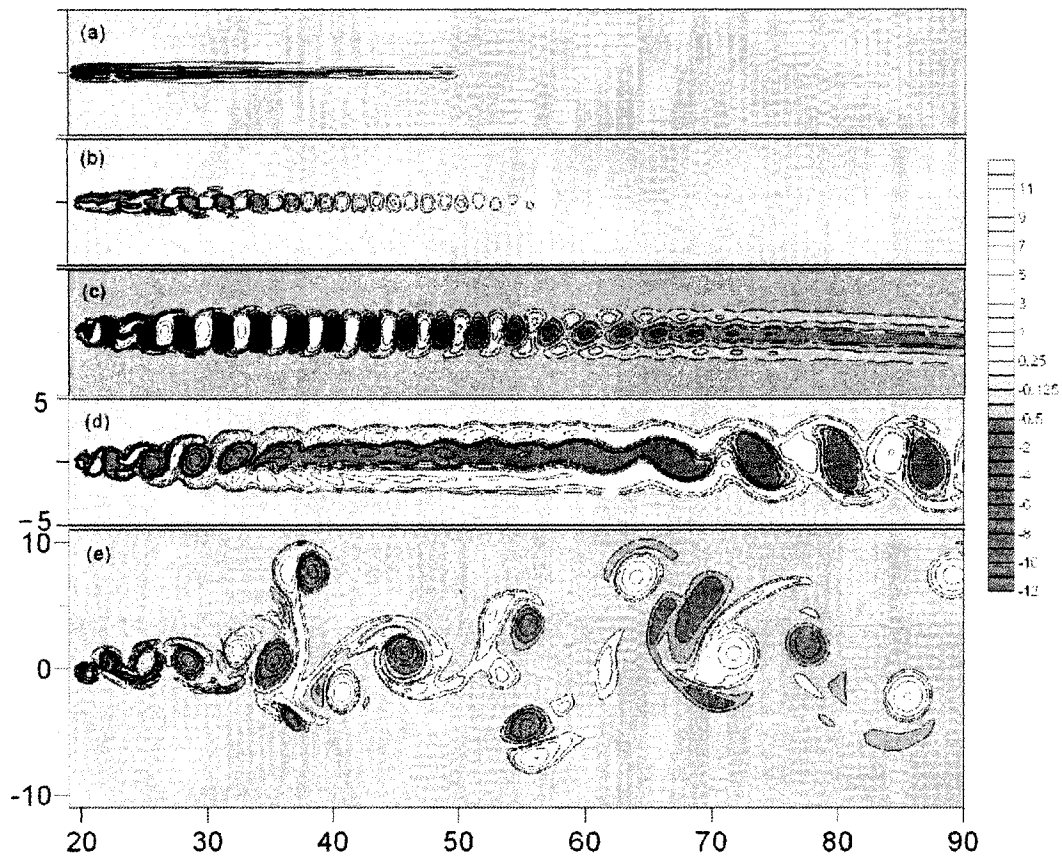

Figure 5.1: Vorticity contours for five different simulations. Panels (a) - (d) are for the same value of velocity U = 5.5 cm/s and different values of momentum flux J = 5.66 (a), 8.81 (b), 30.2 (c) and 41.5 cm^3s^{-2} (d). Panel (e) is for U = 3 cm/s and J = 28.95 cm^3s^{-2}. Color bar shows the values of vorticity in s^{-1}. Scale in cm.

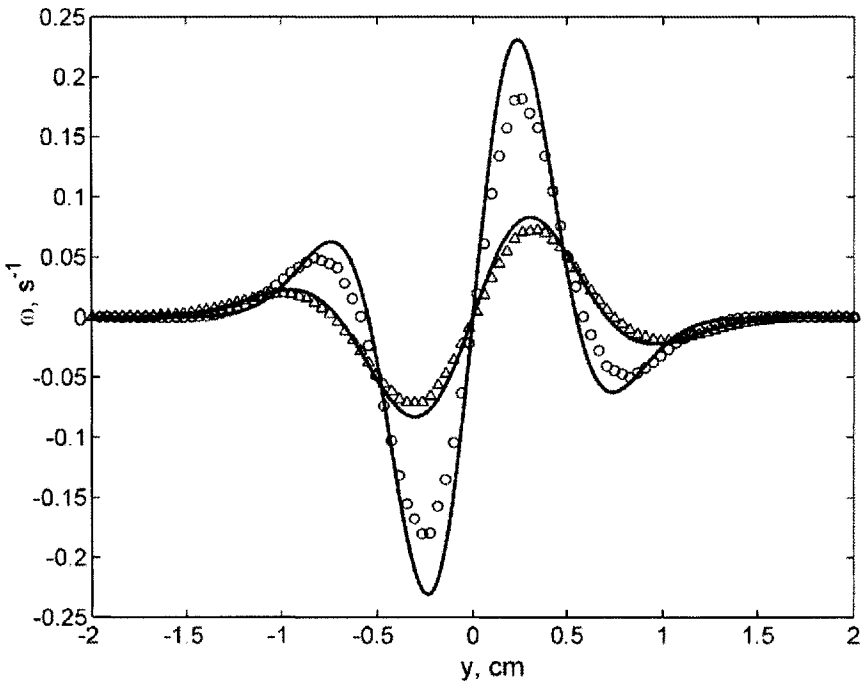

Figure 5.2: Vorticity profiles across the wake at two locations x = 15 (larger amplitude) and 25 cm (smaller amplitude) calculated in numerical simualtins (symbols) and from theoretical relation (2.29). Control parameters are the same as those in Fig. 2.4.

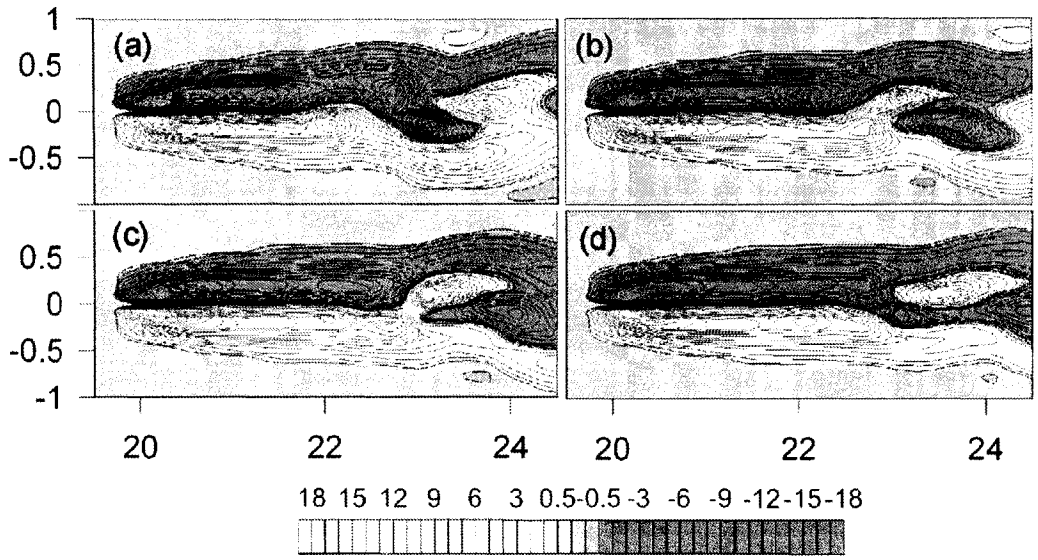

Figure 5.3: A succession of images showing the vorticity distribution in the vicinity of forces for different phases of the shedding cycle t = 147.9 (a), 148.1 (b), 148.25 (c) and 148.4 (d). Control parameters are the same as those for Fig. 5.1 b. Scale in cm. Color bar shows the values of vorticity in s^{-1}.

particular flow $Re = 2aU/\nu = 120$ is fairly high. The comparison reveals a closer agreement for larger distance as one might expect for the solution obtained in the Oseen approximation. For larger J, regular shedding of oppositely signed vortices occurs in the close vicinity of the forces. The vortices then form a regular vortex street downstream. Zoomed images of the area where forces are located are demonstrated in Fig. 5.3. Closer inspection reveals that in this regime the upstream force (located at $x = 20$ cm in Fig.5.1 b) is not strong enough to produce a recirculation region in the form of a vortex dipole. Rather this force creates a region of reduced velocity in the incoming stream. The wake behind this force is stable. In contrast, the flow induced by the downstream force (located at $x = 23$ cm) is unstable and regular shedding

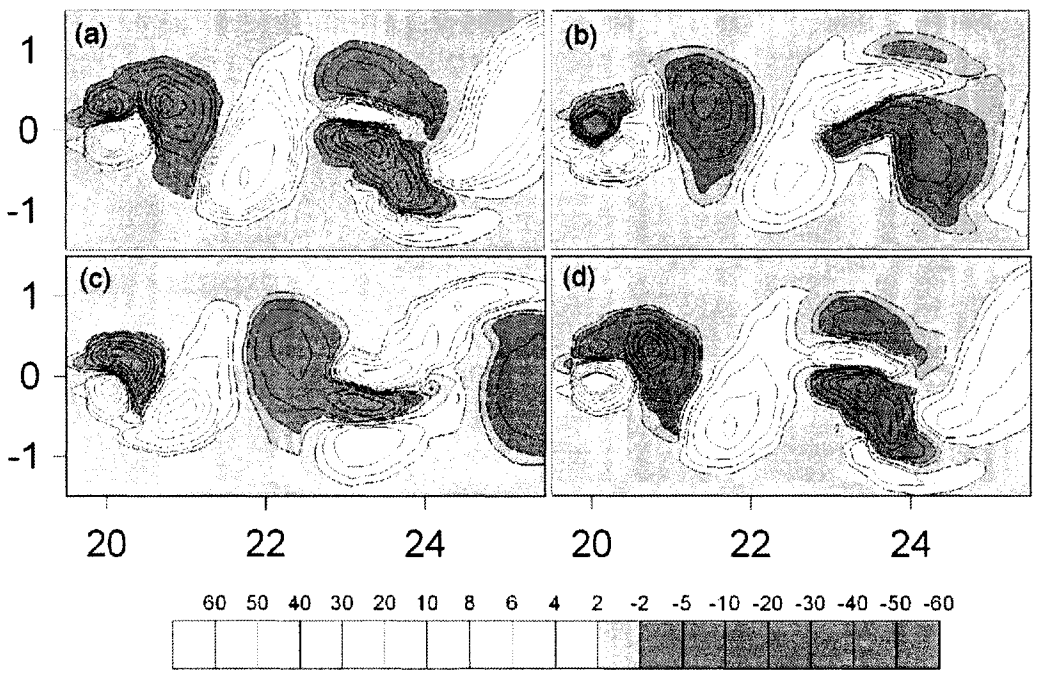

Figure 5.4: A succession of images showing the vorticity distribution in the vicinity of forces for different phases of the shedding cycle t = 66.3 (a), 66.5 (b), 66.75 (c) and 66.85 (d). Control parameters are the same as those for Fig. 5.1 d. Scale in cm. Color bar shows the values of vorticity in s^{-1}.

of vorticity occurs in the vicinity of the force. Different phases of shedding over one period are depicted in Fig. 5.3. The separated vortices create a regular vortex street along the axis of the flow while the layers of vorticity generated by the upstream force are displaced to the periphery. The final result of the interaction between the vorticity generated by both forces is a regular array of vortices of alternating sign aligned along the axis of the flow. Returning to Fig. 5.1, we can observe that the flows for even higher values of J (Fig. 5.1 c and d) also form a regular vortex street but the character of the vortex shedding becomes different. Close view of images in Fig. 5.4 reveal that the flow in the vicinity of the upstream force now becomes unstable. The upstream force is strong enough to overcome the incoming stream and create a vortex dipole. Vortices in the dipole grow alternatively and separate. While the dipole looses vorticity of one sign it becomes asymmetric and eventually turns in the direction of rotation of the remaining vortex. Thus the periodic shedding of vortices is accompanied by the wobbling of the dipole. Finally, for very large values of J, the flow becomes irregular (Fig. 5.1 e). The wake consists of highly nonlinear vortex dipoles which move in different directions and interact with each other.

The transitions between the regimes described above can be further observed on the plot (Fig. 5.5) of shedding frequency f as a function of J in the series of simulations where the velocity of the stream U was fixed (1-4 in Table 5.1). The transition between the stable wake (zero frequency) to regular vortex shedding can be easily identified on the plot. In the latter regime the shedding of vortices occurs at the downstream force. The frequency slowly decreases with J. The further transition to a regime when the shedding begins at the upstream force, can then be identified by a rapid drop in frequency. The second transition is indicated by arrows in Fig. 5.5. After the drop the frequency follows a pattern of slow decay similar to that observed after the first transition. In this regime the vortex wake experiences a partial

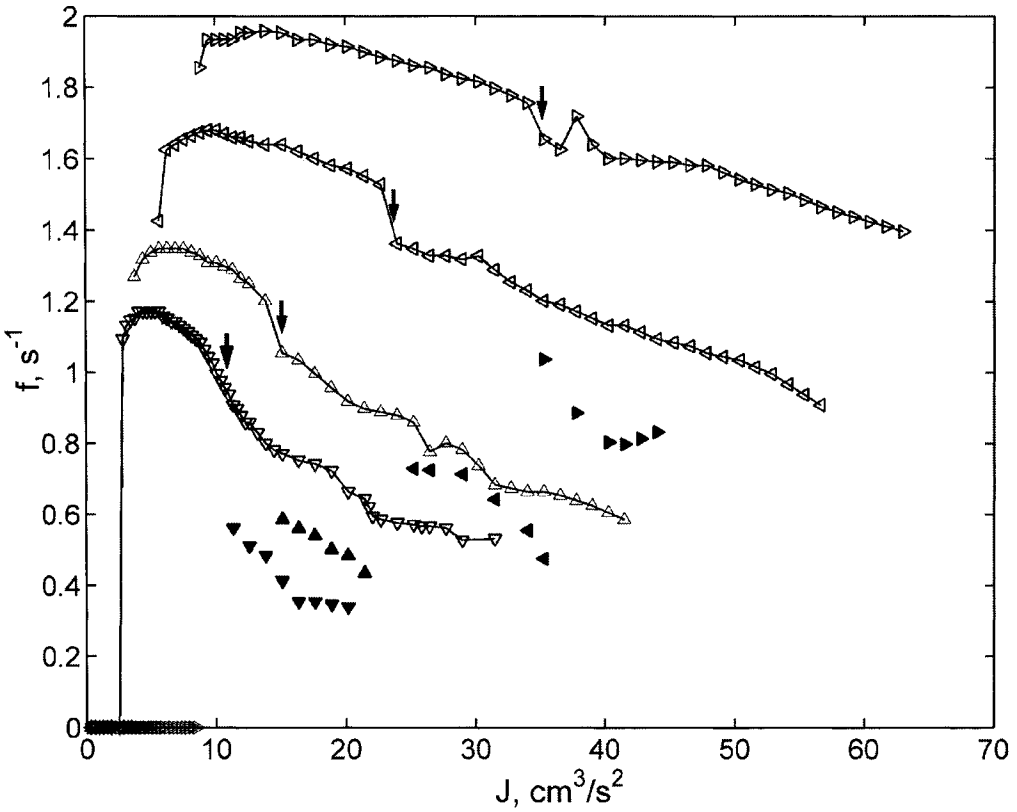

Figure 5.5: Frequency f for different values of J for series 1-4. The legend for symbols is in Table 5.1. Filled symbols show the frequency in the far wake. Arrows indicate the transition between different regimes of vortex shedding.

restabilization which can be observed in the vorticity field between $x = 40$ and $60cm$ in Fig. 5.1 d. Further downstream of this region, the secondary instability develops. Filled symbols in Fig. 5.5 give values of frequency for a secondary instability in the far wake. The values of frequency are approximately two times lower than those for the primary instability. This indicates that this instability is most likely due to a pairing of primary vortices. Figure 5.6 demonstrates the signature of the secondary instability in the distribution of the y-component of velocity along the axis (y = 0) of the flow. The regions of the primary wake closer to the origin and the secondary wake farther from the origin can be clearly seen in the plot.

In series 5-9 (Table 5.1) the value of the momentum flux J was fixed while the velocity U was varied. The plot of shedding frequency as a function of velocity is given in Fig. 5.7. Different regimes of the flow can be identified on the plot in linear coordinates in Fig. 5.7 a. For low values of U the wake is irregular as is depicted in Fig. 5.1 e. There is no definite value of frequency associated with such a wake. For larger U a regularization vortex shedding takes place. During this stage an intermediate asymptotic behavior (Fig. 5.7 b) is observed. For even higher U the wake is stable and the frequency drops to zero. The values of J and U where the first and second transitions are observed, were measured for series 1-9 using plots in Figs. 5.5 and 5.7. While the first transition can be clearly identified on both of these plots, the second transition can only be seen in Fig. 5.5. The values of J are plotted in Fig. 5.8 as a function of U^2. In these coordinates the behavior of the transition values of J is described accurately by linear relations of the form $J = 0.3U^2$ for the first transition and $J = 1.16U^2$ for the second transition. A similar dependence although with different value of the numerical factor, was observed in our previous simulations of the wakes behind a single force (Afanasyev, Korabel [1]). In that case the (second) transition between the different regimes of the flow was related to the appearance

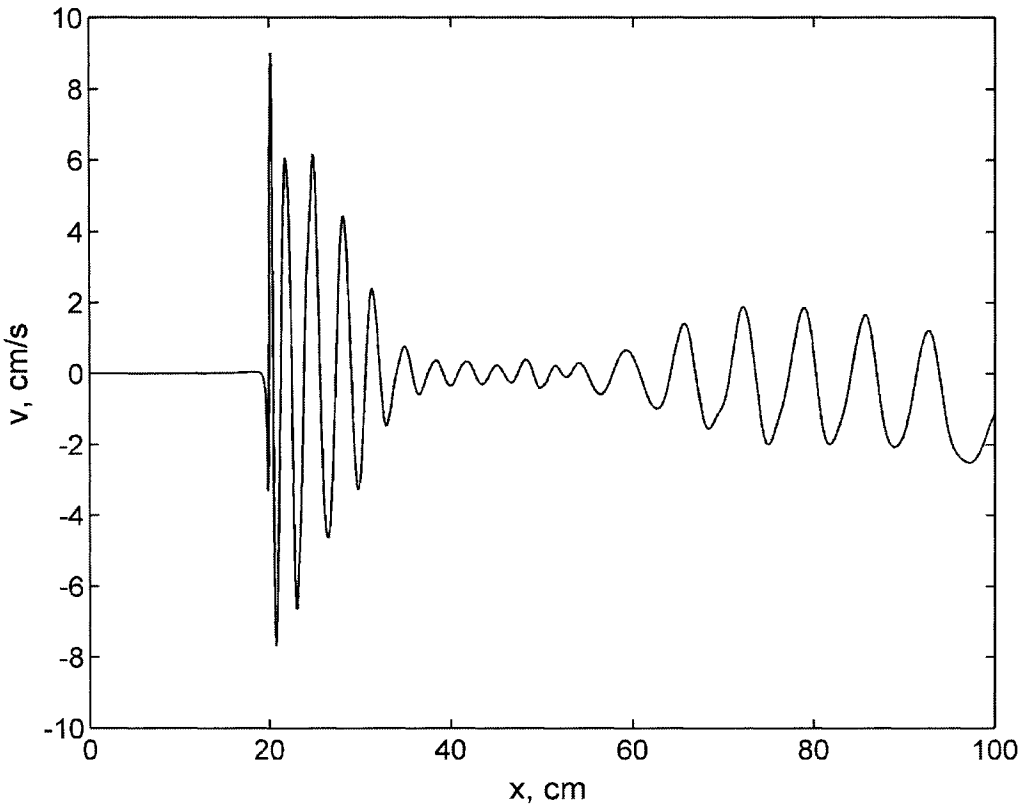

Figure 5.6: Distribution of the y-component of velocity along the axis of the flow ($y = 0$). Control parameters are the same as those for Fig. 5.1 d.

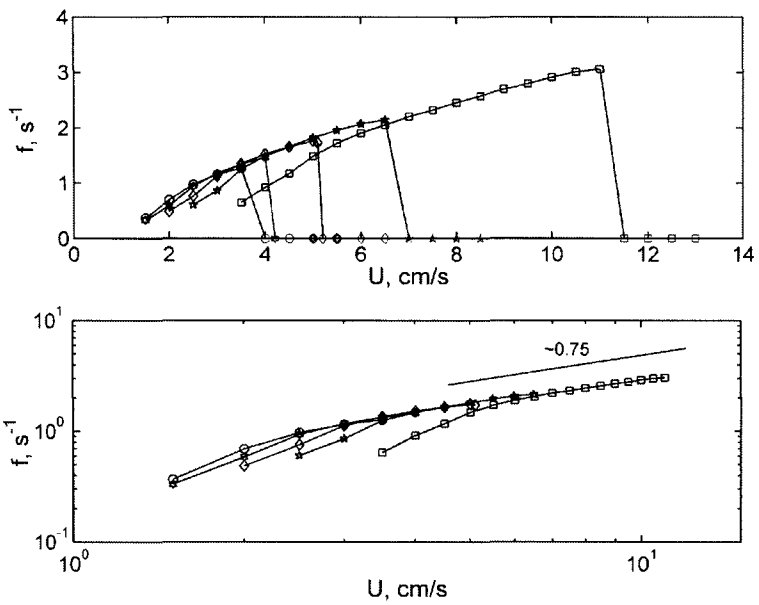

Figure 5.7: Frequency f for different values of U for series 5-9. The legend for symbols is in Table 5.1. Panel b shows the same data in logarithmic coordinates.

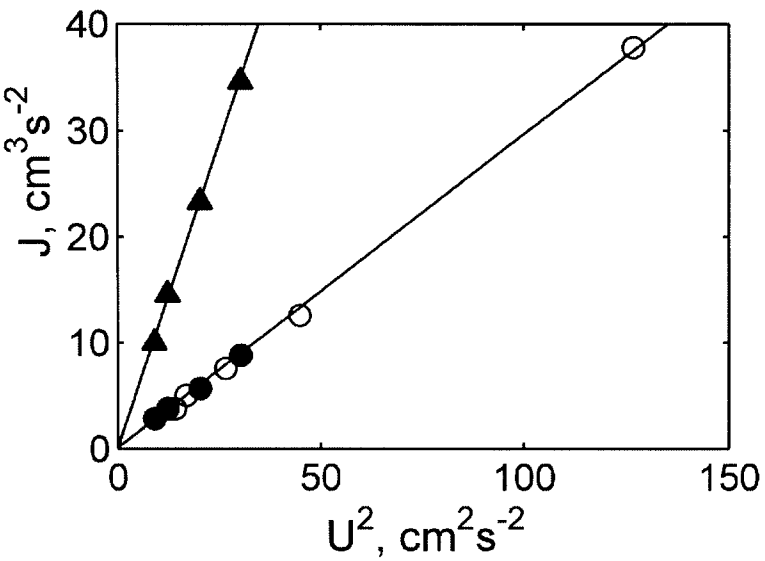

Figure 5.8: Values of J where transitions between the regimes occur for different U^2, measured from plots in Figs. 5.5 and 5.7. Circles show the transition between the stable wakes and wakes with regular vortex shedding. Filled circles are obtained from Fig. 5.7 while clear circles are obtained from 5.5. Triangles show the second transition between different regimes of shedding.

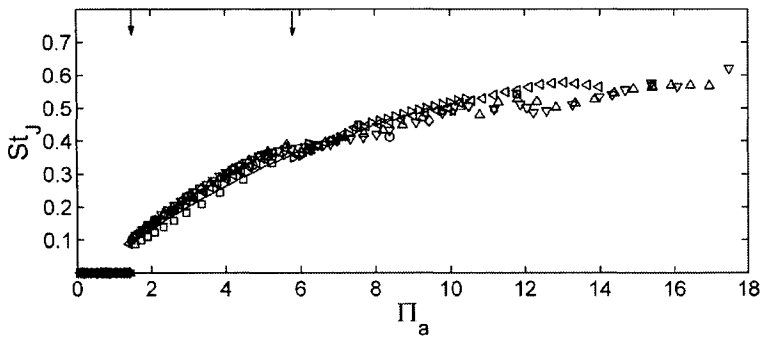

Figure 5.9: The Strouhal number versus Π_α for all series of experiments with two magnets.

of a stagnation point in front of the force at a distance comparable to the size, a, of the area where the force was applied. The flow induced by the force was in the form of a stationary vortex dipole with the stream flowing around it. For values of J smaller than the critical transitional value the stream overwhelms the dipole and the stagnation point does not appear. The position of the stagnation point was obtained from the theoretical relations for the flow induced by a point force. Taking into account the above relations describing the boundaries between the regimes, we can replot the data in the form of dimensionless parameters St_J and Π_α (Fig. 5.9).

The plot in Fig. 5.9 demonstrates that the data for all series of simulations (1-9 in Table 5.1) collapse well in the space of these dimensionless parameters. The data collapse especially well for the regions where transitions take place. The transitions are indicated by arrows at $\Pi_\alpha = 1.5$ and 5.8.

5.2 Concluding remarks

In summary, it can be concluded that the numerical simulations reported in this article provide an insight into the behavior of flows induced by a force doublet. Different regimes of vortex shedding when the shedding occurs either at the upstream or at the downstream force are identified in our simulations. The interaction of vortices generated by both forces is quite complex in the vicinity of the forces and it is somewhat surprising that regular vortex streets are formed downstream for both regimes of vortex shedding. The wake only becomes irregular when the dimensionless parameter Π_α is high enough. In this regime the nonlinear effects become important and the vortices form pairs and translate. Their interactions results in an irregular flow. In the simulations reported in this article only two of the control parameters of the flow, namely the amplitude of forcing J and the velocity of the stream U were varied while the characteristic length scales of the forcing δ and a were fixed. Our preliminary simulations indicate that the regime of the flow might also be sensitive to the value of the ratio δ/a when this ratio is not very large. Understanding the behavior of the flow for different δ and a is both certainly interesting and important and as such will be a subject of our future studies.

5.3 Laboratory experiments

The experimental setup for force doublet is the same as described in Chapter 4. In the experiments with two magnets (force doublet), the magnet in the rear acted in the opposite direction thus simulating the reaction to the thrust force applied by a self-propelled body. Since the drag and thrust forces were of the same magnitude (but of opposite directions) this system simulates a self-propelled body moving with constant speed. Parameters of the experiments with the double forces are summarized in Tables

Series	♯ exps .	J, cm^3/s^2	U, cm/s
1	7	0.8-3.1	0.58
2	11	0.25-3.1	0.87
3	8	0.8-3.1	1.16
4	7	1.3-3.1	1.45
5	5	1.5-3.1	1.74

Table 5.2: Parameters used in laboratory experiments with a double magnet.

5.2. Consider now the results of the experiments where two magnets moving over the surface of the water applied forces of equal magnitude but of opposite direction. Figure 5.10 a demonstrates a typical regimes of the flow.

The magnet at the front generates a dipole stationary in the oncoming stream of velocity U while the magnet at the rear generates a jet flow in the direction opposite to that of the translation of the magnets. A starting vortex dipole can also be seen in the extreme right in figure 5.10 a. For higher values of the magnitude of forcing meandering of the jet similar to that in the experiments with a single magnet, can be observed (not shown here). Plate b of figure 5.10 demonstrates the flow for even higher values of the magnitude of forcing where a regular vortex street is formed in the wake. This vortex street is visually different from the Karman-Benard vortex streets observed in the experiments with a single magnet. While the Karman-Benard vortex street consists of interconnected dipoles, the vortex street for the force doublet can be characterized as an array of interconnected vortex quadrupoles. Each of the quadrupoles consists of two dipoles. Since the prototype flow generated by a stationary localized force is a vortex dipole while the flow generated by a stationary force

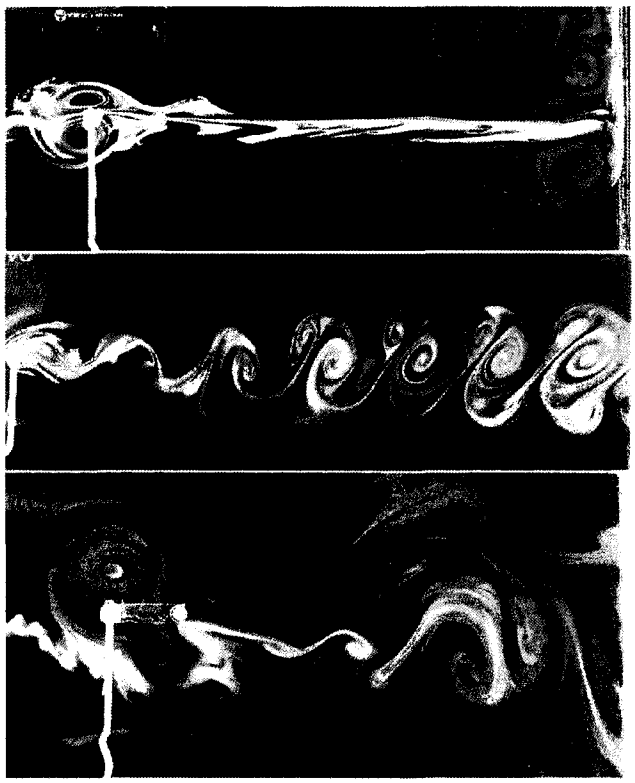

Figure 5.10: Images of the flow generated by two magnets for different regimes. Top view. Experimental parameters: $U = 0.58\,cm/s$, $J = 0.81\,cm^3/s^2$ (a); $U = 0.87\,cm/s$, $J = 3.1\,cm^3/s^2$ (b) and $U = 0.29\,cm/s$, $J = 3.0\,cm^3/s^2$ (c).

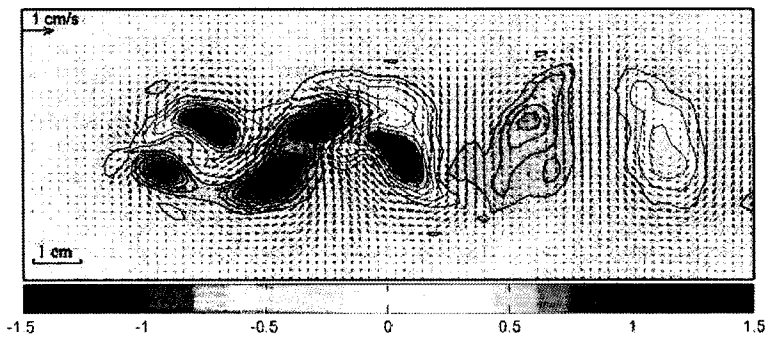

Figure 5.11: Vorticity (color) and velocity (arrows) fields measured in the experiment with two magnets: $U = 0.87\,cm/s$, $J = 0.81\,cm^3/s^2$. The color bar shows the vorticity scale in s^{-1}.

doublet is a vortex quadrupole (e.g. Voropayev and Afanasyev 1994) the arrangement of vortices in the vortex streets correspond to the generic structure of the forcing. A typical vorticity field in the vortex street in the zero momentum wake is shown in figure 5.11.

In the far wake elongated vortices of alternating sign form an array along the x-axis. This is clearly different from the vortex street in the wake generated by a single force where vortices form a checker board pattern (Figire 4.10). Figure 5.10 c illustrates the regime of the flow when the forcing is rather strong while the translation velocity is relatively low. The front magnet generates large scale unsteady dipoles while the rear magnet generates an unstable jet. The overall appearance of the flow is quite irregular in this regime.

The wavelength of the perturbations were measured in the experiments with a force doublet when the wake was unstable in the form of either a meandering jet or the regular vortex street. The dependence of the Strouhal number on the parameter Π_α (figure 5.12) is in general similar to that for the single force (figure 4.22).

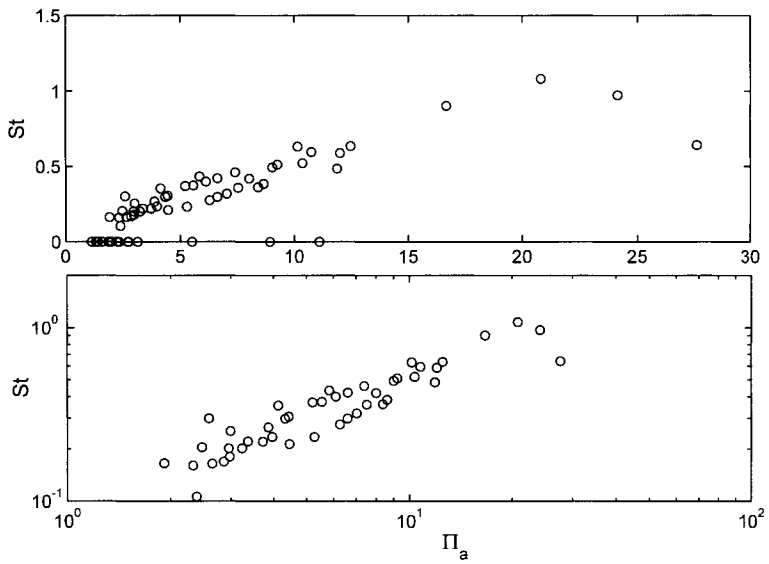

Figure 5.12: The Strouhal number versus Π_α for all series of experiments with two magnets in linear and logarithmic scale.

The values of Π_α where the transition to instability takes place is approximately ($\Pi_\alpha \approx 2$) and is close to that for the single force. Note that in the problem with a force doublet there is one additional dimensional parameter, namely the distance δ between the magnets. However, in our present investigation this distance was fixed, $\delta = 3$ cm. The dependence of the flow characteristics on this parameter is a subject of further investigations.

5.3.1 Conclusions and Discussions

The results of numerical and laboratory experiments demonstrated an existence of a large number regimes of the flow generated by a moving "virtual" self-propelled body in two-dimensional geometry. The regimes of the wake are similar to ones observed in experiments with a single force simulating the towed body. They include the steady jet carrying zero momentum, the unsteady meandering jet where the initial instability is symmetric in the form of a chain of vortex dipoles, the regular vortex street and finally the irregular ejection of vortex dipoles.

The results of experiments with the force doublet which simulates the self-propelled body were qualitatively similar to those with a single force. The pattern of the vortex street behind the force doublet was however different from that of the Karman-Benard vortex street. This pattern consisted of interconnected vortex quadrupoles which is consistent with the generic structure of forcing. The far wake transforms eventually into an array of vortices of alternating sign located along the x-axis.

The behavior of the dimensionless frequency of vortex shedding exhibit dependence on the parameter Π_α and negligible dependence on the parameter Π_ν which includes the kinematic viscosity, for relatively high values of the speed U. In the regime of the vortex street however, when U is smaller and J is larger, the dependence on viscosity becomes significant. This dependence can be expressed in the form

of the linear relation between the Roshko number and the Reynolds number of the flow in direct analogy to the relation for the flow around a circular cylinder.

In summary, it can be concluded that the numerical simulations reported in this chapter provide an insight into the behavior of flows induced by a force doublet. Different regimes of vortex shedding when the shedding occurs either at the upstream or at the downstream force are identified in our simulations. The interaction of vortices generated by both forces is quite complex in the vicinity of the forces and it is somewhat surprising that regular vortex streets are formed downstream for both regimes of vortex shedding. The wake only becomes irregular when the dimensionless parameter Π_α is high enough. In this regime the nonlinear effects become important and the vortices form pairs and translate. Their interactions results in an irregular flow. In the simulations reported in this article only two of the control parameters of the flow, namely the amplitude of forcing J and the velocity of the stream U were varied while the characteristic length scales of the forcing δ and a were fixed. Our preliminary simulations indicate that the regime of the flow might also be sensitive to the value of the ratio δ/a when this ratio is not very large. Understanding the behavior of the flow for different δ and a is both certainly interesting and important and as such will be a subject of our future studies.

Chapter 6

Conclusions

A new class of flows generated by a localized forcing, both stationary and moving, has been studied. A combination of theoretical work, numerical simulations and laboratory experiments was used in the investigation. Theoretical analysis is based on the application of the Oseen approximation. This approach allows one to offer a unified description for the number of flows generated by localized forces in different spatial configurations. One possible application of this approach includes the investigation of far-field wakes of towed and self-propelled bodies. A commercial finite volume CFD code FLUENT was used in numerical simulations. A rectangular high-resolution computational domain was employed for unsteady simulations of dipole and wake flows. A new experimental technique based on the utilization of the electromagnetic method of forcing was developed for the investigation of wake flow in laboratory experiments. This method of forcing allows to create a "virtual" body without introducing any

solid objects into the fluid.

The first set of results deals with the case of stationary localized force acting on a static fluid. In this situation a starting dipole flow is generated. Two cases with the force which acts impulsively or continuously on a fluid were investigated. Theoretical expressions for the vorticity and stream-function of the dipole flow are obtained in the Oseen approximation for both cases. The comparison with the results of fully non-linear numerical simulations and laboratory experiments shows that the Oseen approximation gives a reasonable theoretical prediction for the propagation velocity of the dipole. The theoretical result which predicts the power law asymptotic behavior of the flow turned out to be especially robust even when additional factors such as the bottom friction in the laboratory experiments affect the flow.

The second set of results describes the numerical simulations and laboratory experiments of the wake flow generated by a single moving localized force or a "virtual" towed body in two-dimensional geometry. If a single localized force is moving with respect to fluid, it generates a wake, a region with a substantial velocity deficit. The deficit in u-velocity decays rapidly and spreads out downstream. The correspondent instantaneous vorticity field for the stable wake is of the form of a "fork". The stable wake experiences instability and becomes unstable with vorticity arranged in the form of regular vortex street. It has been shown that the development and further evolution of the vortex structures calculated with a fully non-linear Navier-Stokes solver are in good agreement with the results of laboratory experiments.

The numerical simulations and laboratory experiments demonstrate the existence of a large number of flow regimes which include the steady wake, the unsteady meandering wake with the initial instability, the regular Karman-Benard vortex street and finally the irregular wake with the large number of erratically ejected vortex dipoles.

For the stable wake, velocity and vorticity profiles calculated in numerical simula-

tions and obtained with the help of Particle Image Velocimetry technique in laboratory experiments were compared with the theoretical profiles derived using the Oseen approximation. The agreement appears to be good in the region far from the origin of the forcing.

The results of the unsteady numerical simulations of the unstable wake flow provide a detailed quantitative description of the behavior of the dimensionless shedding frequency, the Strouhal number, for different values of two dimensionless arguments which include the main control parameters of the flow, namely the magnitude of the forcing, the size of the forcing area, the velocity of the stream and the kinematic viscosity of the fluid. The transition between stable and unstable wake was investigated in the space of control parameters. It was shown that the transition point is well described by the theoretical relation. Characteristics of unstable wakes, in particular the shedding frequency was measured for variable magnitude and translational speed of the forcing.

Flow visualizations with the help of pH-indicator made in laboratory experiments allow to perform quantitative laboratory measurements of the wake instability wavelength and compare the shedding frequency in the laboratory experiments to that measured in the numerical simulations. It was shown that both approaches describe well main regimes of the flow and give close values of the dimensionless parameters corresponding to the transition points between regimes.

Several distinct regimes of vortex shedding were observed in numerical simulations and the asymptotic relations for the Strouhal number were obtained. The analysis shows that the transition between regimes is due to the finite size of the forcing region. The boundary between the regimes is described by the theoretical relation for the position of the stagnation point when this position is fixed with respect to the size of the forcing area.

The third set of results covers the numerical simulations and laboratory experiments of the flow generated by a moving force doublet, or a "virtual" self-propelled bluff body. The wake flow shows a variety of regimes which include the steady jet carrying momentum, the unsteady meandering jet where the initial instability is symmetric in the form of a chain of vortex dipoles, the vortex street, similar to Karman-Benard vortex street, and finally the irregular ejection of vortex dipoles. The pattern of the vortex street behind the force doublet was however different from that of the Karman-Benard vortex street. This pattern consisted of interconnected vortex quadrupoles which is consistent with the generic structure of forcing. The far wake transforms eventually into an array of vortices of alternating sign located along the x-axis.

The qualitative investigation of the instantaneous vorticity fields and shedding frequency in the form of the dimensionless Strouhal and Roshko numbers shows similarities of the investigated flows with the flows generated by a single localized force. The transition due to the finite size of the forcing area also exists in this case.

The results of the numerical simulations give a detailed description of the mechanics of the vortex shedding in the case of the force doublet. Different shedding regimes when the the shedding occurs either on the upstream or downstream force are identified and investigated.

The interaction of vortices generated by both forces is quite complex. When the nonlinear effects become important, the vortices form pairs and translate. In this regime the wake flow is irregular.

In the investigation of the flow generated by a force doublet two parameters, namely the distance between two forces δ and the size of the forcing area a were kept constant. Numerical simulations suggest that the regime of the flow might be also sensitive to the value of the ratio δ/a. Understanding the behavior of the flow for

different δ and a is both interesting and important and could be a subject of a future research.

In summary, the new class of flows generated by localized forces has been investigated. It includes flows generated by a stationary localized forcing (single force, force doublet, etc.) acting on a static fluid and flows generated by a moving forcing. The latter class of flows includes flows behind towed and self-propelled bluff bodies. The approach in which the effect of the body on a fluid is effectively reduced to a combination of spatially localized forces acting on the fluid is justified when one is interested in a flow far from the body (far-field flow). This approach may be generalized to an arbitrary spatial distribution of forces. Due to important oceanographic and engineering applications this approach requires serious further investigation.

Appendix A

Appendix A

A.1 Commercial CFD package FLUENT 6.2

All numerical simulations of the described flows are carried out by solving the Navier-Stokes equations in two dimensions. The code used is Fluent (Fluent 1999). Fluent is an unstructured-mesh solver based on second-order-accurate spatial and time discretization. Technical literature and manuals can be found on the web-site www.fluent.com.

A.2 UDFs specifying external body force

The following C script was written to produce an external force in the right-hand side of the Navier-Stokes equations (2.1). The script runs continuously or for the certain period of time depending of the temporal characteristics of the focing.

```
/************************************************************************/
/* UDF for specifying an x-momentum source term in a spatially
*/ /* dependent porous media
*/
/************************************************************************/

#include "udf.h"

#define CON 300.0

#define AMP 400.0

#define XCENTRELEFT 0.2

#define YCENTRELEFT 0.0

#define XCENTRERIGHT 0.23

#define YCENTRERIGHT 0.0

DEFINE_SOURCE(xmom_source, c, t, dS, eqn) {
  real xc[ND_ND];
  real con, source;
  real r2left, r2right;
  real a = 0.002;

  C_CENTROID(xc, c, t);

    r2left = pow(xc[0] - XCENTRELEFT,2) + pow(xc[1] - YCENTRELEFT,2);
    r2right = pow(xc[0] - XCENTRERIGHT,2) + pow(xc[1] - YCENTRERIGHT,2) ;

    if ( r2left <= 0.002 && r2right <= 0.002 )
    {
      /* source term */

      source = AMP*(-exp(-r2left/(a*a)) + exp(-r2right/(a*a)));

    }

  else
    source = 0.0;
  return source;
}
```

BIBLIOGRAPHY

Abernathy, F. H. and Kronauer, R. E (1962). The Formation of Vortex Streets. *J. Fluid Mech.*, **13**, 1-20.

Afanasyev Y.D. (2004). Wakes behind towed and self-propelled bodies: asymptotic theory, *Phys Fluids*, **16**, 3235-3238.

Afanasyev Y.D. and I.A. Filippov (1995). Formation of a vortex street behind an oscillating cylinder, *Fluid Dynamics*, **30**, 40.

Afanasyev Y.D., S.I. Voropayev and I.A. Filippov (1989). A model of the mushroom-like currents in a stratified fluid when a source of momentum acts continuously. Izvestiya Russ. Acad. of Sci., *Atmosp. and Ocean. Phys.*, **25** (7), 741-750.

Afanasyev Y.D., S.I. Voropayev and P.G. Potylitsin (1993). A model of vortex dipole interactions in the upper ocean. *Izvestiya Russ. Acad. of Sci.*, Atmosp. and Ocean. Phys., **30** (5), 696-703.

Afanasyev Y.D.and S.I. Voropayev (1989). On the spiral structure of the mushroom-like currents in the ocean. *Dokl. Akad. Nauk SSSR*, **308** (1), 179-183.

Afanasyev,Y.D. and Wells, J. (2005). Quasi-two-dimensional turbulence on the polar beta-plane: laboratory experiments, *Geophys. Astrophys. Fluid Dynamics*, **99** (1), 1-17.

Batchelor G.K. (1967), *An Introduction to Fluid Dynamics* (Cambridge University Press. Cambridge).

Bearman, P. W. (1984). Vortex Shedding from Oscillating Bluff Bodies. *Ann. Rev. Fluid Mech.*,**16**, 195 - 222

Berger, E., and Wille, R. (1972). Periodic flow phenomena. *Ann. Rev.Fluid Mech.*, **4**, 313-340.

Cantwell B.J. (1986). Viscous starting jets. *J. Fluid Mech.* **173**, 159.

Chaplin J. R. (1999). History forces and the unsteady wake of a cylinder, *J. Fluid Mech.*, **393**, 99-121.

Chasnov, J. R. (1997). On the decay of two-dimensional homogeneous turbulence. *Phys. Fluids*, **9**, 171.

Danilov, S., Dolzhanskii, F. V., Dovzhenko, V. A. and Krymov, V. A. (2002). Experiments on free decay of quasi-two-dimensional turbulent flows. *Phys. Rev. E.*, **65**, 036316-1

Dusek J., P. Le Gal, P. Fraunié (1994). A numerical and theoretical study of the first Hopf bifurcation in a cylinder wake, *J. Fluid Mech.* **264**, 59-80.

Easterling K. (1983), *Introduction to the Physical Metallurgy of Welding* (Butterworths & Co. Ltd., London).

Farlow S. J., (1993). *Partial Differential Equations for Scientists and Engineers*, Dover.

Fedorov, K. N. and Ginsburg, A. I.(1989). Mushroom-like currents (vortex dipoles): One of the most wide-spread forms of non-stationary coherent motions in the ocean, In *Mesoscale/Synoptic Coherent Structures in Geophysical Turbulence*, edited by J. C. Nihoul and B. M. Jamart, Elsevier, Amsterdam, 15.

Gerrard, J. H. (1966). The Mechanics of the Formation Region of Vortices Behind Bluff bodies. *J. Fluid Mech.*, **25**, 401-13

Ginsburg, A. I. and Fedorov, K. N. (1984). Mushroom-formed currents in ocean (on the base of analysis of satellite images), *Investigation of the Earth from the Space*, **3**, 18.

Gollub, J.P., Clarke, J., Gharib, M., Lane, B. and O.N. Mesquita (1991). Fluctuations and transport in a stirred fluid with a mean gradient, *Phys. Rev. Lett.*, **67**, 3507-3511.

Hinch E.J. (1999). In *Mixing: Chaos and Turbulence*, edited by H. Chate, E. Villermaux, and J.-M. Chomaz (Klewer Academic/Plenum Publishers, New York), p. 37.

Inoue O., T. Yamazaki (1999). Secondary vortex streets in two-dimensional cylinder wakes, *Fluid Dyn. Res.*, **25**, 1-18.

Karasudani T., M. Funakoshi (1994). Evolution of a vortex street in far wake of a cylinder, *Fluid Dyn. Res.*, **14**, 331-352.

Kármán, Th. von. (1954). *Aerodynamics*. Cornell University Press.

Kovasznay, L.S.G. (1949). Hot-wire investigation of the wake behind cylinder at low Reynolds numbers. *Proc. Roy. Soc. London*, **A198**, 174-190.

Mair, W.A., and Maull, D.J. (1971). Bluff bodies and vortex shedding: a report on EuroMech 17. *J. Fluid Mech.*, **45**, 209-24.

Martin, B. K., Wu, X. L., Goldburg, W. I. and Rutgers, M. A.(1998). Spectra of Decaying Turbulence in a soap film, *Phys. Rev. Lett.* **80**, 3964

Morkovin, M.V. (1964). Flow around circular cylinder – a kaleidoscope of challenging fluid phenomena, *Proc. ASME Symp. Fully Separated Flows* (ed. A. G. Hansen), 102-118, New York.

Neill and Elliot (2004). Observations and simulations of an unsteady island wake in the Firth of Forth, Scotland. *Ocean Dynamics*, **54**, Issue 3-4, 324-332.

Oertel, H. Jr. (1990). Wakes behind blunt bodies. *Ann. Rev. Fluid Mech.*, **22**, 539-64.

Pope S.B. (1994). Lagrangian PDF methods for turbulent flows. *Annu. Rev. Fluid. Mech.* **26**, 23-63.

Roshko A. (1954). On the development of turbulent wakes from vortex streets, NACA Report 1191, National Advisory Committee for Aeronautics, Washington, DC, U.S.A.

Ruijter de W.P.M., H. M. van Aken, E. J. Beier, J. Lutjeharms, R. Matano, M. Schouten (2004). Eddies and dipoles around South Madagascar: formation, pathways and large-scale impact. *Deep Sea Res. I*, **51**, 383–400.

Sane, S. P. (2003). The aerodynamics of insect flight, *J.Exper. Biol.,* **206**, 4191-4208.

SarpkayaT. (1979). Vortex Induced Oscillations: a Selective Review. *ASME Journal of Applied Mechanics*, **46**, 241-258.

Smirnov S.A. and S.I. Voropayev (2003). On the asymptotic theory of momentum/zero-momentum wakes, *Phys. Letters A*, **307**, 2.

Sozou C. (1979). Development of the flow field of a point force in an infinite fluid, *J. Fluid Mech.* **91**, 541.

Stokes, G.G . (1851). On the Effect of the Internal Friction of Fluids on the Motion of Pendulums. *Trans.Camb.Phil.Soc.* **9**, 8 -106 (Mathematical and Phisical Papers 3, I)

Strouhal, V. (1878). Uber eine besondere Art der Tonerregung. *Ann. Physik. Chem.* (Leipzig) **5** (10), 216-251.

Taneda S. (1959). Downstream development of the wakes behind cylinders, *J. Phys. Soc. Jpn.* **14**, 843.

Thompson M.C., P. Le Gal (2004). The Stuart-Landau model applied to wake transition revisited, *European Journal of Mech. Fluids,* **23**, 219-228 .

Tritton, D.J. (1959). Experiments on flow past circular cylinder at low Reynolds number. *J. Fluid Mech.*, **6**, 547-567.

Tritton, D.J. (1971). A note on vortex street behind circular cylinder at low Reynolds numbers. *J. Fluid M*ech., **45**, 203-208.

Villermaux E., H. Chate, and J.-M. Chomaz (1999). in *Mixing: Chaos and Turbulence*, edited by H. Chate, E. Villermaux, and J.-M. Chomaz (Klewer Academic/Plenum Publishers, New York), p. 1.

Vorobieff P., D. Georgiev and M. S. Ingber (2002). Onset of the second wake: Dependence on the Reynolds number, *Phys. Fluids*, **14**, 7 .

Voropayev S.I. (1985). Theory of the self-similar development of a jet in a uniform-density fluid, *Izvestiya, Acad. Sciences USSR*, Atmos. Oceanic Physics, **21**, 975.

Voropayev S.I. and Y.D. Afanasyev (1992). Two-dimensional vortex dipoles interactions in a stratified fluid. *J.Fluid Mech.*, **236**, 665-689.

Voropayev S.I., Y.D. Afanasyev and I.A. Filippov (1991). Horizontal jets and vortex dipoles in a stratified fluid. *J. Fluid Mech.* **227**, 543.

Voropayev S.I., Y.D. Afanasyev, V. N. Korabel and I.A. Filippov(2003). On the frontal collision of two round jets in water, *Phys. Fluids*, **15**, 3429.

Voropayev S.I.and Y.D. Afanasyev (1994), *Vortex Structures in a Stratified Fluid* (Chapman and Hall. London).

Voropayev, S.I. and Afanasyev Ya.D. (1992). Two dimensional vortex dipole interaction in a stratified fluid. *J. Fluid Mech.*, **236**, 665-89.

Williamson C. H. K. and R. Govardhan (2004). Vortex-induced vibrations, *Ann. Rev. Fluid Mech*, **36**, 413-455.

Williamson C. H. K. (1996). Three-dimensional wake transition, *J. Fluid Mech.*, **328**, 345-407.

Williamson C. H. K. and A. Prasad (1993). Wave interactions in the far wake of a body, *Phys. Fluids,* **A 5**, 1854.

Zdravkovich M. M. (1997). *Flow Around Circular Cylinders*, Oxford University Press.